stronomy & strophysics manuscript no. Seyfert
September 30, 2018

The X-ray variability of Seyfert 1.8/1.9 galaxies

Hernández-García, L.[1,2]; Masegosa, J.[1]; González-Martín, O.[3]; Márquez, I.[1]; Guainazzi, M.[4]; Panessa, F.[2]

[1] Instituto de strofísica de ndalucía, CSIC, Glorieta de la stronomía, s/n, 18008 Granada, Spain
[2] IN F - Istituto di strofisica e Planetologia Spaziali di Roma (I PS-IN F), Via del Fosso del Cavaliere 100, I-00133 Roma, Italy
e-mail: lore a.her a dez@iaps.i af.it
[3] Instituto de radioastronomía y strofísica (IRy -UN M), 3-72 (Xangari), 8701, Morelia, Mexico
[4] European Space Research and Technology Centre (ES /ESTEC), Kepleriaan 1, 2201 Z Noordwijk, The Netherlands

Received XXX / ccepted XXX

BSTR CT

Context. Seyfert 1.8/1.9 are sources showing weak broad H_α components in their optical spectra. ccording to unification schemes, they are seen with an edge on inclination, similarly to type 2 Seyfert galaxies, but with slightly lower inclination angles.
ims. We aim at testing whether Seyfert 1.8/1.9 have similar properties at UV and X-ray wavelengths.
Methods. We use the 15 Seyfert 1.8/1.9 in the Véron Cetty and Véron catalogue with public data available from the *Chandra* and/or *XMM–Newton* archives at different dates, with timescales between observations ranging from days to years. ll the spectra of the same source were simultaneously fitted with the same model and different parameters were left free to vary in order to select the variable parameter(s). Whenever possible, short-term variations from the analysis of the X-ray light curves and long-term UV variations from the optical monitor onboard *XMM–Newton* were studied. Our results are homogeneously compared with a previous work using the same methodology applied to a sample of Seyfert 2 (Hernández-García et al. 2015a).
Results. X-ray variability is found in all 15 nuclei over the aforementioned ranges of timescales. The main variability pattern is related to intrinsic changes in the sources, which are observed in ten nuclei. Changes in the column density are also frequent, as they are observed in six nuclei, and variations at soft energies, possibly related to scattered nuclear emission, are detected in six sources. X-ray intra-day variations are detected in six out of the eight studied sources. Variations at UV frequencies are detected in seven out of nine sources.
Conclusions. comparison between the samples of Seyfert 1.8/1.9 and 2 shows that, even if the main variability pattern is due to intrinsic changes of the sources in the two families, these nuclei exhibit different variability properties in the UV and X-ray domains. In particular, variations in the broad X-ray band on short time-scales (days/weeks), and variations in the soft X-rays and UV on long time-scales (months/years) are detected in Seyfert 1.8/1.9 but not in Seyfert 2. Overall, we suggest that optically classified Seyfert 1.8/1.9 should be kept separated from Seyfert 2 galaxies in UV/X-ray studies of the obscured GN population because their intrinsic properties might be different.

Key words. Galaxies: active – X-rays: galaxies – Ultraviolet: galaxies

1. Introduction

ctive galactic nuclei (GN) are though to be powered by accretion of matter onto the supermassive black hole (SMBH) that resides in the center of the galaxies (Rees 1984). Historically, these nuclei have been classified as type 1 when broad Balmer permitted lines (full-width at half maximum (FWHM)∼1000-20000 km/s) are detected in their optical spectra, while they are classified as type 2 when detecting only narrow lines (FWHM∼300-1000 km/s). Using the relative intensity of broad and narrow lines, the nuclei can also be classified as type 1.2, 1.5, 1.8, or 1.9 GN (intermediate Seyferts), the latter having the weaker broad component (e.g., Osterbrock 1977; Osterbrock & Martel 1993). In particular, the optical spectra of Seyfert 1.8 are characterized by strong narrow emission lines combined with weak broad H_α and H_β emission lines, whereas Seyfert 1.9 present the narrow lines but only a weak broad H_α emission line (Osterbrock 1981).

The detection of broad components in polarized light of type 2 sources set the unified model of GN (Lawrence et al. 1987; ntonucci 1993; Urry & Padovani 1995; Moran et al. 2000). Under this scenario, the different properties observed in GN can be explained by orientation effects, i.e., they are the same kind of source observed at different angles. The cornerstone of this model is a dusty structure (often simplified as a torus) that surrounds the SMBH, which plays a fundamental role as it is responsible for obscuring the broad line region (BLR) where the broad lines are created. In support of this model, X-ray observations have shown that type 2 sources are more obscured than type 1s, whereas type 1.8 and 1.9 GN are less absorbed than strictly type 2s (Risaliti et al. 1999).

X-rays are indeed a powerful tool for the comprehension of GN as they are capable to reach closer to the SMBH than other wavelengths. t these energies the absorbing column density, N_H, is used to classify sources as unobscured (type 1) when N_H is below $\sim 10^{22} cm^{-2}$ and obscured (type 2) sources for larger values. For N_H values larger than 1.5 $10^{24} cm^{-2}$, the sources are classified as Compton-thick (Maiolino et al. 1998). Sometimes transitions from Compton-thick to Compton-thin (or vice versa) have been observed; these are known as changing-look sources according to the original nomenclature by Matt et al. (2003).

Variability is one of the properties characterizing GN, a highly valuable tool for the comprehension of their physical structure (Peterson 1997; Netzer 2013). The first systematic studies of GN showed that short-term X-ray variabil-

Table 1: General properties of the sample galaxies.

Name	R (J2000)	DEC (J2000)	Dist.[1] (Mpc)	N_{Gal} (10^{20} cm^{-2})	m_V	Morph. type	Seyfert type	$\log M_{BH}$ $M_\odot$
(1)	(2)	(3)	(4)	(5)	(6)	(7)	(8)	(9)
ESO 540-G01	00 34 13.8	-21 26 20	110.5	1.62	13.7	SBc	1.8	-
ESO 195-IG21	01 00 36.5	-47 52 03	201.8	1.65	16.7	-	1.8	-
ESO 113-G10	01 05 17.0	-58 26 13	104.1	2.95	14.6	SBa	1.8	6.85
NGC 526	01 23 54.4	-35 03 56	77.8	2.19	14.6	S0	1.9	7.90
M RK 609	03 25 25.4	-06 08 39	141.1	4.42	14.1	S0	1.8	-
NGC 1365	03 33 36.4	-36 08 24	18.0	1.35	13.0	Sb	1.8	7.54
NGC 2617	08 35 38.8	-04 05 19	56.1	3.65	14.0	SBc	1.8	7.60
M RK 1218	08 38 11.1	24 53 45	116.6	3.54	14.1	Sb	1.8	-
NGC 2992	09 45 42.0	-14 19 35	30.5	4.99	13.8	Sa	1.9	7.73
POX 52	12 02 56.8	-20 56 03	87.3	4.03	17.2	-	1.8	5.14
NGC 4138	12 09 29.9	43 41 06	16.0	1.36	12.2	S0-a	1.9	7.30
NGC 4395	12 25 48.9	33 32 48	4.5	1.35	10.3	Sm	1.8	4.82
NGC 4565	12 36 20.6	25 59 11	12.1	1.30	12.4	Sb	1.9	6.30
M RK 883	16 29 52.8	24 26 39	155.7	3.97	14.4	I	1.9	7.28
IR S 20051-1117	20 07 51.4	-11 08 35	128.9	6.57	14.0	-	1.9	7.11

(Col. 1) Name, (Col. 2) right ascension, (Col. 3) declination, (Col. 4) distance, (Col. 5) galactic absorption, (Col. 6) aparent magnitude in the Johnson filter V from Véron-Cetty & Véron (2010), (Col. 7) galaxy morphological type from Hyperleda, (Col. 8) GN type as in Véron-Cetty & Véron (2010), and (Col. 9) black-hole mass on logarithmical scale, determined using the correlation between stellar velocity dispersion (from HyperLeda) and black-hole mass (Tremaine et al. 2002), or obtained from the literature otherwise (ESO 113-G10 from Cackett et al. (2013), NGC 526 from Vasudevan & Fabian (2009), NGC 2617 from Shappee et al. (2014), M RK 883 from Benítez et al. (2013), and IR S 20051-1117 from Wang & Zhang (2007).)

[1] ll distances are taken from the NED and correspond to the average redshift-independent distance estimates.

ity (from hours to days) is common in type 1s, but not in type 2s, while long-term (from months to years) variations are common in both (e.g., Nandra et al. 1997; Turner et al. 1997; Vaughan et al. 2005). Nowadays we believe that the X-ray variations might be related to intrinsic changes of the nuclear source (e.g., Uttley et al. 2005; Uttley 2007; Parker et al. 2015), or to absorbing clouds that intersect the line of sight to the observer (e.g., Risaliti et al. 2007). These changes can be studied by modelling the X-ray spectrum of GN, whose continuum is dominated by a power-law component extending up to a cut-off at energies ≥100 keV (e.g., Zdziarski et al. 1995; Guainazzi et al. 2005; Fabian et al. 2015). Changes in the power law might indicate a change in the accretion disk or the X-ray corona, while changes in the absorption may be related to clouds in our line of sight, more likely in the BLR, the torus, or the boundary between them (Risaliti et al. 2002, 2005a, 2011; Braito et al. 2013; Markowitz et al. 2014).

Due to their similar optical and X-ray spectra, it is usually assumed that optically classified Seyfert 1.2 and 1.5 behave more likely type 1s, whereas types 1.8 and 1.9 behave as type 2s. Indeed, many studies aiming at analyzing the properties of type 2 sources have included Seyfert 1.8/1.9 in their samples (e.g., Guainazzi et al. 2001; Risaliti 2002; kylas & Georgantopoulos 2009).

However, it is not clear whether the properties of Seyfert 1.8/1.9 are directly related to differences in the nuclear continuum or to an obscurer in our line of sight, since weaker broad lines may be produced by a lower ionizing continuum flux or by reddening from the BLR or the host galaxy (Osterbrock 1981; Goodrich 1995; Trippe et al. 2011). Through the analysis of variability, we are able to differentiate between changes in the accretion state and the configuration of the clouds. The main purpose of the present work is to homogeneously compare the variability properties of optically classified Seyfert 1.8/1.9 and Seyfert 2. The ultimate goal of our study is to understand the physical origin of the phenomenological differences between Seyfert 1.8/1.9 and Seyfert 2 in the optical, UV and X-ray. We employ X-ray variability as gauge in this paper. This study is part of a systematic analysis of the variability properties of nearby GN; by now we have analyzed the properties of a sample of optically classified low ionization nuclear emission line regions (LINERs, Hernández-García et al. 2013, 2014), and a sample of Seyfert 2 (Hernández-García et al. 2015a). comparison between the properties of LINERs and Seyfert 2 was carried out in Hernández-García et al. (2016).

The paper is organized as follows. The sample selection is presented in Sect. 2. The data reduction and the methodology are explained in Sect. 3 and 4. The results of the analysis are presented in Sect. 5, which are discussed in Sect. 6. Finally, the conclusions of this study are summarized in Sect. 7.

2. Sample and data

We used the 13^{th} edition of the Véron-Cetty and Véron catalogue (Véron-Cetty & Véron 2010), which contains quasars and GN. We selected nearby sources located at redshifts below 0.05[2] that were classified as Seyfert type 1.8 and 1.9. In this way we selected 142 Seyfert 1.8 and 189 Seyfert 1.9.

We used the HE S RC database[3] to search for public data in the *Chandra* and/or *XMM–Newton* archives of these sources. In order to study X-ray variability, we selected those sources with more than one observation with these satellites. This included 12 Seyfert 1.8 and another 12 Seyfert 1.9.

[2] The redshift of 0.05 corresponds to a distance of d=214.3 Mpc (using $H_0 = 70\ km\ s^{-1}$). The limit on distance was chosen to be the same as in Hernández-García et al. (2015a) for Seyfert 2.

[3] http://heasarc.gsfc.nasa.gov/

We restricted further our sample to sources whose spectra have a minimum of 400 number counts in the 0.5–10 keV energy band (to use χ^2-statistics) and to not be affected by a pileup fraction larger than 10%. This leaves us with nine Seyfert 1.8 and seven Seyfert 1.9. We removed M RK 1018 from the sample because, although being classified as a Seyfert 1.9 by Osterbrock (1981) using optical data, Cohen et al. (1986) reported variations from Seyfert 1.9 to Seyfert 1 also using optical data, and remained as a Seyfert 1 at least up to 2007 (Trippe et al. 2010).

Therefore, the final sample includes nine Seyfert 1.8 and six Seyfert 1.9. The sample properties are presented in Table 1.

It is worth to notice that a caveat in the analysis could be related to the non simultaneity of the X-ray data with the optical spectroscopic data used for the optical classification of the sources. Unfortunately, the only case in our sample where the X-ray and optical data were obtained at close epochs is NGC 2617, where the X-ray data were taken in 2013, while it was reclassified as a Seyfert 1 using optical spectroscopy gathered in 2014, confirming that variability might be an important issue.

3. Data reduction

3.1. Chandra data

Chandra observations were obtained from the CIS instrument (Garmire et al. 2003). Data reduction and analysis were carried out in a systematic, uniform way using CXC Chandra Interactive nalysis of Observations (CI O[4]), version 4.6. Level 2 event data were extracted by using the task ACIS-PROCESS-EVE TS. Background flares were cleaned using the task LC_CLEA .SL[5], which calculates a mean rate from which it deduces a minimum and maximum valid count rate and creates a good time intervals file.

Nuclear spectra were extracted from a circular region centered on the positions given by NED[6]. We chose circular radii, aiming to include all possible photons, while excluding other sources or background effects. The radii are in the range between 2-4″ (see Table .1). The background was extracted from circular regions in the same chip that are free of sources and close to the object.

For the source and background spectral extractions, the DMEXTRACT task was used. The response matrix file (RMF) and ancillary reference file (RF) were generated for each source region using the MKACISRMF and MKWARF tasks, respectively. Finally, the spectra were binned to have a minimum of 20 counts per spectral bin using the GRPPHA task (included in FTOOLS), to be able to use the χ^2 statistics, as customary in X-ray spectroscopy.

3.2. XMM-Newton data

XMM-Newton observations were obtained with the EPIC pn camera (Strüder et al. 2001). The data were reduced in a systematic, uniform way using the Science nalysis Software (S S[7]), version 14.0.0. First, Good-Time Intervals (GTIs) were selected using a method that maximizes the signal-to-noise ratio of the net source spectrum by applying a different constant count rate threshold on the single events, E > 10 keV field-of-view background light curve. We extracted the spectra of the nuclei from circles of 20–35″ radius centered on the positions given by NED, while the background spectra were extracted from circular regions using an algorithm that automatically selects the best area - and the closest to the source - that is free of sources. This selection was manually checked to ensure the best selection for the backgrounds.

Source and background spectra were extracted with the EVSELECT task. The response matrix files (RMF) and the ancillary response files (RF) were generated using the RMFGE and ARFGE tasks, respectively. To be able to use the χ^2 statistics, the spectra were binned to obtain at least 20 counts per spectral bin using the GRPPHA task.

3.3. Light curves

Light curves in three energy bands (0.5–2.0 keV, 2.0–10.0 keV, and 0.5–10 keV) for the source and background regions as defined above were extracted using the DMEXTRACT task (for *XMM–Newton*) and EVSELECT task (for *Chandra*) with a 1000s bin. To be able to compare the variability amplitudes in different light curves of the same object, only those observations with a net exposure time longer than 30 ksec were taken into account. For observations longer than 40 ksec, the light curves were divided into segments of 40 ksec, so in some cases more than one segment of the same light curve can be extracted. Our light curves are occasionally affected by high particle background events ("flares"), whose flux dominates the observed count rates. We decided to remove these intervals from the source background-subtracted light curves due to their poor signal-to-noise ratio that could affect the estimate of the normalized effect variance (cf. Sect. 4.4). High particle background flux intervals were identified using the same algorithm described in Sect. 3.2. s the fraction of high particle background intervals is small, our procedure does not significantly affect the results discussed in this paper (Vaughan et al. 2003). We notice that after excluding these events, the exposure time of the light curve could be shorter, thus we recall that only observations with a net exposure time longer than 30 ksec were used for the analysis. The light curves are shown in ppendix D. We recall that the values of the continuum (median value of the count rate) and dashed (1 standard deviation) lines are used only for visual inspection of the data and not as estimators of the variability (as in Hernández-García et al. 2014).

4. Methodology

The methodology used in this work is presented in Hernández-García et al. (2013). Here we review the most important aspects but we refer the reader to this paper for details on the analysis.

4.1. Individual spectral analysis

The first step is to select a model to fit all the data of the same source simultaneously. For that purpose, we used five different models that were fitted to each spectrum individually. We notice that more complex models were also tested but they were not required by the data. The models are as follows:

- PL: single power law representing the continuum of a non-stellar source. The empirical model is $e^{N_{Gal}\ (E)} \cdot e^{N_H\ (E(1+z))}[N_H] \cdot Norme^{-\Gamma}[\Gamma, Norm]$.
- ME: The emission is dominated by hot diffuse gas, i.e., a thermal plasma. MEK L (in XSPEC) model is used to fit the spectrum. The model is $e^{N_{Gal}\ (E)} \cdot e^{N_H\ (E(1+z))}[N_H] \cdot MEK\ \ L[kT, Norm]$.

[4] http://cxc.harvard.edu/ciao4.4/
[5] http://cxc.harvard.edu/ciao/ahelp/lc_clean. html
[6] http://ned.ipac.caltech.edu/
[7] http://xmm.esa.int/sas/

- 2PL: In this model the primary continuum is an absorbed power law representing the non stellar source, while the soft energies are due to a scattering component that is represented by another power law. Mathematically the model is explained as
$e^{N_{Gal}\ (E)}\ e^{N_{H1}\ (E(1+z))}[N_{H1}]\ \cdot\ Norm_1 e^{-\Gamma}[\Gamma, Norm_1]\ +\ e^{N_{H2}\ (E(1+z))}[N_{H2}] \cdot Norm_2 e^{-\Gamma}[\Gamma, Norm_2])$.
- MEPL: The primary continuum is represented by an absorbed power law, but at soft energies a thermal plasma dominates the spectrum. Empirically it can be described as
$e^{N_{Gal}\ (E)}\ e^{N_{H1}\ (E(1+z))}[N_{H1}]\ \cdot\ MEK\ \ L[kT, Norm_1]\ +\ e^{N_{H2}\ (E(1+z))}[N_{H2}] \cdot Norm_2 e^{-\Gamma}[\Gamma, Norm_2])$.
- ME2PL: This is same model as MEPL, but an additional power law is required to explain the scattered component at soft energies, so mathematically it is
$e^{N_{Gal}\ (E)}\ e^{N_{H1}\ (E(1+z))}[N_{H1}]\ \cdot\ Norm_1 e^{-\Gamma}[\Gamma, Norm_1]\ +\ MEK\ \ L[kT] + e^{N_{H2}\ (E(1+z))}[N_{H2}] \cdot Norm_2 e^{-\Gamma}[\Gamma, Norm_2])$.

In the equations above, (E) is the photo-electric cross-section, z is the redshift, and $Norm_i$ are the normalizations of the power law and/or the thermal component. For each model, the parameters that vary are written in brackets. The Galactic absoption, N_{Gal}, is included in each model and fixed to the predicted value (Col. 5 in Table 1) using the tool H within FTOOLS (Dickey & Lockman 1990; Kalberla et al. 2005). Even if not included in the mathematical expressions above, all the models include three narrow Gaussian lines to take the iron lines at 6.4 keV (FeKα), 6.7 keV (FeXXV), and 6.95 keV (FeXXVI) into account.

The $\chi^2/d.o.f$ and F-test were used to select the simplest model that represents the data best. We considered an improvement of the spectral fit significant when the F-test results in a value lower than 10^{-5}.

4.2. Simultaneous spectral analysis

We determined the best-fit model for each individual observation using the procedure described in Sect. 4.1. s a baseline model we used the one corresponding to the individual observation with the largest count number, and we checked that it matches the best fit model of the remaining spectra of the same source[8]. This model was applied to all the observations of the same source simultaneously with its parameters linked amongst them – note that the values of the parameters are able to change from the initial values given in the baseline model. If this fit (SMF0) resulted in a good fit (see below), we considered the source as non-variable.

When SMF0 did not give a good resut, the next step was to let different parameters in the model vary one-by-one (SMF1). These parameters are the column densities at soft (N_{H1}) and hard (N_{H2}) energies, the temperature (kT), the spectral index (Γ), and the normalizations at soft ($Norm_1$) and hard ($Norm_2$) energies.

When SMF1 failed to be a good fit, we also tested to vary two parameters at the same time (SMF2), and also three parameters (SMF3) were needed in one case.

Each 'next step' (e.g., SMF1 versus SMF0) was always tested in order to confirm an improvement of the spectral fit. χ^2_r in the range between 0.9–1.5 –and as close as possible to the unity and an F-test value lower than 10^{-5} were the criteria to accept a new step. If different models at a given step yielded a significant improvement with respect to the previous step, we chose the model corresponding to the lowest χ^2_r.

Whenever possible, this analysis was applied to observations of the same satellite. However, in some cases there was only one observation per instrument available. In order to compare the data extracted from different apertures, we fit the extranuclear emission in the annular region in the *Chandra* image between the *Chandra* aperture around the nucleus and the *XMM–Newton* aperture (see Table .1) using the same procedure described in Sect. 4.1. This allowed us to define the best-fit model of the *Chandra* extranuclear emission. This model was included in the spectral analysis of the *XMM–Newton* data, when comparing with *Chandra* data. This procedure was applied whenever *XMM–Newton* and *Chandra* data were available.

4.3. Flux variability

The luminosities in the soft and hard X-ray energy bands were computed using XSPEC for both the fits of the individual observations, as well as for the simultaneous fit of all the observations together. The distances were taken from NED, corresponding to the average redshift-independent distance estimate for each object, when available, or to the redshift-estimated distance otherwise; distances are listed in Table 1.

When data from the optical monitor (OM) onboard *XMM–*Newton were available, UV luminosities (simultaneously to X-ray data) were estimated in the available filters. We recall that UVW2 is centered at 1894Å (1805-2454) Å, UVM2 at 2205Å (1970-2675) Å, and UVW1 at 2675Å (2410-3565) Å. We used the OM observation FITS source lists (OBSMLI)[9] to obtain the photometry. When OM data were not available, we searched for UV information in the literature. We note that in this case, the X-ray and UV data might not be simultaneous (see ppendix B).

We assumed an object to be variable when the square root of the squared errors was at least three times smaller than the dynamical range covered by the luminosities (see Hernández-García et al. 2014, for details).

4.4. Short-term variability

Initially, we assumed a constant count rate for segments of 30-40 ksec of the observation in each energy band and calculated χ^2/d.o.f. We considered the source as a variable candidate if the count rate differed from the average by more than 3 (or 99.7% probability).

Secondly, we calculated the normalized excess variance, $^2_{\rm NXS}$, for each light curve segment with 30-40 ksec following prescriptions in Vaughan et al. (2003) (see also González-Martín et al. 2011; Hernández-García et al. 2014). We recall that $^2_{\rm NXS}$ is related to the area below the power spectral density (PSD) shape.

When $^2_{\rm NXS}$ was negative or compatible with zero within the errors, we estimated the 90% upper limits using Table 1 in Vaughan et al. (2003). We assumed a PSD slope of -1, the upper limit from Vaughan et al. (2003), and we added the value of 1.282err($^2_{\rm NXS}$) to the limit to account for Poisson noise. For a number of segments, N, obtained from an individual light curve, an upper limit for the normalized excess variance was calculated. When N segments were obtained for the same light curve and at

[8] Note that for NGC 4138 we used the PL model because the *Chandra* spectrum did not have counts below 2 KeV, therefore the analysis was performed in the 2–10 keV band.

[9] ftp://xmm2.esac.esa.int/pub/odf/data/docs/XMM-SOC-GEN-ICD-0024.pdf

least one was consistent with being variable, we calculated the normalized weighted mean and its error as the weighted variance.

We considered short-term variations for $^{2}_{\rm NXS}$ detections above 3 of the confidence level.

4.5. Compton thickness

We tested the possibility of some sources being so heavily absorbed that their spectra can be completely reflected below 10 keV, i.e., Compton-thick sources. Since the Compton-thick column densities cannot be directly measured at the energies analyzed here, the following indirect indicators (using X-ray and [O III] data) are taken to classify these sources: $\Gamma < 1$. EW(FeKα) > 500 eV, and $F(2-10keV)/F_{[OIII]} < 1$ (Ghisellini et al. 1994; Bassani et al. 1999; Panessa & Bassani 2002). Where Γ and EW(FeKα) were obtained from individual spectral fits in the 3-10 keV energy band using the PL model, the extinction-corrected [O III] fluxes were obtained from the literature (and corrected when needed following Bassani et al. 1999), and the hard X-ray luminosities, $L(2-10keV)$, from the individual fits were used (see Table .3) for the calculation.

We considered that a source is a Compton-thick candidate when at least two of the three criteria above were met. Otherwise, the source is considered to be a Compton-thin candidate. When different observations of the same source result in different classifications, the object was considered to be a changing-look candidate.

5. Results

In this section we present the results of the spectral characteristics and variability patterns of the Seyfert 1.8/1.9 in the sample. For results on individual sources we refer the reader to ppendix B, as well as for notes and comparison with previous studies.

5.1. Spectral characteristics

We used five different models to fit each spectrum individually. The best model for each source resulted to be the same in all the individual observations from the same satellite. When comparing data from different instruments, different best fit models were selected for two sources (NGC 1365, and NGC 4138), most probably because of the low count-rate in the *Chandra* data, which required the simplest model. It is worth noticing that the *XMM–Newton* spectrum of NGC 4138 is best fitted with the ME2PL model, but the lack of counts in the *Chandra* spectrum below 2 keV forced us to perform the analysis only above 2 KeV and thus using the PL model (see ppendix B.11). The ME model was not the best-fit for any of the spectra.

The median [25% and 75% percentiles] values of the spectral parameters are presented in Table 3. bsorption at soft energies is usually compatible with the Galactic one (see Table .2). bsorption at high energies is common in these sources, being obscured in the range of $10^{21}-10^{23}cm^{-2}$, with median of $N_{H2} = 3.00[0.06-8.34]$ $10^{22}cm^{-2}$. The median value of the spectral indices is $\Gamma = 1.7[1.4-1.9]$, completely compatible with other GN (see e.g., Brightman & Nandra 2011a). The thermal component has a median of kT = 0.19[0.09-0.62] keV.

The X-ray luminosity medians in our sample are logL(0.5–2.0 keV)=41.9[41.2-42.6] and logL(2–10 keV)=42.5[41.7-42.7].

5.2. Compton-thickness

We recall that a source was classified as a Compton-thick candidate within an observation when at least two out of the three criteria explained in Sect. 4.5 were met. None of the sources are classified as Compton-thick. Two of the sources are classified as changing-look candidates (NGC 1365, and NGC 2992), as already reported in the literature (Gilli et al. 2000; Risaliti et al. 2009). nother two sources have been classified as changing-look candidates in the literature (M RK 609, Trippe et al. 2010 and NGC 2617, Shappee et al. 2014), but the present work does not detect these changes. It is worth noticing that we did not find the flux of the [$OIII$] in the literature for four sources (ESO 540-G01, ESO 195-IG21, ESO 113-G10, and NGC 2617), but the two other criteria were compatible with them being Compton-thin.

5.3. Long-term X-ray spectral variability

From the 15 nuclei in our sample, we compare spectra obtained from the same instrument in 10 cases, all of them observed by *XMM–Newton*, and in one case (NGC 4395) *Chandra* data are also available. In the remaining five sources only one observation per instrument was available.

Chandra and *XMM–Newton* data are available for the same source in eight cases (note that this analysis is independent of the one mentioned above, see Table .1), thus the simultaneous analysis was carried out by using the methodology explained in Sect. 4.2.

Long-term X-ray spectral variability is detected in all the 15 nuclei. Variations are detected in four parameters ($Norm_1$, $Norm_2$, N_{H1}, and N_{H2}). In nine objects the observed variability can be explained by varying only one parameter; in five nuclei varying two parameters is required (ESO 195-IG21, NGC 2617, NGC 2992, POX 52, and NGC 4395), and in NGC 1365 varying three parameters is required. The most frequent variations are found in $Norm_2$, which are observed in ten nuclei (ESO 540-G01, ESO 195-IG21, NGC 526 , NGC 1365, M RK 1218, NGC 2992, NGC 4138, NGC 4395, M RK 883, and IR S 20051-1117). Changes in N_{H2} are also frequent, as they are observed in six nuclei (NGC 1365, NGC 2617, NGC 2992, POX 52, NGC 4395, and NGC 4565). Variations at soft energies are detected in six sources (ESO 195-IG21, ESO 113-G01, M RK 609, NGC 1365, NGC 2617, and POX 52). mong them, only in two objects (ESO 195-IG21 and POX 52) these variations are reported for a simultaneous fit using *Chandra* and *XMM–Newton* together, thus these variations cannot be ascribed to the comparison of data obtained from different instruments.

5.4. Short-term X-ray variability

Short-term X-ray variations are analyzed in eight nuclei (Table .4). We recall that only light curves longer than 30 ksec were analyzed (see Sect. 4.4). Two sources do not show variations (POX 52 and NGC 4565) according to the $\chi^2/d.o.f$ and $^{2}_{NXS}$, whereas the remaining six are variable in at least one energy band. Four sources show variations in the total, soft, and hard energy bands (ESO 113-G10, NGC 526 , NGC 1365, and NGC 4395). mong these, all but NGC 1365 show variations above the 3 confidence level in the three energy bands. mong the eight observations analyzed for NGC 1365, four do not show variations in any band, two show variations in the total and hard bands, and another two show variations in the three

Table 2: Results of the variability analysis.

Name	log (L_{soft}) (0.5-2 keV)	log (L_{hard}) (2-10 keV)	log (R_{Edd})	Long-term variability SMF0	SMF1	SMF2/3	T_{max} (Years)	Short term	UV Variab.
(1)	(2)	(3)	(4)	(5)	(6)	(7)	(8)	(9)	(10)
ESO 540-G01 (X,C)	41.53±0.13	41.72±0.13	-	MEPL	$Norm_2$		1	-	-
	40%	38%			74%				
ESO 195-IG21 (X,C)	42.54±0.37	43.03±0.37	-	MEPL	$Norm_2$	$Norm_1$	4	-	-
	98%	97%			91%	98%			
ESO 113-G10 (X)	43.07±0.05	42.70±0.05	-0.74	ME2PL	$Norm_1$		4	TSH	W2
	17%	17%			40%				
NGC 526 (X)	42.91±0.10	43.32±0.09	-1.16	2PL	$Norm_2$	-	11	TSH	W1
	48%	46%			48%				
M RK 609 (X)	42.55±0.04	42.69±0.04	-	2PL	$Norm_1$		5	-	-
	13%	13%			22%				
NGC 1365 (X)^{CL}	41.15±0.35	42.18±0.42	-1.95	ME2PL	N_{H2}	$N2/N1$*	10	TSH	W1, M2
	81%	24%			68%	33/35%			
(X,C)	41.80±0.38	41.73±0.27		ME2PL	N_{H2}	$Norm_2$	2	-	-
	99%	77%			37%	30%			
NGC 2617 (X)	43.24±0.15	43.25±0.15	-0.94	2PL	$Norm_1$	N_{H2}	0.1	TS	W1
	46%	45%			59%	30%			
M RK 1218 (X)	41.87±0.22	42.56±0.21	-	PL	$Norm$		0.08	-	No
	64%	64%			63%				
NGC 2992 (X)^{CL}	41.57±0.23	42.03±0.22	-2.30	2PL	N_{H2}	$Norm_2$	3	TH	M2
	19%	19%			5%	21%			
POX 52 (X,C)	41.89±0.01	41.75±0.02	0.18	ME2PL	N_{H2}	N_{H1}	1	No	-
	2%	7%			44%	100%			
NGC 4138 (X,C)	-	41.53±0.07	-2.42	PL**	$Norm$		2	-	-
		21%			98%				
NGC 4395 (C)	39.50	39.94	-1.15	ME2PL	N_{H2}		0.003	-	W1
	0%	0%			31%				
(X)	39.69±0.06	40.28±0.40		ME2PL	N_{H2}	$Norm_2$	12	TSH	-
	15%	13%			20%	88%			
(X,C)	39.78±0.21	40.21±0.22		ME2PL	$Norm_2$		2	-	-
	61%	65%			93%				
NGC 4565 (X,C)	39.51±0.03	39.65±0.07	-4.63	PL	N_H		2	No	-
	11%	21%			48%				
M RK 883 (X)	42.42±0.09	42.71±0.08	-1.15	PL	$Norm$		4	-	W1, W2
	28%	28%			28%				
IR S 20051-1117 (X)	42.39±0.09	42.53±0.09	-1.16	PL	$Norm$		0.5	-	No
	29%	29%			29%				

N tes. (Col. 1) Name, and the instrument (C: *Chandra* and/or X: *XMM*–Newton) in parenthesis (^{CL} refer to changing-look candidates); (Cols. 2 and 3) logarithm of the soft (0.5–2 keV) and hard (2–10 keV) X-ray luminosities, where the mean was calculated for variable objects, and percentages in flux variations; (Col. 4) Eddington ratio, L_{bol}/L_{Edd}, calculated from Eracleous et al. (2010) using $L_{bol} = 33L_{2-10keV}$; (Col. 5) best fit for SMF0; (Col. 6) parameter varying in SMF1, with the percentage of variation; (Col. 7) parameter varying in SMF2 and SMF3 (for NGC 1365, *N1=$Norm_1$, and N2=$Norm_2$), with the percentage of variation; (Col. 8) the sampling timescale, corresponding to the difference between the first and the last observation. The percentages correspond to this T_{max}; (Col. 9) short-term variations in the total (T), soft (S), and/or hard (H) energy bands; and (Col. 10) filters where variations are detected at UV frequencies with the OM. '-' means that data were not available, while 'No' means that variations were not detected.

** Note that the *XMM–Newton* data of NGC 4138 is best fitted by the ME2PL model, but *Chandra* data does not have counts below 2 keV, thus the PL model is used for the simultaneous fit.

energy bands (both from 2012). NGC 2992 shows variations in the total and hard energy bands. Five observations were analyzed for this source, two of them not showing variations in any of the bands. NGC 2617 shows variations in the total and soft energy bands, in both cases above the 3 confidence level.

5.5. Long-term UV flux variability

UV data are available for nine sources. The remaining six sources do not have more than one *XMM–Newton* observations or different filters were used for the observations and thus cannot be directly compared.

mong the nine sources, two of them do not show UV variability (M RK 1218 and IR S 20051-1117), whereas the re-

Table 3: Median values and 25% and 75% percentiles of the spectral parameters of Seyfert 1.8/1.9 presented in this work (Col. 2) and the Seyfert 2 sample (Col. 3) presented in Hernández-García et al. (2015a).

(1)	Seyfert 1.8/1.9 (2)	Seyfert 2 (3)
log(L(0.5-2 keV) [erg s^{-1}])	$41.9^{42.6}_{41.2}$	$42.1^{42.6}_{41.3}$
log(L(2-10 keV) [erg s^{-1}])	$42.5^{42.7}_{41.7}$	$42.7^{42.8}_{42.5}$
N_{H2} ($10^{22}[cm^{-2}]$)	$3.00^{8.34}_{0.06}$	$22.2^{38.4}_{9.8}$
Γ	$1.7^{1.9}_{1.4}$	$1.7^{2.0}_{1.5}$
kT [keV]	$0.19^{0.38}_{0.09}$	$0.71^{0.81}_{0.67}/0.15^{0.18}_{0.12}$
S/N(0.5–2 KeV)	$5.3^{7.7}_{4.9}$	$5.2^{6.4}_{3.8}$
S/N(2–10 KeV)	$5.4^{6.6}_{4.7}$	$3.8^{5.2}_{2.3}$

N tes. (Col. 1) Spectral parameter, (Col. 2) average values for Seyfert 1.8/1.9, and (Col. 3) average values of Seyfert 2 from Hernández-García et al. (2015a). The two temperatures represent the two thermal components in the model.

maining seven sources show variations in at least one filter (see Table .1 and Fig. .1). We remind that all the reported variations are above the 3 confidence level.

6. Discussion

The optical and X-ray spectra of Seyfert 1.8/1.9 resembles those of Seyfert 2. For this reason, many studies aiming at analyzing the properties of obscured sources have included all these nuclei in the same samples (e.g., Risaliti et al. 1999; kylas & Georgantopoulos 2009; Malizia et al. 2012). However, a study of their variability properties compared to those of Seyfert 2 represents a powerful tool in revealing similarities and differences. In this work we can compare these properties in an homogeneous way for the first time using the results for Seyfert 1.8/1.9 presented here and the sample of Seyfert 2 presented in Hernández-García et al. (2015a).

6.1. Spectral properties

Fig. 2 shows the models used for Seyfert 1.8/1.9 and 2. The main conclusion is that Seyfert 2 require, in general, more complex models to fit the data. The difference cannot be attributed to different spectral qualities since the average signal-to-noise ratio(S/N) – which were estimated following Stoehr et al. (2008) – for each spectrum is similar for both type 1.8/1.9 and type 2 samples in the 0.5–2 keV and 2–10 keV energy bands (see Fig. 3). In Table 3, we show the median values [25% and 75% percentiles] of the spectral parameters for the Seyfert 1.8/1.9 and 2 nuclei. It can be seen that the main difference between these GN families is in N_{H2} (see also Fig. 4), in agreement with previous studies (Risaliti et al. 1999; Guainazzi et al. 2001; kylas & Georgantopoulos 2009; Brightman & Nandra 2011b). This is in fact the main reason why Seyfert 1.8/1.9 have been explained as nuclei that are less obscured than Seyfert 2, their difference being ascribed only to the absorbing material.

However, another difference is observed in the temperatures of the thermal emission, with Seyfert 2 having a bimodal distribution centred at $KT_1 \sim 0.7$ keV and $KT_2 \sim 0.2$ keV whereas Seyfert 1.8/1.9 show only one temperature regime centred at $KT \sim 0.2$ keV. Moreover the comparison with the study by Brightman & Nandra (2011a,b) on the 12 μm complete sample of Seyferts show that a thermal component is fitted in Seyfert 1-1.5 (Seyfert 2) in 15 (24) cases, with 12 (6) of them centred at 0.1 keV and three (18) centred at 0.7 keV. This result might indicate that the thermal component observed in Seyfert 1.8/1.9 is more similar to that observed in Seyfert 1 than to that in type 2.

In this context, it should be noticed that a more realistic physical model for the absorbing material in Seyfert 1.8/1.9 might be represented by ionised absorption (i.e., winds) instead of neutral absorption (i.e., the torus). We changed the neutral absorption by an ionised absorption in our models but the spectral fits were statistically the same (the fits did not improve at the 99.9% of confidence level using the F-test), except in the case of NGC 1365, where the presence of ionised absorption is well established (Risaliti et al. 2005a; Guainazzi et al. 2009). Since we cannot differentiate between neutral or ionised absorption due to the resolution of the spectra presented in this work, this issue should be explored using high spectral resolution data.

6.2. Short-term variability

Further information can be obtained from the analysis of the variability. X-ray short-term (i.e., intra-day) variations in Seyfert 2 galaxies were not detected in Hernández-García et al. (2015a), and thus all the measurements of $^{2}_{NXS}$ are upper limits. It is interesting to notice that most Seyfert 1 show changes at these timescales (Nandra et al. 1997; Turner et al. 1997), but variations at these timescales in a few Seyfert 2 have also been reported in the literature (e.g., González-Martín & Vaughan 2012). Even though the physical origin of these variations is not yet well settled, the involved timescales imply that they occur very close to the SMBH, and it has been suggested that accretion-disc/corona instabilities or variations in the accretion rate may be involved (Uttley et al. 2005; Breedt et al. 2010; McHardy 2010; Soldi et al. 2014). Fig. 5 shows the $^{2}_{NXS}$ in the 2–10 keV energy band against M_{BH} for the variable Seyfert 1.8/1.9 in our sample and the upper limits for the Seyfert 2 together with the results reported by Ponti et al. (2012) for the C IX 's sample, which include unobscured sources. For a proper comparison, we used their $^{2}_{NXS}$ calculated for light curve segments of 40 ksec. The green squares represent those sources with a width at half maximum (FMWH) of the H_β larger than 2500 $km\ s^{-1}$, the red triangles those with FMWH(H_β) < 2500 $km\ s^{-1}$, and the black hexagons the sources where they did not report the FMWH(H_β). It has been shown that the 2–10 keV power spectrum in GN follows a power law of slope $\Gamma \sim$-2 at high frequencies, which then flattens to a slope of $\Gamma \sim$-1 below a break frequency (Papadakis 2004; O'Neill et al. 2005; Miniutti et al. 2009). This model is named the universal power spectrum density (PSD) model because the integral of the PSD is equal to the $^{2}_{NXS}$ of a light curve (Vaughan et al. 2003). The dotted line in Fig. 5 represents this model as in Papadakis (2004, see also González-Martín et al. 2011), which was obtained for a sample of broad line Seyfert 1. For the relation, we used an Eddington ratio of R_{Edd} =[0.005,0.025,0.5], which is represented as a dotted, dash-dotted, and dashed lines in Fig. 5, respectively. It can be observed that the Seyfert 1.8/1.9 in our sample fit well both with this model and with the results reported by Ponti et al. (2012), as well as Seyfert 2 do. Thereof the short-term variability in Seyfert 1, Seyfert 1.8/1.9 and Seyfert 2 is consistent within the statistical uncertainties and thus we cannot provide evidence for a difference among the classes in this respect until the variations in Seyfert 2 are rejected.

6.3. Long-term variations

We found differences in the spectral variations between Seyfert 1.8/1.9 and Seyfert 2 in timescales from weeks to years. Variations at soft energies are only detected in Seyfert 1.8/1.9. The origin of the soft X-ray emission in Seyferts is under debate, maybe related to e.g., the possible dilution effect of scattering by photoionised gas (e.g., González-Martín et al. 2010) or to a warm absorber (W), consisting on ionized absorbing gas, that is observed in about 65% of Seyfert 1s (Laha et al. 2014), and it is highly variable (e.g., Winter et al. 2012; Laha et al. 2016, and references therein). However, the exposure times of the high resolution data (e.g., from the *Reflection Grating Spectrometer*) of the sources discussed in this paper are too short to constrain the properties of the soft X-ray emission, and thus the nature of the soft X-ray variations (e.g., Laha et al. 2011; Giustini et al. 2016).

t long timescales we find that Seyfert 1.8/1.9, as well as Seyfert 2 and LINERs, show hard X-ray variations in timescales between months and years, these changes being related to intrinsic variations of the hard nuclear continuum. This suggests that the emission mechanism is the same in these GN families. We have also computed the variability dynamical timescale against the time between the observations for the two families. We did not find differences in the variability of these sources, neither any obvious trend against the time difference. We notice that a caveat in our analysis might be that the observations were taken at random epochs, and thus the timescale between the observations do not refer to the variability timescales.

The GN continuum at X-rays comes from the Comptonization of photons from the inner parts of the accretion disk (Shakura & Sunyaev 1973). Thus, these long-term variations might be related to fluctuations in the inner accretion disk (e.g., Hernández-García et al. 2016). Moreover, variations due to absorbing clouds (i.e., N_H) are common in our sample, both in Seyfert 1.8/1.9 (six out of the 15, i.e., 40%) and 2s (four out of the 11 variable sources, i.e., 36%). However, these kind of eclipses are also observed in Seyfert 1s (Risaliti et al. 2011; Sanfrutos et al. 2013; Markowitz et al. 2014; gís-González et al. 2014). When it is possible to estimate the cloud velocity, and thus the location of the absorbing material, the clouds appear to be located very close to the BLR or within the borderline between the BLR and the torus (Risaliti et al. 2009, 2013; Nardini & Risaliti 2011; Walton et al. 2014; Connolly et al. 2014; Markowitz et al. 2014; Parker et al. 2015; Giustini et al. 2016). The velocities of the clouds in Seyfert 1.8/1.9 (NGC 1365, NGC 2617, NGC 2992, and NGC 4395) and Seyfert 2 (Mark 1210, and NGC 4507) in our sample are greater than $10^3 km/s$[10] (following the procedure in Risaliti et al. 2010). Therefore, these eclipses due to clouds passing through our line of sight seem to be happening at distances from the accretion disc consistent within or very close to the location of the BLR.

Furthermore, while variations at UV frequencies are not detected in Seyfert 2, these changes are observed in Seyfert 1.8/1.9 in the present work. The same behaviour is also seen in Seyfert 1s (e.g., Cardaci 2010; Netzer 2013). This result might indicate a less obstructed view of the accretion disk in Seyfert 1.8/1.9 compared to that of Seyfert 2, in agreement with the higher values of N_{H2} in Seyfert 2 compared to those of Seyfert 1.8/1.9.

s a final remark, we would like to warn the reader for the simplistic association of Seyfert 1.8/1.9 to Seyfert 2, since different variability properties are observed in the two GN groups both at X-ray and at UV frequencies. We leave open the possibility that Seyfert 1.8/1.9 behave more likely Seyfert 1, but a proper comparison between the properties of these families need to be done in a systematic and homogeneous way.

[10] Since the timescales between the observations were obtained at random, we can only estimate its velocities when the timescale is shorter than ~ 1 month.

7. Summary and conclusions

We have performed a spectral and variability analysis at X-ray and UV frequencies of a sample of fifteen galaxies classified as Seyfert 1.8/1.9 based on optical spectroscopy. The main results of the study can be summarized as follows:

- X-ray long-term variability is found in all the 15 nuclei. None of the sources are classified as Compton-thick candidates, and two of them have been classified as changing-look candidates.
- The main variability pattern is related to intrinsic changes in the sources, which are observed in ten nuclei. Changes in the column density are also frequent, as they are observed in six nuclei. Variations at soft energies are detected in six sources.
- X-ray short-term variations are detected in six out of the eight studied sources.
- Variations at UV frequencies are detected in seven out of the nine sources where data were available.

We have compared the properties of Seyfert 1.8/1.9 with the results of a sample of Seyfert 2 that were analyzed using the same methodology applied in this work (Hernández-García et al. 2015a), allowing a homogeneous comparison. The main conclusions obtained from this work are the following:

- The X-ray long term variations occur in a similar way in all the nuclei and are mainly related to intrinsic changes of the nuclear continuum. Variations in the absorbing column densities are also frequent in both GN families.
- X-ray short-term, soft X-ray, and UV long term variations are detected in Seyfert 1.8/1.9 but not in Seyfert 2, indicating that the view of the SMBH is unobstructed in Seyfert 1.8/1.9 and obstructed in Seyfert 2.
- We caution on the simplistic association of Seyfert 1.8/1.9 to Seyfert 2 to classify all of them as obscured sources, because they show different variability properties at X-ray and UV frequencies.

similar study of a sample of Seyfert 1 would be required in order to homogeneously compare their properties and to test whether Seyfert 1.8/1.9 are similar to these GN or not.

cknowledgements. We thank the anonymous referee for helpful comments. We acknowledge the GN group at the I for helpful comments during this work. This work was financed by MINECO grant Y 2010-15169, Y 2013-42227-P, and Junta de ndalucía TIC114. OGM acknowledges financial support from the UN M P PIIT I 100516 project. LHG and FP acknowledge the SI/IN F agreement number 2013-023-R1. This research made use of data obtained from the *Chandra* Data rchive provided by the *Chandra* X-ray Center (CXC). This research made use of data obtained from the *XMM*-Newton Data rchive provided by the *XMM*-Newton Science rchive (XS). This research made use of the N S /IP C extragalactic database (NED), which is operated by the Jet Propulsion Laboratory under contract with the National eronautics and Space dministration. We acknowledge the usage of the HyperLeda data base (http://leda.univ-lyon1.fr).

References

gís-González, B., Miniutti, G., Kara, E., et al. 2014, MNR S, 443, 2862

kylas, . & Georgantopoulos, I. 2009, & , 500, 999

ntonucci, R. 1993, R & , 31, 473

Barth, . J., Ho, L. C., Rutledge, R. E., & Sargent, W. L. W. 2004, pJ, 607, 90

Bassani, L., Dadina, M., Maiolino, R., et al. 1999, pJS, 121, 473

Baumgartner, W. H., Tueller, J., & Mushotzky, R. F. 2008, The stronomer's Telegram, 1794

Beckmann, V., Gehrels, N., & Tueller, J. 2007, pJ, 666, 122

Benítez, E., Méndez- breu, J., Fuentes-Carrera, I., et al. 2013, pJ, 763, 136

Braito, V., Ballo, L., Reeves, J. N., et al. 2013, MNR S, 428, 2516

Braito, V., Reeves, J. N., Gofford, J., et al. 2014, pJ, 795, 87

Breedt, E., McHardy, I. M., révalo, P., et al. 2010, MNR S, 403, 605

Brenneman, L. W., Risaliti, G., Elvis, M., & Nardini, E. 2013, MNR S, 429, 2662

Brightman, M. & Nandra, K. 2011a, MNR S, 413, 1206

Brightman, M. & Nandra, K. 2011b, MNR S, 414, 3084

Cackett, E. M., Fabian, . C., Zogbhi, ., et al. 2013, pJ, 764, L9

Cameron, D. T., McHardy, I., Dwelly, T., et al. 2012, MNR S, 422, 902

Cappi, M., Panessa, F., Bassani, L., et al. 2006, & , 446, 459

Cardaci, M. V. 2010, PhD thesis, Universidad utónoma de Madrid

Cohen, R. D., Puetter, R. C., Rudy, R. J., ke, T. B., & Foltz, C. B. 1986, pJ, 311, 135

Condon, J. J., Condon, M. ., Gisler, G., & Puschell, J. J. 1982, pJ, 252, 102

Condon, J. J., Yin, Q. F., Thuan, T. X., & Boller, T. 1998, J, 116, 2682

Connolly, S. D., McHardy, I. M., & Dwelly, T. 2014, rXiv e-prints

Coziol, R., Demers, S., Pena, M., et al. 1993, J, 105, 35

Dahari, O. & De Robertis, M. M. 1988, pJS, 67, 249

Dewangan, G. C., Mathur, S., Griffiths, R. E., & Rao, . R. 2008, pJ, 689, 762

Dickey, J. M. & Lockman, F. J. 1990, R & , 28, 215

Eracleous, M., Hwang, J. ., & Flohic, H. M. L. G. 2010, pJ, 711, 796

Fabian, . C., Lohfink, ., Kara, E., et al. 2015, MNR S, 451, 4375

Garmire, G. P., Bautz, M. W., Ford, P. G., Nousek, J. ., & Ricker, J. G. R. 2003, in Society of Photo-Optical Instrumentation Engineers (SPIE) Conference Series, Vol. 4851, Society of Photo-Optical Instrumentation Engineers (SPIE) Conference Series, ed. J. E. Truemper & H. D. Tananbaum, 28–44

Georgantopoulos, I., Papadakis, I., Zezas, ., & Ward, M. J. 2004, pJ, 614, 634

Georgantopoulos, I., Zezas, ., & Ward, M. J. 2003, pJ, 584, 129

Ghisellini, G., Haardt, F., & Matt, G. 1994, MNR S, 267, 743

Gilli, R., Maiolino, R., Marconi, ., et al. 2000, & , 355, 485

Giustini, M., Costantini, E., De Marco, B., et al. 2016, rXiv e-prints

Glass, I. S. 1997, MNR S, 292, L50

González-Martín, O., costa-Pulido, J. ., Perez Garcia, . M., & Ramos lmeida, C. 2010, pJ, 723, 1748

González-Martín, O., Papadakis, I., Reig, P., & Zezas, . 2011, & , 526, 132

González-Martín, O. & Vaughan, S. 2012, & , 544, 80

Goodrich, R. W. 1995, pJ, 440, 141

Griffiths, R. E., Schwartz, D. ., Schwarz, J., et al. 1979, pJ, 230, L21

Guainazzi, M., Fabian, . C., Iwasawa, K., Matt, G., & Fiore, F. 2005, MNR S, 356, 295

Guainazzi, M., Fiore, F., Matt, G., & Perola, G. C. 2001, MNR S, 327, 323

Guainazzi, M., Risaliti, G., Nucita, ., et al. 2009, & , 505, 589

Hernández-García, L., González-Martín, O., Márquez, I., & Masegosa, J. 2013, & , 556, 47

Hernández-García, L., González-Martín, O., Masegosa, J., & Márquez, I. 2014, & , 569, 26

Hernández-García, L., Masegosa, J., González-Martín, O., & Márquez, I. 2015a, & , submitted

Hernández-García, L., Masegosa, J., González-Martín, O., Márquez, I., & Perea, J. 2016, pJ, 824, 7

Hernández-García, L., Vaughan, S., Roberts, T. P., & Middleton, M. 2015b, MNR S, 453, 2877

Hickson, P., Kindl, E., & uman, J. R. 1989, pJS, 70, 687

Ho, L. C., Filippenko, . V., Sargent, W. L. W., & Peng, C. Y. 1997, pJS, 112, 391

Ho, L. C. & Ulvestad, J. S. 2001, pJS, 133, 77

Jorsater, S. & van Moorsel, G. . 1995, J, 110, 2037

Kalberla, P. M. W., Burton, W. B., Hartmann, D., et al. 2005, & , 440, 775

Kara, E., Zoghbi, ., Marinucci, ., et al. 2015, MNR S, 446, 737

Laha, S., Dewangan, G. C., & Kembhavi, . K. 2011, pJ, 734, 75

Laha, S., Guainazzi, M., Chakravorty, S., Dewangan, G. C., & Kembhavi, . K. 2016, MNR S, 457, 3896

Laha, S., Guainazzi, M., Dewangan, G. C., Chakravorty, S., & Kembhavi, . K. 2014, MNR S, 441, 2613

LaMassa, S. M., Heckman, T. M., Ptak, ., et al. 2011, pJ, 729, 52

LaMassa, S. M., Yaqoob, T., Ptak, . F., et al. 2014, pJ, 787, 61

Lawrence, ., Watson, M. G., Pounds, K. ., & Elvis, M. 1987, Nature, 325, 694

Maiolino, R. & Rieke, G. H. 1995, pJ, 454, 95

Maiolino, R., Salvati, M., Bassani, L., et al. 1998, & , 338, 781

Malizia, ., Bassani, L., Bazzano, ., et al. 2012, MNR S, 426, 1750

Markowitz, . G., Krumpe, M., & Nikutta, R. 2014, MNR S

Marquez, I. & Moles, M. 1996, & S, 120, 1

Matt, G., Guainazzi, M., & Maiolino, R. 2003, MNR S, 342, 422

McHardy, I. 2010, in Lecture Notes in Physics, Berlin Springer Verlag, Vol. 794, Lecture Notes in Physics, Berlin Springer Verlag, ed. T. Belloni, 203

McHardy, I., Connolly, S., Peterson, B., et al. 2016, rXiv e-prints

Minezaki, T., Yoshii, Y., Kobayashi, Y., et al. 2006, pJ, 643, L5

Miniutti, G., Ponti, G., Greene, J. E., et al. 2009, MNR S, 394, 443

Moran, E. C., Barth, . J., Kay, L. E., & Filippenko, . V. 2000, pJ, 540, L73

Moran, E. C., Eracleous, M., Leighly, K. M., et al. 2005, J, 129, 2108

Moran, E. C., Halpern, J. P., & Helfand, D. J. 1996, pJS, 106, 341

Mulchaey, J. S., Wilson, . S., & Tsvetanov, Z. 1996, pJS, 102, 309

Murphy, K. D., Yaqoob, T., & Terashima, Y. 2007, pJ, 666, 96

Mushotzky, R. F. 1982, pJ, 256, 92

Nagar, N. M., Falcke, H., Wilson, . S., & Ulvestad, J. S. 2002, & , 392, 53

Nagar, N. M., Wilson, . S., Mulchaey, J. S., & Gallimore, J. F. 1999, pJS, 120, 209

Nandra, K., George, I. M., Mushotzky, R. F., Turner, T. J., & Yaqoob, T. 1997, pJ, 476, 70

Nardini, E. & Risaliti, G. 2011, MNR S, 417, 2571

Netzer, H. 2013, The Physics and Evolution of ctive Galactic Nuclei

O'Neill, P. M., Kaspi, S., Laor, ., et al. 2006, pJ, 645, 160

O'Neill, P. M., Nandra, K., Papadakis, I. E., & Turner, T. J. 2005, MNR S, 358, 1405

Osterbrock, D. E. 1977, pJ, 215, 733

Osterbrock, D. E. 1981, pJ, 249, 462

Osterbrock, D. E. & Dahari, O. 1983, pJ, 273, 478

Osterbrock, D. E. & Martel, . 1993, pJ, 414, 552

Panessa, F. & Bassani, L. 2002, & , 394, 435

Panessa, F., Bassani, L., Cappi, M., et al. 2006, & , 455, 173

Panessa, F., Wolter, ., Pellegrini, S., et al. 2005, pJ, 631, 707

Papadakis, I. E. 2004, MNR S, 348, 207

Parker, M. L., Fabian, . C., Matt, G., et al. 2015, MNR S, 447, 72

Parker, M. L., Walton, D. J., Fabian, . C., & Risaliti, G. 2014, MNR S, 441, 1817

Peterson, B. M. 1997, n Introduction to ctive Galactic Nuclei (Cambridge University Press)

Pietsch, W., Bischoff, K., Boller, T., et al. 1998, & , 333, 48

Polletta, M., Bassani, L., Malaguti, G., Palumbo, G. G. C., & Caroli, E. 1996, pJS, 106, 399

Ponti, G., Papadakis, I., Bianchi, S., et al. 2012, & , 542, 83

Porquet, D., Uttley, P., Reeves, J. N., et al. 2007, & , 473, 67

Rees, M. J. 1984, R & , 22, 471

Risaliti, G. 2002, & , 386, 379

Risaliti, G., Bianchi, S., Matt, G., et al. 2005a, pJ, 630, L129

Risaliti, G., Elvis, M., Bianchi, S., & Matt, G. 2010, MNR S, 406, L20

Risaliti, G., Elvis, M., Fabbiano, G., Baldi, ., & Zezas, . 2005b, pJ, 623, L93

Risaliti, G., Elvis, M., Fabbiano, G., et al. 2007, pJ, 659, L111

Risaliti, G., Elvis, M., & Nicastro, F. 2002, pJ, 571, 234

Risaliti, G., Harrison, F. ., Madsen, K. K., et al. 2013, Nature, 494, 449

Risaliti, G., Maiolino, R., & Salvati, M. 1999, pJ, 522, 157

Risaliti, G., Miniutti, G., Elvis, M., et al. 2009, pJ, 696, 160

Risaliti, G., Nardini, E., Salvati, M., et al. 2011, MNR S, 410, 1027

Rivers, E., Risaliti, G., Walton, D. J., et al. 2015, pJ, 804, 107

Sanfrutos, M., Miniutti, G., gís-González, B., et al. 2013, MNR S, 436, 1588

Shakura, N. I. & Sunyaev, R. . 1973, & , 24, 337

Shappee, B. J., Prieto, J. L., Grupe, D., et al. 2014, pJ, 788, 48

Shi, Y., Rieke, G. H., Smith, P., et al. 2010, pJ, 714, 115

Shu, X. W., Yaqoob, T., Murphy, K. D., et al. 2010, pJ, 713, 1256

Singh, V., Shastri, P., & Risaliti, G. 2011, & , 532, 84

Smith, J. E., Robinson, ., lexander, D. M., et al. 2004, MNR S, 350, 140

Soldi, S., Beckmann, V., Baumgartner, W. H., et al. 2014, & , 563, 57

Stoehr, F., White, R., Smith, M., et al. 2008, in stronomical Society of the Pacific Conference Series, Vol. 394, stronomical Data nalysis Software and Systems XVII, ed. R. W. rgyle, P. S. Bunclark, & J. R. Lewis, 505

Strüder, L., Briel, U., Dennerl, K., et al. 2001, & , 365, L18

Terashima, Y. & Wilson, . S. 2003, pJ, 583, 145

Thornton, C. E., Barth, . J., Ho, L. C., Rutledge, R. E., & Greene, J. E. 2008, pJ, 686, 892

Tremaine, S., Gebhardt, K., Bender, R., et al. 2002, pJ, 574, 740

Trippe, M. L., Crenshaw, D. M., Deo, R., & Dietrich, M. 2008, J, 135, 2048

Trippe, M. L., Crenshaw, D. M., Deo, R. P., et al. 2010, pJ, 725, 1749

Trippe, M. L., Reynolds, C. S., Koss, M., Mushotzky, R. F., & Winter, L. M. 2011, pJ, 736, 81

Turner, T. J., George, I. M., Nandra, K., & Mushotzky, R. F. 1997, pJS, 113, 23

Turner, T. J. & Pounds, K. . 1989, MNR S, 240, 833

Ulvestad, J. S. 1986, pJ, 310, 136

Ulvestad, J. S. & Wilson, . S. 1984, pJ, 278, 544

Urry, C. M. & Padovani, P. 1995, P SP, 107, 803

Uttley, P. 2007, in stronomical Society of the Pacific Conference Series, Vol. 373, The Central Engine of ctive Galactic Nuclei, ed. L. C. Ho & J.-W. Wang, 149

Uttley, P., McHardy, I. M., & Vaughan, S. 2005, MNR S, 359, 345

Vasudevan, R. V. & Fabian, . C. 2009, MNR S, 392, 1124

Vaughan, S., Edelson, R., Warwick, R. S., & Uttley, P. 2003, MNR S, 345, 1271

Vaughan, S., Iwasawa, K., Fabian, . C., & Hayashida, K. 2005, MNR S, 356, 524

Véron-Cetty, M.-P. & Véron, P. 2010, & , 518, 10

Walton, D. J., Risaliti, G., Harrison, F. ., et al. 2014, pJ, 788, 76

Wang, J.-M. & Zhang, E.-P. 2007, pJ, 660, 1072

Ward, M., Penston, M. V., Blades, J. C., & Turtle, . J. 1980, MNR S, 193, 563

Whittle, M. 1992, pJS, 79, 49

Winkler, H. 1992, MNR S, 257, 677

Winter, L. M., Veilleux, S., McKernan, B., & Kallman, T. R. 2012, pJ, 745, 107

Wrobel, J. M. & Ho, L. C. 2006, pJ, 646, L95

Zdziarski, . ., Johnson, W. N., Done, C., Smith, D., & McNaron-Brown, K. 1995, pJ, 438, L63

Zhang, Y.-H. 2011, pJ, 726, 21

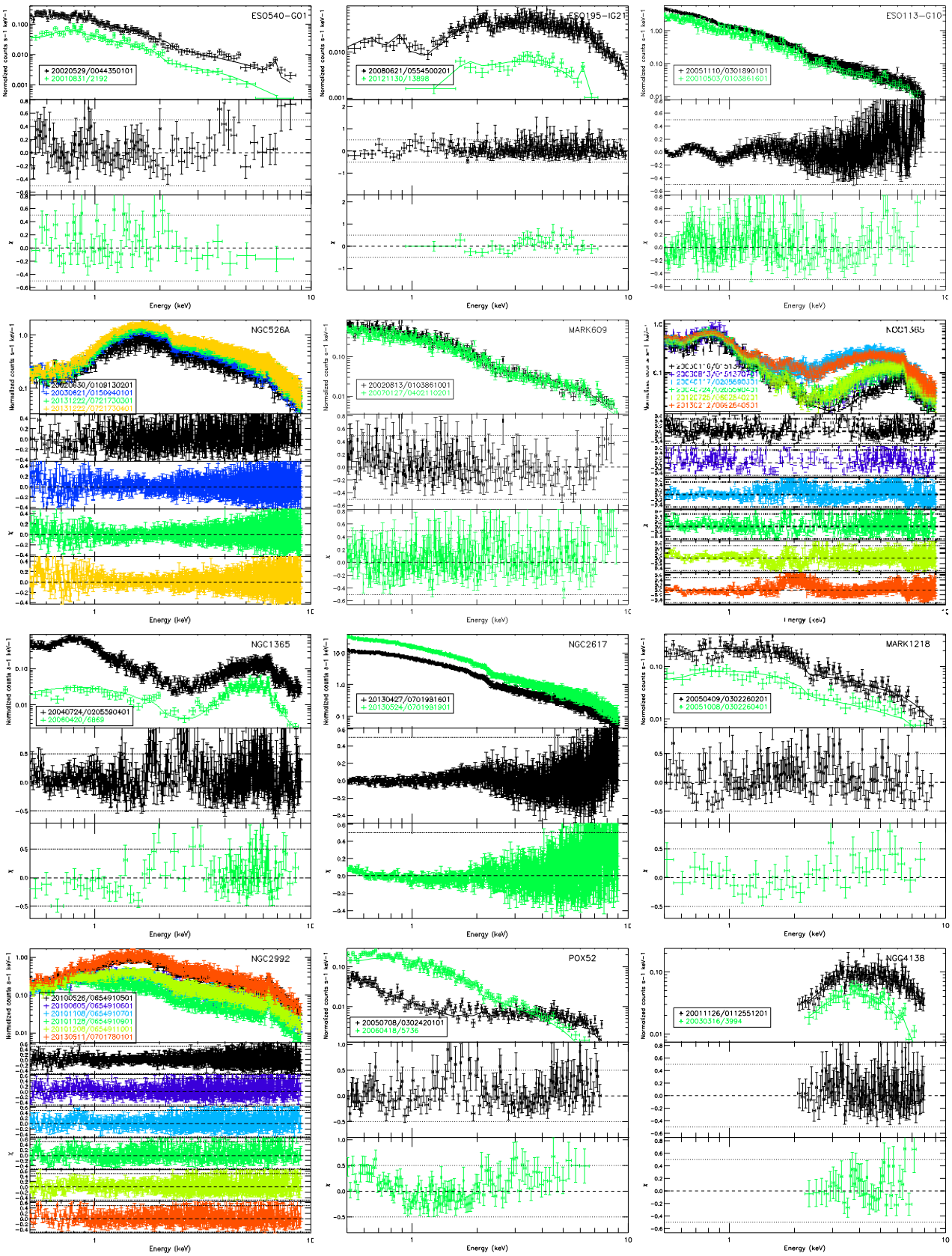

Fig. 1: For each object, (top): simultaneous fit of X-ray spectra; (from second row on): residuals in units of . The legends contain the date (in the format yyyymmdd) and the obsID. Details are given in Table 1.

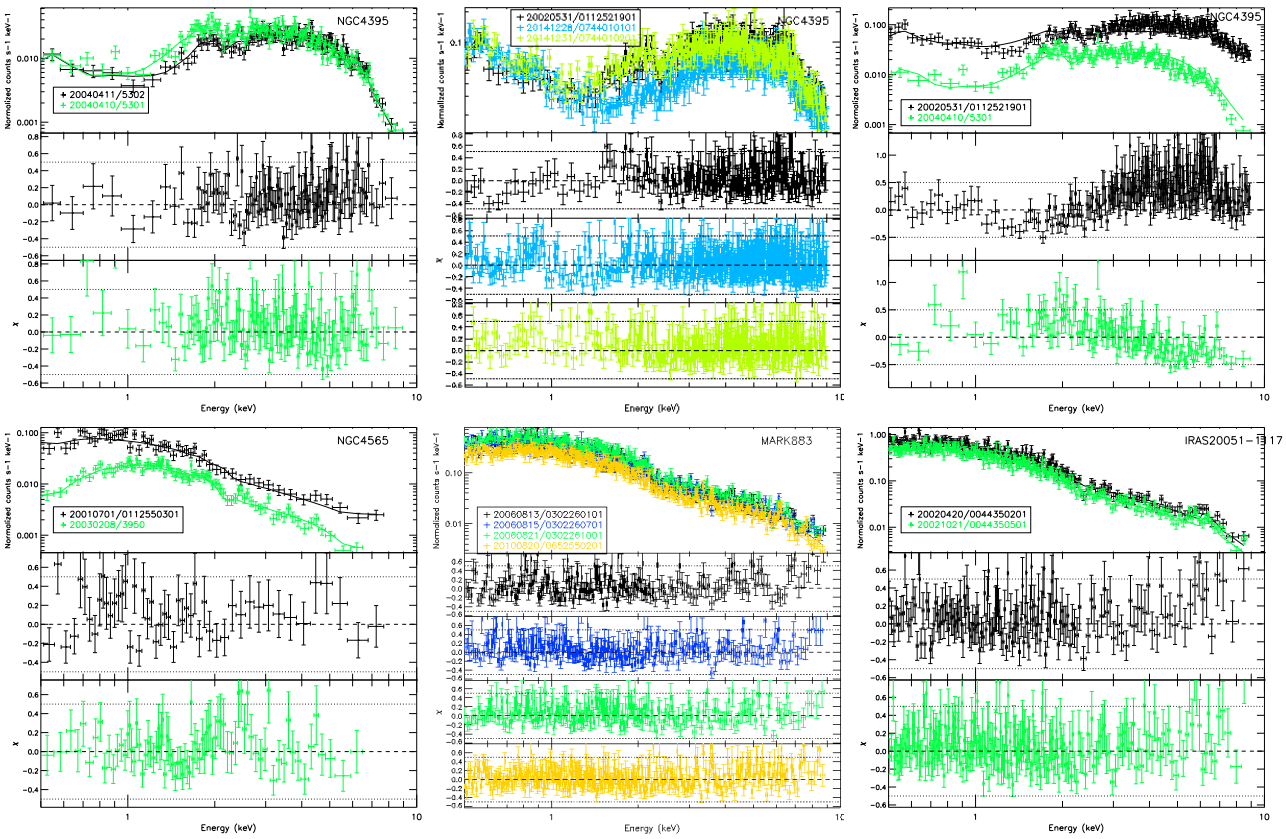
NGC4395
+ 20040411/5302
+ 20040410/5301
NGC4395
+ 20020531/0112521901
+ 20141228/0744010101
+ 20141231/0744010401
NGC4395
+ 20020531/0112521901
+ 20040410/5301
NGC4565
+ 20010701/0112550301
+ 20030208/3950
MARK883
+ 20060813/0302260101
+ 20060815/0302260701
+ 20060821/0302261001
+ 20100820/0652550201
IRAS20051−1317
+ 20020420/0044350201
+ 20021021/0044350501
Normalized counts s−1 keV−1
Energy (keV)
χ

Fig. 1: Cont.

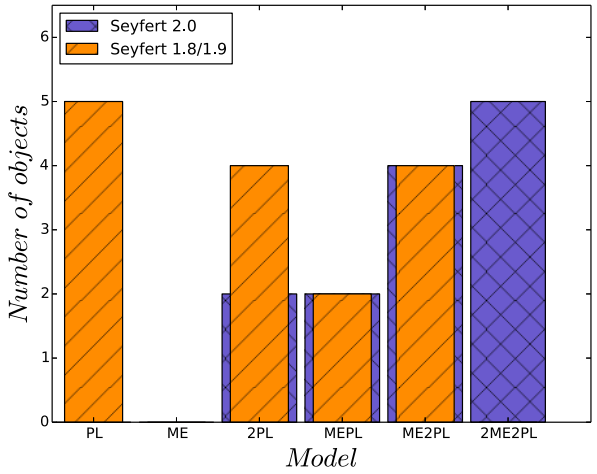

Fig. 2: Histogram of the best fit models for Seyfert 1.8/1.9 and 2.

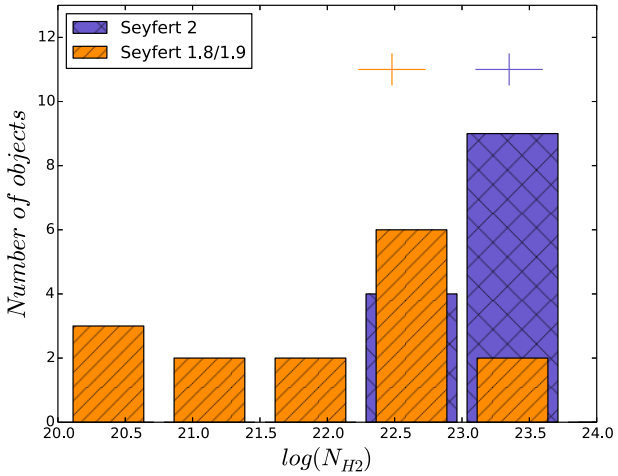

Fig. 4: Histogram of the column density, N_{H2}, for Seyfert 1.8/1.9 and Seyfert 2 in logarithmic scale. The crosses represent the median values.

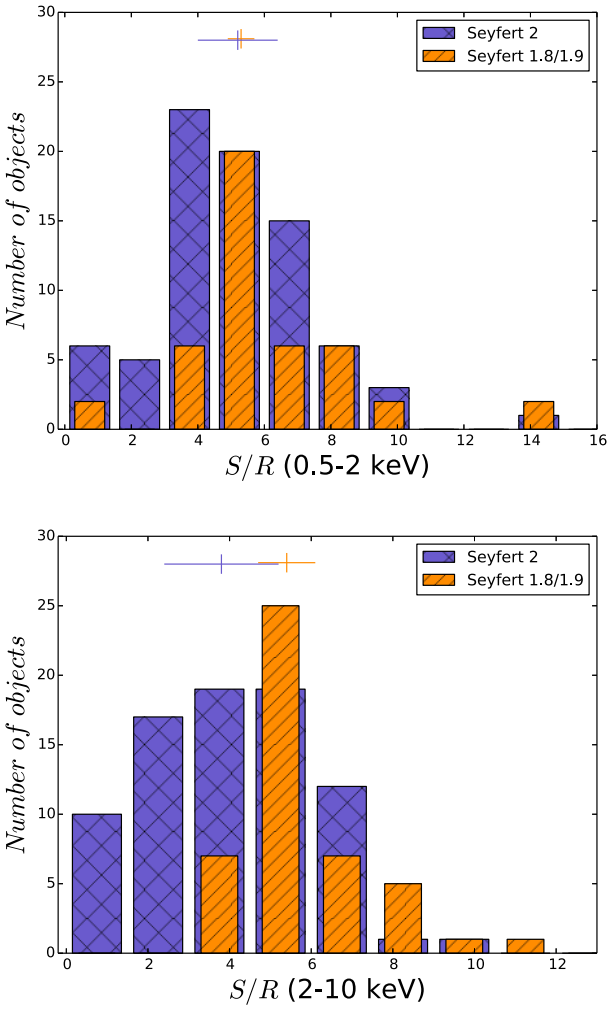

Fig. 3: Histogram of the signal-to-noise ratio, S/R, for the individual spectra of Seyfert 1.8/1.9 and Seyfert 2 in the soft (0.5–2 keV, upper panel) and hard (2–10 keV, bottom panel) energy bands. The crosses represent the median values.

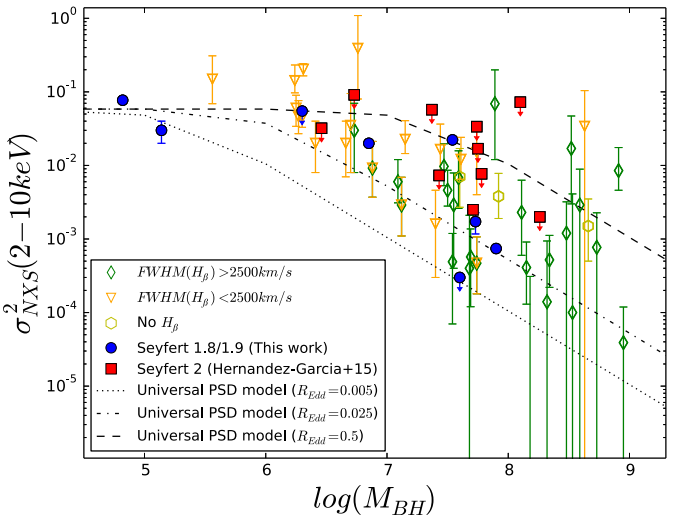

Fig. 5: Normalized excess variance, $^{2}_{NXS}$, against the black hole mass, M_{BH} for the Seyfert 1.8/1.9 in the sample (blue circles) and Seyfert 2 in (Hernández-García et al. 2015a, red squares). Results for the C IX sample using light curve segments of 40 ksec (Ponti et al. 2012) are presented, including sources with (FMWH(H_β >2500 $km\ s^{-1}$ (green diamonds), FMWH(H_β) < 2500 $km\ s^{-1}$ (orange triangles), and those with no H_β (yellow hexagons). The dotted, dash-dotted, and dashed lines are the universal PSD model, represented as a broken power law (Papadakis 2004) using R_{Edd} =[0.005, 0.025, 0.5].

ppendix : Tables

Table .1: Observational details.

Name	Instrument	ObsID	Date	R ($''$)	Net Exptime (ksec)	Counts	OM Filter	log(L_{UV}) (erg/s)
(1)	(2)	(3)	(4)	(5)	(6)	(7)	(8)	(9)
ESO 540-G01	*Chandra*[c]	2192	2001-08-31	3	20	1316	-	
	XMM-Newton[c]	0044350101	2002-05-29	25	11	2728	UVW2	43.26^{+}0.04
							UVW1	43.41^{+}0.01
ESO 195-IG21	*Chandra*[c]	13898	2012-11-30	2	20	529	-	
	XMM-Newton[c]	0554500201	2008-06-21	20	25	6165		Not detected
ESO 113-G10	*XMM-Newton*	0103861601	2001-05-03	25	4	10419	UVW2	42.68^{+}0.06
	XMM-Newton	0301890101	2005-11-10	25	77	304379	UVW2	42.87^{+}0.02
							UVM2	42.94^{+}0.01
							UVW1	43.02^{+}0.01
NGC 526	*XMM-Newton*[c]	0109130201	2002-06-30	35	8	20949	UVM2	42.13^{+}0.08
							UVW1	42.27^{+}0.03
	XMM-Newton	0150940101	2003-06-21	35	35	118532	UVW2	41.99^{+}0.07
							UVM2	42.15^{+}0.04
							UVW1	42.41^{+}0.01
	XMM-Newton	0721730301	2013-12-22	35	48	177241	-	
	XMM-Newton	0721730401	2013-12-22	35	37	164811	-	
	Chandra[c]	342	2000-02-07	4	9	1158	-	
M RK 609	*XMM-Newton*	0103861001	2002-08-13	20	7	5054	UVW2	43.32^{+}0.04
	XMM-Newton	0402110201	2007-01-27	20	16	10002	UVM2	43.37^{+}0.01
NGC 1365	*Chandra*[c]	6869	2006-04-20	2	15	2021	-	
	XMM-Newton	0151370101	2003-01-16	20	14	10599	UVW2	41.71^{+}0.02
	XMM-Newton	0151370201	2003-02-09	20	3	1481	-	
	XMM-Newton	0151370701	2003-08-13	20	6	6337	UVW2	41.71^{+}0.03
	XMM-Newton	0205590301	2004-01-17	20	50	83303	UVW1	41.69^{+}0.01
							UVM2	41.30^{+}0.02
	XMM-Newton[c]	0205590401	2004-07-24	20	29	30181	UVW1	42.21^{+}0.01
							UVM2	41.95^{+}0.01
	XMM-Newton	0505140201	2007-06-30	20	42	26349	UVW1	42.07^{+}0.01
							UVM2	41.35^{+}0.02
	XMM-Newton	0505140401	2007-07-02	20	78	49947	UVW1	42.08^{+}0.01
	XMM-Newton	0505140501	2007-07-04	20	46	29528	UVW1	42.24^{+}0.01
							UVM2	42.04^{+}0.01
	XMM-Newton	0692840201	2012-07-25	20	106	115167	UVW1	42.01^{+}0.01
	XMM-Newton	0692840301	2012-12-24	20	95	276846	UVW1	41.94^{+}0.01
	XMM-Newton	0692840401	2013-01-23	20	89	366687	UVW1	41.78^{+}0.01
	XMM-Newton	0692840501	2013-02-12	20	102	172790	UVW1	41.77^{+}0.01
NGC 2617	*XMM-Newton*	0701981601	2013-04-27	25	39	574119	UVW2	42.95^{+}0.02
							UVM2	43.02^{+}0.01
							UVW1	43.05^{+}0.01
	XMM-Newton	0701981901	2013-05-24	25	14	496297	UVW1	43.24^{+}0.01
M RK 1218	*XMM-Newton*	0302260201	20050409	20	6	3652	UVW2	41.98^{+}0.25
							UVM2	42.12^{+}0.09
							UVW1	42.43^{+}0.03
	XMM-Newton	0302260401	20051008	20	3	935	UVM2	42.06^{+}0.10
NGC 2992	*XMM-Newton*	0654910501	2010-05-26	25	35	85124	UVM2	41.14^{+}0.08
	XMM-Newton	0654910601	2010-06-05	25	33	35540	UVM2	41.28^{+}0.05
	XMM-Newton	0654910701	2010-11-08	25	37	40296		Not detected
	XMM-Newton	0654910901	2010-11-28	25	33	20874		Not detected

Table .1: (Cont.)

Name	Instrument	ObsID	Date	R	Net Exptime	Counts	OM Filter	log(L_{UV})
				($''$)	(ksec)			(erg/s)
(1)	(2)	(3)	(4)	(5)	(6)	(7)	(8)	(9)
	XMM-Newton	0654911001	2010-12-08	25	38	44100	UVW2	$40.70^{+}_{-}0.33$
							UVM2	$41.24^{+}_{-}0.03$
							UVW1	$41.87^{+}_{-}0.01$
	XMM-Newton	0701780101	2013-05-11	25	9	26676	UVM2	$41.09^{+}_{-}0.06$
POX 52	*Chandra*[c]	5736	2006-04-18	2	22	4979	-	
	XMM-Newton[c]	0302420101	2005-07-08	20	69	4869	UVM2	$42.21^{+}_{-}0.03$
NGC 4138	*Chandra*[c]	3994	2003-03-16	2	6	889	-	
	XMM-Newton[c]	0112551201	2001-11-26	25	8	4271	-	
NGC 4395	*Chandra*	5302	2004-04-11	2	28	2779	-	
	Chandra[c]	5301	2004-04-10	2	27	3105	-	
	XMM-Newton[c]	0112521901	2002-05-31	25	8	5209	UVW1	$40.09^{+}_{-}0.02$
	XMM-Newton	0744010101	2014-12-28	25	36	16941	UVW1	$39.99^{+}_{-}0.01$
	XMM-Newton	0744010201	2014-12-31	25	14	8819	UVW1	$40.07^{+}_{-}0.01$
NGC 4565	*XMM-Newton*[c]	0112550301	2001-07-01	20	9	1209	-	
	Chandra[c]	3950	2003-02-08	2	59	2158	-	
M RK 883	*XMM-Newton*	0302260101	2006-08-13	25	8	5311	UVW2	$42.99^{+}_{-}0.08$
							UVM2	$42.92^{+}_{-}0.04$
							UVW1	$43.01^{+}_{-}0.02$
	XMM-Newton	0302260701	2006-08-15	25	10	7307	UVW2	$42.85^{+}_{-}0.06$
							UVM2	$42.91^{+}_{-}0.04$
							UVW1	$43.02^{+}_{-}0.02$
	XMM-Newton	0302261001	2006-08-21	25	8	7000	UVW2	$42.75^{+}_{-}0.06$
							UVM2	$42.94^{+}_{-}0.04$
							UVW1	$43.03^{+}_{-}0.02$
	XMM-Newton	0652550201	2010-08-20	25	26	12409	UVW1	$43.13^{+}_{-}0.01$
IR S 2005-1117	*XMM-Newton*	0044350201	2002-04-20	20	4	4535	UVW2	$42.65^{+}_{-}0.09$
							UVW1	$43.03^{+}_{-}0.01$
	XMM-Newton	0044350501	2002-10-21	20	10	7020	UVW1	$43.01^{+}_{-}0.02$

N tes. (Col. 1) name, (Col. 2) instrument, (Col. 3) obsID, (Col. 4) date, (Col. 5) aperture radius for the nuclear extraction, (Col. 6) net exposure time, (Col. 7) number of counts in the 0.5-10 keV band, (Cols. 8 and 9) UV luminosity from the optical monitor and filter. The *c* represents data from different instruments that were compared as explained in Sect. 4.2.

Table .2: Final compilation of the best-fit models for the sample, including the individual best-fit model for each observation, and the simultaneous best-fit model (i.e., SMF0, SMF1, SMF2, or SMF3) with the varying parameters (except for SMF0). Note that when the column density is compatible with the Galactic absorption, a '-' is placed.

nalysis	ObsID	Model	N_{H1}	N_{H2}	kT	Γ	$Norm_1$	$Norm_2$	$\chi^2/d.o.f$
					keV		(10^{-4})	(10^{-4})	F-test
(1)	(2)	(3)	(4)	(5)	(6)	(7)	(8)	(9)	(10)
					ESO 540-G01				
Ind	2192	MEPL	$0^{0.45}_{0}$	$0.04^{0.14}_{0}$	$0.36^{0.52}_{0.20}$	$1.89^{2.15}_{1.69}$	$0.17^{2.73}_{0.08}$	$0.69^{0.84}_{0.55}$	46.20/42
Ind	0044350101	MEPL	-	$0.75^{1.15}_{0.63}$	$0.65^{0.80}_{0.33}$	$1.82^{1.90}_{1.74}$	$0.90^{0.99}_{0.81}$	$0.08^{6.03}_{0.01}$	87.51/92
SMF (+ring)	0044350101	MEPL	-	-	$0.38^{0.55}_{0.31}$	$1.68^{1.76}_{1.61}$	$0.15^{0.20}_{0.10}$	$0.87^{0.93}_{0.82}$	137.15/142
	2129						$0.57^{0.62}_{0.53}$		
					ESO 195-IG21				
Ind	13898	MEPL	$5.34^{8.25}_{3.07}$	$10.43^{19.62}_{5.98}$	$0.27^{1.11}_{0.14}$	$2.42^{0}_{1.17}$	$252.77^{330.35}_{2.03}$	$9.58^{135.83}_{5.05}$	15.09/16
Ind	0554500201	MEPL	$0.79^{0.93}_{0.68}$	$3.39^{3.69}_{3.11}$	$0.14^{0.17}_{0.11}$	$1.32^{1.43}_{1.22}$	$46.69^{308.08}_{11.98}$	$4.87^{5.82}_{4.10}$	274.21/262
SMF (+ring)	0554500201	MEPL	$0.27^{2.11}_{0.00}$	$3.81^{4.65}_{3.15}$	$2.67^{4.85}_{0.38}$	$1.35^{1.48}_{1.24}$	$0.47^{2.23}_{0.13}$	$5.15^{6.43}_{4.21}$	270.70/255
	2012						$0.04^{0.12}_{0.01}$	$0.08^{0.14}_{0.03}$	

Table .2: (Cont.)

nalysis	ObsID	Model	N_{H1}	N_{H2}	kT keV	Γ	$Norm_1$ (10^{-4})	$Norm_2$ (10^{-4})	$\chi^2/d.o.f$ F-test
(1)	(2)	(3)	(4)	(5)	(6)	(7)	(8)	(9)	(10)
				ESO 113-G10					
Ind	0103861601	ME2PL	-	$1.57^{2.82}_{0.99}$	$0.07^{0.09}_{0.07}$	$3.27^{3.40}_{3.18}$	$6.07^{7.37}_{6.07}$	$6.12^{12.09}_{2.72}$	277.61/236
Ind	0301890101	ME2PL	-	$4.02^{4.35}_{3.73}$	$0.07^{0.08}_{0.07}$	$2.63^{2.66}_{2.60}$	$14.76^{14.96}_{14.76}$	$19.33^{20.76}_{17.97}$	2080.8/1088
SMF1	0103861601	ME2PL	-	$3.62^{3.87}_{3.41}$	$0.08^{0.09}_{0.07}$	$2.67^{2.70}_{2.65}$	$8.95^{9.17}_{8.73}$	$20.48^{21.91}_{19.13}$	2281.77/1302
	0301890101						$14.81^{14.91}_{14.70}$		
				NGC 526					
Ind	0109130201	2PL	$0.01^{0.06}_{0}$	$1.14^{1.24}_{1.08}$	-	$1.38^{1.43}_{1.34}$	$1.08^{1.58}_{0.97}$	$25.31^{27.13}_{23.72}$	706.22/732
Ind	0150940101	2PL	$0.03^{0.05}_{0}$	$1.17^{1.21}_{1.14}$	-	$1.48^{1.50}_{1.46}$	$1.25^{1.49}_{1.04}$	$39.74^{40.86}_{38.67}$	1609.78/1538
Ind	0721730301	2PL	$0.03^{0.05}_{0.01}$	$1.25^{1.28}_{1.22}$	-	$1.49^{1.50}_{1.47}$	$1.37^{1.58}_{1.19}$	$46.44^{47.53}_{45.37}$	1718.2/1638
Ind	0721730401	2PL	$0.06^{0.09}_{0.03}$	$1.23^{1.27}_{1.20}$	-	$1.50^{1.51}_{1.48}$	$1.71^{2.02}_{1.44}$	$55.94^{57.30}_{54.64}$	1747.04/1614
Ind	342	2PL	$0.73^{1.04}_{0.69}$	$120.02^{185.04}_{64.85}$	-	$0.97^{1.25}_{0.84}$	$2.40^{2.78}_{1.99}$	$16.32^{25.17}_{4.02}$	61.32/45
SMF1	0109130201	2PL	$0.03^{0.04}_{0.02}$	$1.21^{1.23}_{1.20}$	-	$1.48^{1.49}_{1.47}$	$1.36^{1.48}_{1.24}$	$28.49^{29.02}_{27.97}$	5863.99/5543
	0150940101							$40.16^{40.74}_{39.59}$	
	0721730301							$45.72^{46.38}_{45.07}$	
	0721730401							$55.12^{55.93}_{54.33}$	
				M RK 609					
Ind	0103861001	2PL	-	$10.43^{149.71}_{5.28}$	-	$1.96^{2.03}_{1.89}$	$3.78^{3.89}_{3.67}$	$2.21^{46.21}_{1.18}$	183.79/173
Ind	0402110201	2PL	-	$12.62^{24.95}_{7.69}$	-	$1.81^{1.89}_{1.78}$	$2.90^{2.96}_{2.84}$	$2.45^{3.31}_{1.80}$	359.17/319
SMF1	0103861001	2PL	-	$11.41^{17.41}_{7.16}$	-	$1.89^{1.93}_{1.85}$	$3.71^{3.81}_{3.61}$	$2.58^{3.16}_{1.95}$	566.07/499
	0402110201						$2.91^{2.97}_{2.85}$		
				NGC 1365					
Ind	6869	2PL	$0^{0.05}_{0}$	$35.98^{38.60}_{33.47}$	-	$1.53^{1.76}_{1.35}$	$0.46^{0.54}_{0.43}$	$38.56^{61.78}_{27.19}$	126.46/89
Ind	0151370101	ME2PL	-	$40.07^{42.76}_{37.58}$	$0.64^{0.66}_{0.61}$	$1.90^{1.96}_{1.83}$	$1.60^{1.76}_{1.59}$	$56.68^{66.66}_{48.52}$	421.94/359
Ind	0151370201	ME2PL	-	$13.30^{22.30}_{8.30}$	$0.73^{0.82}_{0.65}$	$2.02^{2.22}_{1.83}$	$1.57^{2.01}_{1.57}$	$9.21^{14.60}_{5.56}$	70.21/49
Ind	0151370701	ME2PL	$0^{0.04}_{0}$	$32.58^{34.62}_{30.26}$	$0.68^{0.71}_{0.65}$	$2.12^{2.38}_{2.04}$	$1.71^{2.02}_{1.59}$	$97.42^{188.31}_{97.41}$	335.83/232
Ind	0205590301	ME2PL	$0.06^{0.06}_{0.05}$	$11.95^{12.12}_{11.81}$	$0.62^{0.63}_{0.60}$	$2.18^{2.22}_{2.17}$	$2.65^{2.80}_{2.65}$	$130.56^{144.97}_{125.17}$	2751.27/1504
Ind	0205590401	ME2PL	-	$25.86^{26.41}_{24.72}$	$0.62^{0.64}_{0.61}$	$2.03^{2.08}_{1.98}$	$1.65^{1.77}_{1.65}$	$80.55^{88.22}_{72.16}$	1181.26/778
Ind	0505140201	ME2PL	-	$52.73^{59.11}_{46.76}$	$0.65^{0.66}_{0.64}$	$2.20^{2.25}_{2.16}$	$1.53^{1.62}_{1.52}$	$25.72^{30.56}_{21.58}$	632.85/444
Ind	0505140401	ME2PL	-	$64.17^{65.92}_{60.03}$	$0.64^{0.65}_{0.63}$	$2.15^{2.20}_{2.13}$	$1.57^{1.63}_{1.57}$	$45.38^{50.70}_{41.01}$	977.71/681
Ind	0505140501	ME2PL	-	$60.11^{66.62}_{54.24}$	$0.63^{0.65}_{0.62}$	$2.14^{2.17}_{2.10}$	$1.57^{1.65}_{1.57}$	$35.33^{41.61}_{30.12}$	700.17/499
Ind	0692840201	ME2PL	-	$26.07^{26.43}_{25.71}$	$0.65^{0.66}_{0.64}$	$2.12^{2.15}_{2.10}$	$1.69^{1.72}_{1.66}$	$104.65^{115.25}_{104.65}$	2186.8/1529
Ind	0692840301	ME2PL	-	$3.66^{3.72}_{3.60}$	$0.61^{0.64}_{0.58}$	$1.40^{1.42}_{1.39}$	$4.91^{5.06}_{4.91}$	$33.35^{34.32}_{32.41}$	5588.28/1703
Ind	0692840401	ME2PL	$0.09^{0.09}_{0.09}$	$1.99^{2.02}_{1.97}$	67.07^{0}_{0}	$1.65^{1.67}_{1.64}$	$10.95^{11.28}_{10.95}$	$46.00^{47.33}_{45.13}$	4283.19/1697
Ind	0692840501	ME2PL	-	$12.30^{12.43}_{12.14}$	$0.63^{0.64}_{0.62}$	$1.74^{1.76}_{1.73}$	$2.73^{2.80}_{2.73}$	$61.81^{63.43}_{59.72}$	2817.83/1687
SMF3	0151370101	ME2PL	-	$39.40^{41.93}_{37.04}$	$0.62^{0.62}_{0.61}$	$1.63^{1.64}_{1.62}$	$1.63^{1.69}_{1.58}$	$58.68^{63.43}_{54.30}$	10738.3/6122
	0151370701			$31.17^{33.02}_{29.45}$			$1.74^{1.83}_{1.66}$	$73.99^{79.27}_{69.02}$	
	0205590301			$10.44^{10.59}_{10.28}$			$2.07^{2.11}_{2.03}$	$79.99^{82.13}_{77.90}$	
	0205590401			$25.36^{26.07}_{24.67}$			$1.79^{1.80}_{1.75}$	$65.26^{67.77}_{62.82}$	
	0692840201			$25.18^{25.52}_{24.84}$			$1.77^{1.80}_{1.75}$	$74.12^{76.25}_{72.03}$	
	0692840501			$12.77^{12.93}_{12.62}$			$2.52^{2.55}_{2.49}$	$87.64^{89.91}_{85.42}$	
SMF2 (+ring)	0205590401	ME2PL	-	$27.74^{28.95}_{25.62}$	<0.69	$2.26^{2.51}_{2.18}$	$0.31^{0.37}_{0.24}$	$140.24^{185.74}_{99.61}$	1388.72/873
	6869			$44.27^{45.58}_{40.82}$				$199.22^{259.85}_{158.50}$	
				NGC 2617					
Ind	0701981601	2PL	-	$11.93^{13.65}_{10.44}$	-	$2.01^{2.02}_{2.00}$	$71.01^{71.21}_{70.80}$	$39.95^{42.55}_{37.52}$	1903.22/1564
Ind	0701981901	2PL	-	$10.07^{11.77}_{8.61}$	-	$2.15^{2.16}_{2.14}$	$0.02^{0.02}_{0.02}$	$0.01^{0.01}_{0.01}$	1861.39/1469
SMF2	0701981601	2PL	-	$6.88^{7.54}_{6.25}$	-	$2.08^{2.09}_{2.07}$	$70.05^{70.28}_{69.81}$	$49.41^{51.41}_{47.49}$	4431.52/3039
	0701981901			$9.80^{10.98}_{8.75}$			$170.94^{171.43}_{170.46}$		
				M RK 1218					
Ind	0302260201	PL	$0.09^{0.12}_{0.06}$	-	-	$1.12^{1.20}_{1.06}$	-	-	187.44/146
Ind	0302260401	PL	-	-	-	$0.81^{0.94}_{0.74}$	-	-	27.40/30

Table .2: (Cont.)

nalysis	ObsID	Model	N_{H1}	N_{H2}	kT	Γ	$Norm_1$	$Norm_2$	$\chi^2/d.o.f$
					keV		(10^{-4})	(10^{-4})	F-test
(1)	(2)	(3)	(4)	(5)	(6)	(7)	(8)	(9)	(10)
SMF1	0302260201	PL	$0.06^{0.09}_{0.03}$	-	-	$1.05^{1.12}_{1.00}$	$2.49^{2.72}_{2.31}$	-	231.136/181
							$0.91^{1.00}_{0.84}$		
				NGC 2992					
Ind	0654910501	2PL	$0.16^{0.19}_{0.12}$	$0.93^{1.02}_{0.85}$	-	$1.50^{1.53}_{1.48}$	$4.78^{5.88}_{3.74}$	$20.42^{21.35}_{19.45}$	1460.82/1412
Ind	0654910601	2PL	$0.12^{0.14}_{0.10}$	$1.18^{1.47}_{0.92}$	-	$1.38^{1.44}_{1.32}$	$3.93^{4.35}_{3.42}$	$4.05^{4.70}_{3.44}$	1078.77/947
Ind	0654910701	2PL	$0.11^{0.14}_{0.08}$	$0.99^{1.24}_{0.77}$	-	$1.37^{1.42}_{1.32}$	$3.72^{4.21}_{3.09}$	$4.22^{4.78}_{3.66}$	1012.9/1016
Ind	0654910901	2PL	$0.05^{0.07}_{0.03}$	$8.13^{57.00}_{2.36}$	-	$1.22^{1.34}_{1.10}$	$2.65^{2.83}_{2.48}$	$0.54^{1.21}_{0.48}$	676.2/664
Ind	0654911001	2PL	$0.08^{0.11}_{0.05}$	$0.85^{1.03}_{0.69}$	-	$1.37^{1.42}_{1.33}$	$2.99^{3.59}_{2.29}$	$5.79^{6.33}_{5.24}$	1106.19/1078
Ind	0701780101	2PL	$0.09^{0.17}_{0}$	$0.81^{0.95}_{0.70}$	-	$1.50^{1.55}_{1.46}$	$3.36^{5.75}_{1.68}$	$27.24^{28.99}_{25.32}$	818.68/821
SMF2	0654910501	2PL	$0.09^{0.09}_{0.08}$	$0.76^{0.78}_{0.74}$	-	$1.43^{1.44}_{1.41}$	$2.99^{3.07}_{2.90}$	$19.52^{20.00}_{19.06}$	6291.22/5968
	0654910601			$0.95^{1.01}_{0.89}$				$5.51^{5.73}_{5.30}$	
	0654910701			$0.88^{0.93}_{0.83}$				$5.53^{5.74}_{5.33}$	
	0654910901			$7.44^{10.37}_{5.36}$				$1.76^{2.02}_{1.53}$	
	0654911001			$0.93^{0.98}_{0.88}$				$6.56^{6.79}_{6.34}$	
	0701780101			$0.72^{0.74}_{0.69}$				$24.66^{25.32}_{24.02}$	
				POX 52					
Ind	5736	ME2PL	-	$3.23^{4.44}_{2.36}$	$0.22^{0.25}_{0.20}$	$2.62^{2.78}_{2.44}$	$2.32^{2.69}_{2.32}$	$4.25^{6.13}_{2.65}$	122.38/117
Ind	0302420101	ME2PL	-	$6.59^{7.39}_{5.79}$	$0.16^{0.18}_{0.14}$	$1.79^{1.98}_{1.60}$	$0.11^{0.13}_{0.11}$	$1.33^{1.89}_{0.92}$	244.71/174
SMF (+ring)	0302420101	ME2PL	$8.38^{10.43}_{7.36}$	$2.43^{4.28}_{1.30}$	$0.15^{0.17}_{0.11}$	$2.30^{2.34}_{2.26}$	$2.76^{2.98}_{2.05}$	$0.30^{1.00}_{0.10}$	378.76/290
	5736		-	$4.32^{5.41}_{3.51}$					
				NGC 4138					
Ind	3994	PL	$7.92^{9.95}_{6.62}$	-	-	$1.36^{1.93}_{1.01}$	-	-	34.66/35
Ind	0112551201	PL(2–10 keV)	$7.89^{8.82}_{7.00}$	-	-	$1.44^{1.62}_{1.26}$		$0.14^{0.19}_{0.10}$	153.80/162
SMF (+ring)	0112551201	PL(2–10 keV)	$6.76^{9.55}_{4.22}$	-	-	$1.20^{1.83}_{0.61}$	$0.19^{0.86}_{0.01}$	-	186.04/190
	2003						$8.91^{26.70}_{3.16}$		
				NGC 4395					
Ind	5302	ME2PL	-	$4.00^{4.52}_{3.52}$	$0.09^{0.17}_{0.05}$	$1.13^{1.33}_{0.94}$	$0.07^{0.12}_{0.07}$	$3.99^{5.52}_{2.90}$	99.62/108
Ind	5301	ME2PL	-	$3.40^{3.76}_{3.04}$	$0.08^{0.22}_{0.03}$	$1.52^{1.83}_{1.30}$	$0.14^{0.16}_{0.11}$	$5.98^{10.70}_{5.98}$	183.22/121
SMF1	5302	ME2PL	-	$4.34^{4.69}_{3.99}$	$0.09^{0.16}_{0.05}$	$1.37^{1.50}_{1.24}$	$0.11^{0.13}_{0.09}$	$5.50^{6.81}_{4.46}$	265.8/238
	5301			$3.01^{3.29}_{2.74}$					
Ind	0112521901	ME2PL	$5.71^{6.45}_{5.11}$	$0.04^{0.23}_{0}$	$0.16^{0.21}_{0.09}$	$1.29^{1.52}_{1.12}$	$6.75^{11.53}_{6.75}$	$0.35^{0.49}_{0.29}$	261.70/220
Ind	0744010101	ME2PL	-	$8.14^{8.63}_{7.67}$	$0.19^{0.20}_{0.18}$	$1.27^{1.35}_{1.18}$	$0.30^{0.34}_{0.29}$	$8.06^{9.51}_{6.84}$	601.99/590
Ind	0744010201	ME2PL	-	$4.78^{5.20}_{4.56}$	$0.18^{0.21}_{0.14}$	$1.16^{1.26}_{1.05}$	$0.36^{0.47}_{0.35}$	$7.49^{8.93}_{6.14}$	369.14/344
SMF2	0112521901	ME2PL	-	$5.81^{6.21}_{5.43}$	$0.19^{0.20}_{0.18}$	$1.20^{1.26}_{1.14}$	$0.33^{0.35}_{0.31}$	$9.40^{10.55}_{8.37}$	1217.45/1170
	0744010101			$7.94^{8.34}_{7.56}$				$70.83^{79.57}_{63.06}$	
	0744010201			$4.66^{4.96}_{4.38}$				$80.75^{90.29}_{72.23}$	
SMF1 (+ring)	0112521901	ME2PL	$2.87^{3.20}_{2.55}$	$13.58^{16.19}_{11.38}$	$0.25^{0.27}_{0.24}$	$1.42^{1.64}_{1.26}$	$5.31^{6.82}_{4.23}$	$10.17^{17.25}_{6.54}$	460.32/350
	5301							$0.76^{3.00}_{0.01}$	
				NGC 4565					
Ind	0112550301	PL	$0.11^{0.16}_{0.07}$	-	-	$1.80^{1.99}_{1.67}$	-	-	46.52/46
Ind	3950	PL	$0.25^{0.28}_{0.22}$	-	-	$1.96^{2.05}_{1.85}$	-	-	71.19/77
SMF (+ring)	0112550301	PL	$0.13^{0.17}_{0.10}$	-	-	$1.94^{2.05}_{1.85}$	$0.78^{0.86}_{0.71}$	-	121.88/128
	3950		$0.25^{0.29}_{0.22}$						
				M RK 883					
Ind	0302260101	PL	$0.04^{0.06}_{0.02}$	-	-	$1.61^{1.68}_{1.54}$	-	-	206.37/191
Ind	0302260701	PL	$0.04^{0.06}_{0.02}$	-	-	$1.64^{1.71}_{1.59}$	-	-	269.11/249
Ind	0302261001	PL	$0.07^{0.08}_{0.05}$	-	-	$1.75^{1.81}_{1.69}$	-	-	221.43/243
Ind	0652550201	PL	$0.04^{0.05}_{0.03}$	-	-	$1.66^{1.71}_{1.62}$	-	-	438.40/407
SMF1	0302260101	PL	$0.05^{0.05}_{0.04}$	-	-	$1.67^{1.70}_{1.64}$		$3.67^{3.80}_{3.54}$	1151.81/1105
	0302260701							$3.64^{3.76}_{3.52}$	

Table .2: (Cont.)

nalysis	ObsID	Model	N_{H1}	N_{H2}	kT keV	Γ	$Norm_1$ (10^{-4})	$Norm_2$ (10^{-4})	$\chi^2/d.o.f$ F-test
(1)	(2)	(3)	(4)	(5)	(6)	(7)	(8)	(9)	(10)
	0302261001							$4.62^{4.77}_{4.47}$	
	0652550201							$2.66^{2.74}_{2.59}$	
				IR S 20051-1117					
Ind	0044350201	PL	-	-	-	$1.89^{1.94}_{1.85}$	-	-	171.36/160
Ind	0044350501	PL	-	-	-	$1.93^{1.96}_{1.89}$	-	-	246.53/245
SMF1	0044350201	PL	-	-	-	$1.91^{1.94}_{1.88}$	-	$5.88^{6.04}_{5.73}$	425.12/410
	0044350501							$4.17^{4.26}_{4.08}$	

Table .3: X-ray luminosities.

			Individual		Simultaneous	
Name	Satellite	ObsID	log(L(0.5-2 keV))	log(L(2-10 keV))	log(L(0.5-2 keV))	log(L(2-10 keV))
(1)	(2)	(3)	(4)	(5)	(6)	(7)
ESO 540-G01	*XMM–Newton*	0044350101	$43.38^{43.40}_{43.36}$	$41.83^{41.86}_{41.79}$	$41.63^{41.65}_{41.62}$	$41.81^{41.84}_{41.77}$
	Chandra (3″)	2192	$41.49^{41.54}_{41.42}$	$41.55^{44.12}_{41.02}$	$41.41^{41.43}_{41.39}$	$41.60^{41.64}_{41.57}$
	Chandra (25″)	2192	$41.80^{41.87}_{41.73}$	$41.65^{43.67}_{40.99}$		
ESO 195-IG21	*XMM–Newton*	0554500201	$43.46^{43.50}_{43.41}$	$43.31^{43.32}_{43.30}$	$42.83^{42.93}_{42.70}$	$43.32^{43.34}_{43.31}$
	Chandra (2″)	13898	$44.41^{44.55}_{44.22}$	$42.88^{43.29}_{42.31}$	$41.08^{41.43}_{40.99}$	$41.76^{41.87}_{41.62}$
	Chandra (20″)	13898	$42.24^{42.37}_{42.06}$	$42.74^{43.48}_{42.25}$		
ESO 113-G10	*XMM–Newton*	0103861601	$42.67^{42.76}_{42.55}$	$42.60^{42.80}_{42.21}$	$43.03^{43.05}_{43.01}$	$42.66^{42.67}_{42.66}$
	XMM–Newton	0301890101	$43.11^{43.11}_{43.11}$	$42.76^{42.76}_{42.75}$	$43.11^{43.12}_{43.10}$	$42.74^{42.74}_{42.73}$
NGC 526	*XMM–Newton*	0109130201	$42.69^{42.70}_{42.69}$	$43.17^{43.17}_{43.16}$	$42.74^{42.75}_{42.74}$	$43.16^{43.16}_{43.15}$
	XMM–Newton	0150940101	$42.88^{42.88}_{42.88}$	$43.29^{43.30}_{43.29}$	$42.89^{42.89}_{42.88}$	$43.30^{43.30}_{43.29}$
	XMM–Newton	0721730301	$42.95^{42.95}_{42.94}$	$43.35^{43.36}_{43.35}$	$42.94^{42.94}_{42.94}$	$43.35^{43.35}_{43.35}$
	XMM–Newton	0721730401	$43.03^{43.03}_{43.03}$	$43.43^{43.43}_{43.42}$	$43.02^{43.02}_{43.02}$	$43.43^{43.43}_{43.43}$
	Chandra (4″)	342	$42.55^{42.59}_{42.50}$	$43.09^{43.19}_{42.97}$		
	Chandra (35″)	342	$41.87^{41.90}_{41.84}$	$42.58^{42.62}_{42.55}$		
M RK 609	*XMM–Newton*	0103861001	$42.55^{42.56}_{42.54}$	$42.67^{42.69}_{42.64}$	$42.58^{42.59}_{42.57}$	$42.72^{42.74}_{42.71}$
	XMM–Newton	0402110201	$42.50^{42.51}_{42.49}$	$42.69^{42.71}_{42.68}$	$42.52^{42.53}_{42.51}$	$42.66^{42.68}_{42.65}$
NGC 1365	*XMM–Newton*	0151370101	$41.72^{41.73}_{41.71}$	$41.86^{41.87}_{41.84}$	$41.48^{41.49}_{41.47}$	$41.78^{41.79}_{41.77}$
	XMM–Newton	0151370201	$40.97^{40.99}_{40.95}$	$41.08^{41.12}_{41.04}$		
	XMM–Newton	0151370701	$41.94^{41.95}_{41.93}$	$41.97^{41.99}_{41.96}$	$40.45^{40.47}_{40.44}$	$42.82^{42.83}_{42.80}$
	XMM–Newton	0205590301	$42.11^{42.12}_{42.11}$	$42.02^{42.03}_{42.02}$	$41.62^{41.63}_{41.62}$	$41.93^{41.93}_{41.92}$
	XMM–Newton	0205590401	$41.83^{41.84}_{41.83}$	$41.90^{41.91}_{41.89}$	$39.98^{39.99}_{39.98}$	$39.95^{39.96}_{39.94}$
	XMM–Newton	0505140201	$41.37^{41.38}_{41.37}$	$41.33^{41.34}_{41.32}$		
	XMM–Newton	0505140401	$41.60^{41.60}_{41.60}$	$41.59^{41.59}_{41.58}$		
	XMM–Newton	0505140501	$41.50^{41.50}_{41.49}$	$41.49^{41.50}_{41.48}$		
	XMM–Newton	0692840201	$41.97^{41.98}_{41.97}$	$41.98^{41.98}_{41.97}$	$40.38^{40.38}_{40.38}$	$41.50^{41.51}_{41.50}$
	XMM–Newton	0692840301	$41.54^{41.54}_{41.54}$	$42.00^{42.00}_{42.00}$		
	XMM–Newton	0692840401	$41.71^{41.74}_{41.67}$	$42.00^{42.01}_{41.98}$		
	XMM–Newton	0692840501	$41.75^{41.75}_{41.74}$	$41.99^{41.99}_{41.98}$	$40.76^{40.76}_{40.76}$	$41.90^{41.90}_{41.90}$
	XMM–Newton (2″)	0205590401			$42.10^{42.17}_{42.02}$	$41.94^{41.97}_{41.92}$
	Chandra (2″)	6869	$41.45^{41.49}_{41.41}$	$41.86^{41.90}_{41.81}$	$39.69^{39.95}_{38.94}$	$41.31^{41.34}_{41.27}$
	Chandra (20″)	6869	$41.93^{41.95}_{41.92}$	$42.03^{42.05}_{42.01}$		
NGC 2617	*XMM–Newton*	0701981601	$43.06^{43.06}_{43.05}$	$43.12^{43.12}_{43.11}$	$43.08^{43.08}_{43.08}$	$43.10^{43.10}_{43.10}$
	XMM–Newton	0701981901	$43.46^{43.46}_{43.46}$	$43.42^{43.43}_{43.42}$	$43.35^{43.35}_{43.34}$	$43.36^{43.37}_{43.36}$
M RK 1218	*XMM–Newton*	0302260201	$42.09^{42.11}_{42.08}$	$42.70^{42.72}_{42.68}$	$42.04^{42.05}_{42.02}$	$42.73^{42.75}_{42.71}$
	XMM–Newton	0302260401	$41.56^{41.59}_{41.53}$	$42.35^{43.12}_{42.21}$	$41.60^{41.63}_{41.57}$	$42.29^{42.33}_{42.26}$

Table .3: (Cont.)

			Individual		Simultaneous	
Name	Satellite	ObsID	log(L(0.5-2 keV))	log(L(2-10 keV))	log(L(0.5-2 keV))	log(L(2-10 keV))
(1)	(2)	(3)	(4)	(5)	(6)	(7)
NGC 2992	*XMM–Newton*	0654910501	$41.83^{41.84}_{41.83}$	$42.23^{42.24}_{42.23}$	$41.79^{41.79}_{41.79}$	$42.24^{42.24}_{42.24}$
	XMM–Newton	0654910601	$41.35^{41.35}_{41.34}$	$41.84^{41.84}_{41.83}$	$41.37^{41.37}_{41.36}$	$41.83^{41.84}_{41.82}$
	XMM–Newton	0654910701	$41.34^{41.35}_{41.34}$	$41.83^{41.84}_{41.83}$	$41.37^{41.37}_{41.36}$	$41.83^{41.84}_{41.83}$
	XMM–Newton	0654910901	$41.07^{41.08}_{41.07}$	$41.60^{41.60}_{41.59}$	$41.11^{41.12}_{41.11}$	$41.59^{41.60}_{41.58}$
	XMM–Newton	0654911001	$41.38^{41.39}_{41.38}$	$41.88^{41.88}_{41.87}$	$41.42^{41.42}_{41.41}$	$41.88^{41.88}_{41.87}$
	XMM–Newton	0701780101	$41.92^{41.92}_{41.91}$	$42.32^{42.33}_{42.31}$	$41.88^{41.89}_{41.87}$	$42.33^{42.33}_{42.32}$
POX 52	*XMM–Newton*	0302420101	$41.55^{41.57}_{41.53}$	$41.74^{41.76}_{41.72}$	$41.89^{41.92}_{41.87}$	$41.76^{41.78}_{41.74}$
	Chandra (2″)	5736	$42.26^{42.27}_{42.25}$	$41.92^{42.78}_{41.89}$	$41.88^{41.89}_{41.86}$	$41.73^{41.75}_{41.71}$
	Chandra (20″)	5736	$42.29^{42.30}_{42.28}$	$41.94^{41.98}_{41.90}$		
NGC 4138	*XMM–Newton*	0112551201	-	$41.47^{41.49}_{41.46}$	-	$41.48^{41.49}_{41.46}$
	Chandra (2″)	3994	-	$41.54^{41.66}_{41.36}$	-	$41.58^{41.76}_{41.27}$
	Chandra (25″)	3994	-	$41.54^{41.64}_{41.42}$		
NGC 4395	*Chandra*	5302	$39.37^{39.37}_{39.37}$	$39.96^{39.96}_{39.96}$	$39.50^{39.54}_{39.46}$	$39.94^{39.96}_{39.92}$
	Chandra	5301	$39.65^{39.65}_{39.65}$	$39.93^{39.93}_{39.93}$	$39.50^{39.53}_{39.47}$	$39.94^{39.96}_{39.92}$
	XMM–Newton	0112521901	$39.76^{39.78}_{39.73}$	$40.33^{40.34}_{40.32}$	$39.75^{39.76}_{39.73}$	$40.34^{40.35}_{40.33}$
	XMM–Newton	0744010101	$39.69^{39.70}_{39.67}$	$40.23^{40.23}_{40.22}$	$39.63^{39.64}_{39.62}$	$40.22^{40.23}_{40.21}$
	XMM–Newton	0744010201	$39.65^{39.67}_{39.63}$	$40.28^{40.29}_{40.27}$	$39.68^{39.70}_{39.67}$	$40.28^{40.29}_{40.27}$
	XMM–Newton	0112521901			$39.94^{39.96}_{39.91}$	$40.38^{40.42}_{40.34}$
	Chandra	5301			$39.53^{39.56}_{39.51}$	$39.93^{39.97}_{39.89}$
NGC 4565	*XMM–Newton*	0112550301	$39.55^{39.57}_{39.53}$	$39.76^{40.72}_{39.87}$	$39.53^{39.55}_{39.51}$	$39.70^{39.74}_{39.67}$
	Chandra (2″)	3950	$39.47^{39.49}_{39.45}$	$40.21^{40.72}_{40.02}$	$39.48^{39.50}_{39.46}$	$39.60^{39.64}_{39.56}$
	Chandra (20″)	3950	$39.52^{39.54}_{39.50}$	$39.66^{40.39}_{39.12}$		
M RK 883	*XMM–Newton*	0302260101	$42.42^{42.43}_{42.41}$	$42.73^{42.75}_{42.71}$	$42.42^{42.43}_{42.41}$	$42.72^{42.73}_{42.70}$
	XMM–Newton	0302260701	$42.42^{42.43}_{42.41}$	$42.71^{42.73}_{42.69}$	$42.42^{42.43}_{42.41}$	$42.71^{42.72}_{42.70}$
	XMM–Newton	0302261001	$42.56^{42.57}_{42.55}$	$42.80^{42.81}_{42.78}$	$42.52^{42.53}_{42.51}$	$42.81^{42.83}_{42.80}$
	XMM–Newton	0652550201	$42.27^{42.28}_{42.27}$	$42.59^{42.60}_{42.58}$	$42.28^{42.29}_{42.28}$	$42.58^{42.59}_{42.57}$
IR S 20051-1117	*XMM–Newton*	0044350201	$42.45^{42.46}_{42.44}$	$42.62^{42.65}_{42.60}$	$42.46^{42.47}_{42.45}$	$42.60^{42.62}_{42.58}$
	XMM–Newton	0044350501	$42.30^{42.31}_{42.29}$	$42.46^{42.48}_{42.44}$	$42.31^{42.32}_{42.30}$	$42.45^{42.47}_{42.44}$

N tes. (Cols. 4 and 5) soft and hard intrinsic luminosities for individual fits; (Cols. 6 and 7) soft and hard intrinsic luminosities for simultaneous fitting. Blanks mean observations that are not used for the simultaneous fittings.

Table .4: Statistics of the light curves.

Name	ObsID	Energy	$\chi^2/d.o.f$	Prob.(%)	$^2_{NXS}$	$< ^2_{NXS} >$
(1)	(2)	(3)	(4)	(5)	(6)	(7)
ESO 113-G10	0301890101	0.5–10 (1)	1194.3/32	100	$0.0186^{+}_{-}0.0003$	$0.01856^{+}_{-}0.00005$
		0.5–10 (2)	1703.8/39	100	$0.0185^{+}_{-}0.0003$	
		0.5–2 (1)	1014.3/32	100	$0.0185^{+}_{-}0.0003$	$0.0183^{+}_{-}0.0002$
		0.5–2 (2)	1419.7/39	100	$0.0181^{+}_{-}0.0003$	
		2–10 (1)	222.5/32	100	$0.019^{+}_{-}0.001$	$0.020^{+}_{-}0.001$
		2–10 (2)	333.9/39	100	$0.021^{+}_{-}0.001$	
NGC 526	0150940101	0.5–10	228.9/28	100	$0.0025^{+}_{-}0.0001$	
		0.5–2	130.6/28	100	$0.0038^{+}_{-}0.0003$	
		2–10	128.4/28	100	$0.0018^{+}_{-}0.0001$	
	0721730301	0.5–10	109.3/33	100	$0.00068^{+}_{-}0.00007$	
		0.5–2	66.1/33	100	$0.0009^{+}_{-}0.0002$	
		2–10	81.3/33	100	$0.0006^{+}_{-}0.0001$	
	0721730401	0.5–10	376.2/38	100	$0.00241^{+}_{-}0.00006$	
		0.5–2	75.4/38	100	$0.0008^{+}_{-}0.0002$	

Table .4: (Cont.)

Name	ObsID	Energy	$\chi^2/d.o.f$	Prob.(%)	σ^2_{NXS}	$< \sigma^2_{NXS} >$
(1)	(2)	(3)	(4)	(5)	(6)	(7)
		2–10	341.1/38	100	$0.00321^{+}0.00009$	
NGC 1365	0205590301	0.5–10	1012.7/37	100	$0.0206^{+}0.0004$	
		0.5–2	33.3/37	36	<0.0014	
		2–10	1464.2/37	100	$0.0412^{+}0.0009$	
	0505140201	0.5–10	41.3/27	99	$0.0014^{+}0.0007$	
		0.5–2	37.2/27	99	$0.0013^{+}0.0009$	
		2–10	18.8/27	12	$0.004^{+}0.004$	
	0505140401	0.5–10 (1)	55.3/25	100	$0.0030^{+}0.0007$	$0.0020^{+}0.0013$
		0.5–10 (2)	18.7/36	1	<0.0014	
		0.5–2 (1)	25.6/25	57	$0.0002^{+}0.0009$	$0.0001^{+}0.0001$
		0.5–2 (2)	31.6/36	32	<0.0017	
		2–10 (1)	67.6/25	100	$0.018^{+}0.003$	$0.0012^{+}0.0008$
		2–10 (2)	32.2/36	35	<0.0068	
	0505140501	0.5–10	53.3/30	100	$0.0020^{+}0.0007$	
		0.5–2	45.0/30	99	$0.0016^{+}0.0008$	
		2–10	24.1/30	33	<0.0077	
	0692840201	0.5–10 (1)	634.3/40	100	$0.0183^{+}0.0005$	$0.0107^{+}0.0035$
		0.5–10 (2)	384.1/40	100	$0.0105^{+}0.0003$	
		0.5–10 (3)	228.6/38	100	0.0063^{+} 0.0003	
		0.5–2 (1)	52.6/40	99	$0.0010^{+}0.0007$	$0.0006^{+}0.0003$
		0.5–2 (2)	47.4/40	80	$0.0006^{+}0.0007$	
		0.5–2 (3)	60.0/38	100	$0.0019^{+}0.0007$	
		2–10 (1)	1291.7/40	100	$0.058^{+}0.002$	$0.028^{+}0.009$
		2–10 (2)	630.9/40	100	$0.0281^{+}0.0009$	
		2–10 (3)	352.6/38	100	$0.0178^{+}0.0007$	
	0692840301	0.5–10 (1)	3511.7/38	100	$0.0426^{+}0.0006$	$0.0417^{+}0.0008$
		0.5–10 (2)	3763.3/40	100	$0.0409^{+}0.0005$	
		0.5–2 (1)	659.6/38	100	$0.0257^{+}0.0007$	$0.0262^{+}0.0005$
		0.5–2 (2)	791.5/40	100	$0.0267^{+}0.0007$	
		2–10 (1)	3229.5/38	100	$0.0538^{+}0.0009$	$0.052^{+}0.002$
		2–10 (2)	3175.1/40	100	$0.0495^{+}0.0008$	
	0692840401	0.5–10 (1)	5994.8/37	100	$0.090^{+}0.001$	$0.06^{+}0.02$
		0.5–10 (2)	5409.8/36	100	$0.0453^{+}0.0005$	
		0.5–2 (1)	1458.4/37	100	$0.067^{+}0.002$	$0.058^{+}0.006$
		0.5–2 (2)	2447.0/36	100	$0.054^{+}0.001$	
		2–10 (1)	4977.2/37	100	$0.106^{+}0.002$	$0.06^{+}0.02$
		2–10 (2)	3164.0/36	100	$0.0430^{+}0.0006$	
	0692840501	0.5–10 (1)	6872.7/36	100	$0.145^{+}0.002$	$0.03^{+}0.02$
		0.5–10 (2)	1125.4/38	100	$0.0276^{+}0.0006$	
		0.5–10 (3)	504.2/39	100	$0.0115^{+}0.0003$	
		0.5–2 (1)	559.1/36	100	$0.054^{+}0.002$	$0.01^{+}0.02$
		0.5–2 (2)	21.9/38	2	<0.0014	
		0.5–2 (3)	24.9/39	5	<0.0014	
		2–10 (1)	7598.8/36	100	$0.192^{+}0.004$	$0.05^{+}0.03$
		2–10 (2)	1585.9/38	100	$0.059^{+}0.001$	
		2–10 (3)	753.4/39	100	$0.0271^{+}0.0007$	
NGC 2617	0701981601	0.5–10	128.7/31	100	$0.00046^{+}0.00004$	
		0.5–2	138.3/31	100	$0.00065^{+}0.00005$	
		2–10	27.1/31	73	<0.0003	
NGC 2992	0654910501	0.5–10	41.2/40	58	$0.00003^{+}0.00014$	
		0.5–2	44.9/40	73	$0.0002^{+}0.0003$	
		2–10	27.6/40	7	$0.00031^{+}0.0002$	

Table .4: (Cont.)

Name	ObsID	Energy	$\chi^2/d.o.f$	Prob.(%)	$^2_{NXS}$	$< ^2_{NXS} >$
(1)	(2)	(3)	(4)	(5)	(6)	(7)
	0654910601	0.5–10	29.4/22	87	$0.0006^{+}_{-}0.0005$	
		0.5–2	16.2/22	19	<0.0024	
		2–10	28.2/22	83	$0.0011^{+}_{-}0.0009$	
	0654910701	0.5–10	70.4/36	100	$0.0015^{+}_{-}0.0004$	
		0.5–2	36.2/36	54	$0.00002^{+}_{-}0.00078$	
		2–10	61.8/36	100	$0.0021^{+}_{-}0.0007$	
	0654910901	0.5–10	24.9/29	32	<0.0017	
		0.5–2	25.7/29	36	<0.0033	
		2–10	25.6/29	35	<0.0035	
	0654911001	0.5–10	61.1/32	100	$0.0014^{+}_{-}0.0004$	
		0.5–2	45.2/32	99	$0.0015^{+}_{-}0.0008$	
		2–10	50.9/32	99	$0.0017^{+}_{-}0.0007$	
POX 52	0302420101	0.5–10 (1)	59.5/23	100	$0.09^{+}_{-}0.02$	$0.05^{+}_{-}0.03$
		0.5–10 (2)	50.9/33	99	$0.03^{+}_{-}0.01$	
		0.5–2 (1)	60.6/23	100	$0.20^{+}_{-}0.06$	$0.08^{+}_{-}0.08$
		0.5–2 (2)	38.2/33	76	$0.02^{+}_{-}0.03$	
		2–10 (1)	34.6/23	95	$0.05^{+}_{-}0.03$	$0.03^{+}_{-}0.01$
		2–10 (2)	45.8/33	99	$0.02^{+}_{-}0.02$	
NGC 4395	0744010101	0.5–10	782.1/40	100	$0.069^{+}_{-}0.003$	
		0.5–2	83.7/40	100	$0.045^{+}_{-}0.01$	
		2–10	815.1/40	100	$0.077^{+}_{-}0.003$	
NGC 4565	3950	0.5–10	30.1/40	13	<0.0161	
		0.5–2	43.5/40	68	$0.004^{+}_{-}0.001$	
		2–10	40.0/40	53	<0.0548	

N tes. (Col. 1) name, (Col. 2) obsID, (Col. 3) energy band in keV, (Cols. 4 and 5) $\chi^2/d.o.f$ and the probability of being variable in the 0.5-10.0 keV energy band of the total light curve, (Col. 6) normalized excess variance, $^2_{NXS}$, and (Col. 8) the mean value of the normalized excess variance, $< ^2_{NXS} >$, for each light curve and energy band.

Table .5: Classification of the sample objects on the basis of the nuclear X-ray obscuration (and its variability).

Name	ObsID	Γ	EW (keV)	$F_x/F_{[OIII]}$	Ref.[1] $[OIII]$	CT?	Classification
(1)	(2)	(3)	(4)	(5)	(6)	(7)	(8)
ESO540-G01	0044350101	$1.44^{2.32}_{1.07}$	<0.48	-	-	✗	Compton-thin
ESO195-IG21	0554500201	$1.29^{1.52}_{1.06}$	$0.11^{0.15}_{0.08}$	-	-	✗	Compton-thin
	13898	$2.06^{2.57}_{0.87}$	$0.51^{0.78}_{0.23}$	-		✗	
ESO113-G10	0103861601	$1.62^{1.89}_{1.38}$	<0.18	-	-	✗	Compton-thin
	0301890101	$1.80^{1.87}_{1.75}$	<0.04	-		✗	
NGC526	0109130201	$1.30^{1.41}_{1.24}$	$0.08^{0.11}_{0.05}$	75.4	1	✗	Compton-thin
	0150940101	$1.55^{1.61}_{1.48}$	$0.06^{0.07}_{0.05}$	99.4		✗	
	0721730301	$1.48^{1.53}_{1.43}$	$0.07^{0.07}_{0.06}$	114.2		✗	
	0721730401	$1.58^{1.63}_{1.52}$	$0.06^{0.07}_{0.05}$	137.3		✗	
	342	<0.53	<0.23	19.4		✗	
M RK609	0103861001	$1.59^{1.86}_{1.22}$	<0.16	31.1	2	✗	Compton-thin
	0402110201	$1.25^{1.45}_{1.08}$	$0.11^{0.19}_{0.03}$	32.5		✗	
NGC1365	0151370101	$1.18^{1.46}_{0.91}$	$0.20^{0.25}_{0.16}$	13.2	1	✗	Changing-look
	0151370201	<1.36	<0.31	2.2		✗	
	0151370701	$2.44^{2.77}_{2.20}$	$0.14^{0.18}_{0.09}$	17.0		✗	
	0205590301	$2.88^{2.94}_{2.84}$	$0.11^{0.12}_{0.10}$	19.1		✗	
	0205590401	$2.18^{2.37}_{2.08}$	$0.17^{0.19}_{0.15}$	14.5		✗	

Table .5: (Cont.)

Name	ObsID	Γ	EW (keV)	$F_x/F_{[OIII]}$	Ref.[1] [$OIII$]	CT?	Classification
(1)	(2)	(3)	(4)	(5)	(6)	(7)	(8)
	0505140201	<0.39	$0.46^{0.52}_{0.41}$	3.9			
	0505140401	<0.09	$0.42^{0.54}_{0.39}$	7.1			
	0505140501	<0.17	$0.43^{0.58}_{0.38}$	5.6			
	0692840201	$2.08^{2.12}_{1.99}$	$0.12^{0.13}_{0.11}$	17.4		✗	
	0692840301	$2.40^{2.44}_{2.38}$	$0.09^{0.10}_{0.08}$	18.2		✗	
	0692840401	$2.32^{2.38}_{2.31}$	$0.08^{0.09}_{0.07}$	18.2		✗	
	0692840501	$2.20^{2.22}_{2.13}$	$0.09^{0.10}_{0.08}$	17.8		✗	
	6869	$1.34^{2.08}_{0.96}$	$0.13^{0.19}_{0.07}$	13.2		✗	
NGC2617	0701981601	$1.60^{1.63}_{1.58}$	$0.06^{0.07}_{0.05}$	-	-	✗	Compton-thin
	0701981901	$1.70^{1.74}_{1.67}$	$0.05^{0.06}_{0.03}$	-		✗	
M RK1218	0302260201	$1.34^{1.75}_{1.13}$	<0.09	18.1	2	✗	Compton-thin
	0302260401	$1.670^{2.99}_{0.74}$	<0.20	8.1		✗	
NGC2992	0654910501	$1.54^{1.63}_{1.46}$	$0.16^{0.18}_{0.14}$	2.2	1	✗	Changing-look
	0654910601	$1.31^{1.45}_{1.20}$	$0.33^{0.36}_{0.29}$	0.9		✗	
	0654910701	$1.26^{1.36}_{1.22}$	$0.32^{0.34}_{0.29}$	0.9		✗	
	0654910901	$1.23^{1.42}_{1.05}$	$0.50^{0.55}_{0.45}$	0.5			
	0654911001	$1.30^{1.42}_{1.22}$	$0.25^{0.28}_{0.22}$	1.0		✗	
	0701780101	$1.39^{1.54}_{1.33}$	$0.17^{0.21}_{0.14}$	2.8		✗	
POX52	0302420101	$1.48^{1.88}_{1.14}$	<0.11	8.2	3	✗	Compton-thin
	5736	$1.79^{3.23}_{1.44}$	<0.45	12.5		✗	
NGC4138	0112551201	$1.23^{1.49}_{0.98}$	$0.08^{0.13}_{0.04}$	478.6	4	✗	Compton-thin
	3994	$1.29^{1.94}_{0.18}$	$0.17^{0.30}_{0.04}$	478.6		✗	
NGC4395	0112521901	$1.28^{1.53}_{1.05}$	$0.11^{0.16}_{0.07}$	64.8	4	✗	Compton-thin
	5301	$1.24^{1.65}_{0.80}$	<0.11	27.7		✗	
	5302	$1.26^{1.67}_{0.64}$	<0.10	25.8		✗	
NGC4565	0112550301	$1.55^{2.49}_{1.08}$	<0.71	5.6	5	✗	Compton-thin
	3950	$2.73^{2.95}_{1.51}$	$0.03^{0.05}_{0.01}$	15.4		✗	
M RK883	0302260101	$1.22^{1.49}_{1.05}$	<0.17	27.5	2	✗	Compton-thin
	0302260701	$1.44^{1.65}_{1.26}$	$0.12^{0.21}_{0.02}$	26.2		✗	
	0302261001	$1.58^{2.13}_{1.34}$	$0.10^{0.19}_{0.02}$	32.3		✗	
	0652550201	$1.43^{1.73}_{1.33}$	$0.18^{0.24}_{0.11}$	19.9		✗	
IR S20051-1117	0044350201	$1.68^{2.41}_{1.36}$	$0.21^{0.35}_{0.06}$	13.8		✗	Compton-thin
	0044350501	$1.70^{2.25}_{1.48}$	<0.16	9.5	5	✗	

N tes. (Col. 1) name, (Col. 2) obsID, (Cols. 3 and 4) index of the power law and the equivalent width of the FeKα line from the spectral fit (PL model) in the 3–10 keV energy band, (Col. 5) ratio between the individual hard X-ray luminosity (from Table .3) and the extinction-corrected [O III] fluxes, (Col. 6) references for the measure of $F_{[OIII]}$, (Col. 7) classification from the individual observation, (Col. 8) classification of the object, and (Col. 9) slope of the power law at hard energies for Compton-thick candidates from the simultaneous analysis (see Sect. 4.5). [1]References: (1) Bassani et al. (1999); (2) Dahari & De Robertis (1988); (3) Whittle (1992); (4) Panessa et al. (2006); and (5) Panessa & Bassani (2002).

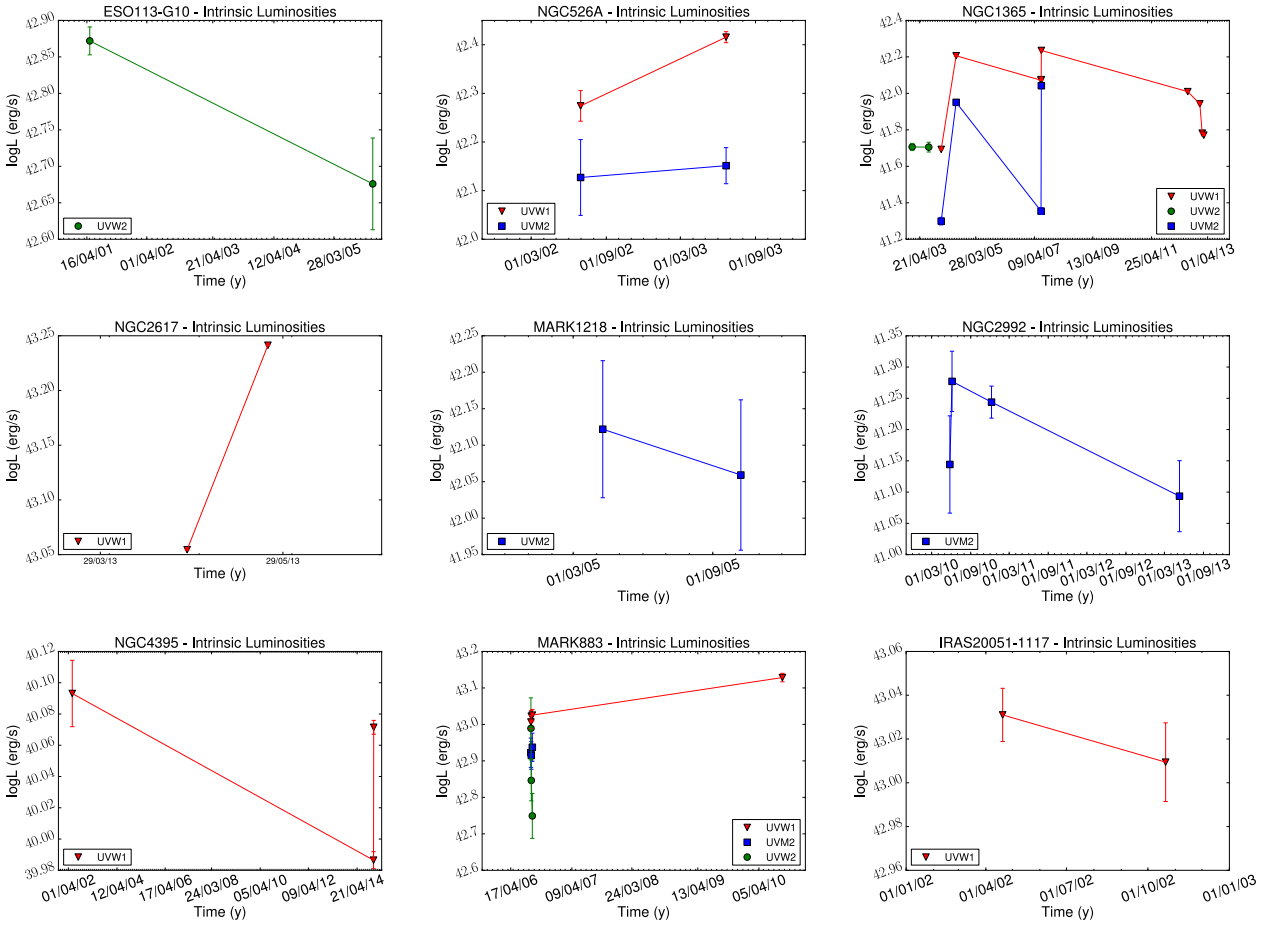

Fig. .1: UV luminosities obtained from the data with the OM camera onboard *XMM*–Newton, when available. Different filters have been used; UVW1 (red triangles), UVW2 (green circles), and UVM2 (blue squares).

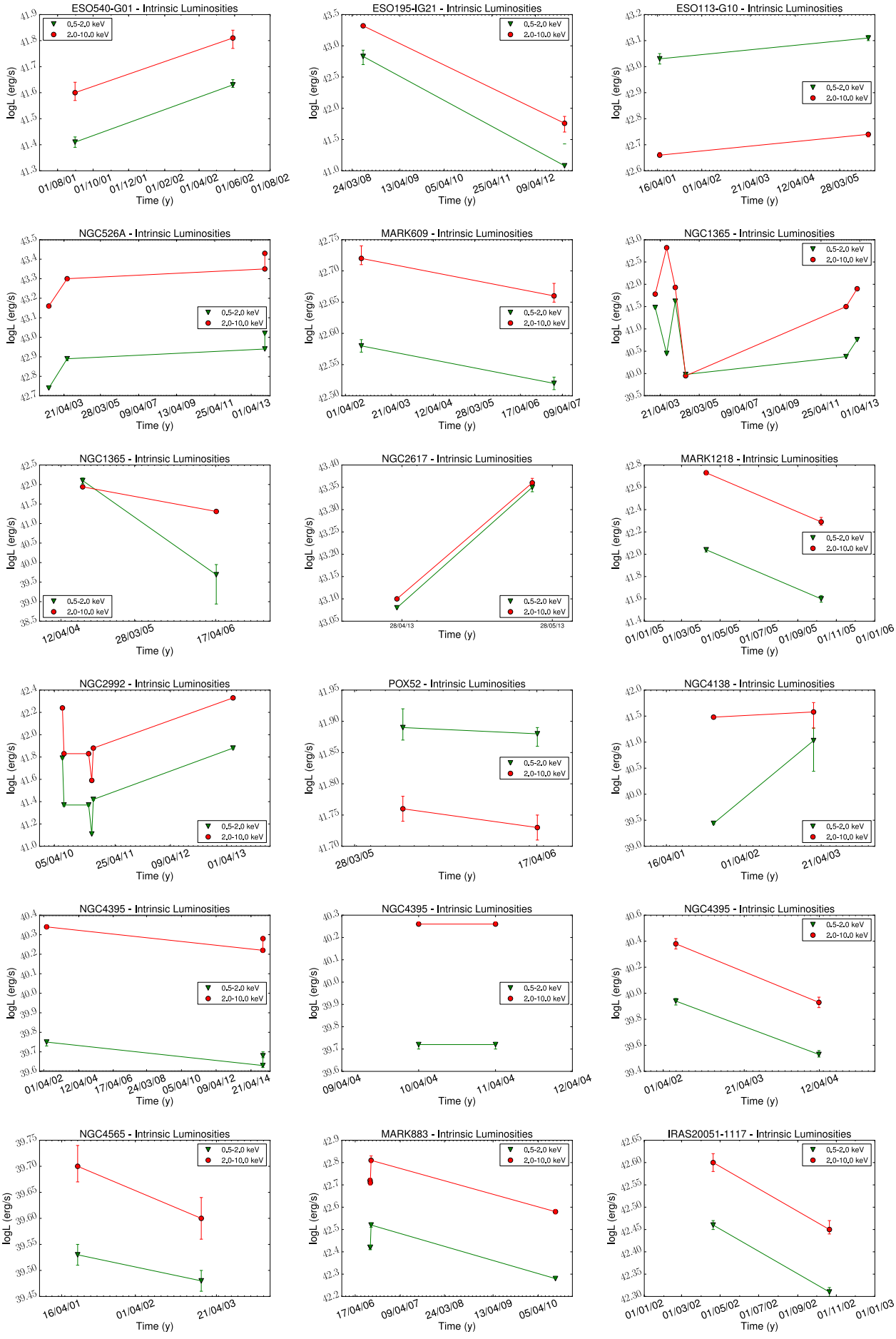

Fig. 2. X-ray intrinsic luminosities calculated for the soft (0.5–2.0 keV, green triangles) and hard (2.0–10.0 keV, red circles) energies in the simultaneous fits, only for the variable objects.

ppendix B: Notes and comparisons with previous results for individual objects

In this appendix we discuss the general characteristics of the galaxies in our sample at different wavelengths, as well as comparisons with previous variability studies. We recall that long-term UV variability and short-term X-ray variations were studied only for some sources (ten and seven sources, see Tables 1 and .4, respectively), so comparisons are only made in those cases. For the remaining objects, results from other authors are mentioned, when available.

ppendix B.1: ESO 540-G01

NGC 540-G01 is the brightest member of the Hickson compact group 4 (Hickson et al. 1989). It was classified as a Seyfert 1.8 using optical data (Coziol et al. 1993), although also as a composite galaxy (Moran et al. 1996). radio counterpart was detected with *VL* data at 1.4 GHz (Condon et al. 1998). It is another source classified as a type 1 GN showing no X-ray absorption (Panessa et al. 2005).

This galaxy was observed once by *Chandra* in 2001 and once by *XMM–Newton* in 2002. Georgantopoulos et al. (2003) studied the *Chandra* data. They found long-term X-ray flux variations when comparing with previous *ROS T* data by a factor of 25 in ten years. When comparing *Chandra* and *XMM–Newton* data, the annular region contributed with 21% in *Chandra* data, and the best representation is obtained with SMF1 showing variations in $Norm_2$ (74%) in one year period. This implies flux variability of 40% (38%) in the soft (hard) energy band.

Georgantopoulos et al. (2003) studied the *Chandra* light curve and did not find short-term variability.

ppendix B.2: ESO 195-IG21

ESO 195-IG21 was classified as a Seyfert 1.8 using optical data, after its discovery using *Swift* data (Baumgartner et al. 2008). We did not find data at radio frequencies for this source in the literature.

This galaxy was observed once by *XMM–Newton* in 2008 and once by *Chandra* in 2012. Variability studies of this source were not found in the literature. In this case, the annular region contributed with 10% to the *Chandra* data. When comparing the data, SMF2 results in the best fit with $Norm_1$ (91%) and $Norm_2$ (98%) varying in a four years period. This results in flux variability of 98% (97%) in the soft (hard) energy band.

ppendix B.3: ESO 113-G10

The nucleus was classified as a Seyfert 1.8 in the optical by Pietsch et al. (1998), who also reported X-ray variations of a factor of three between two *ROS T* observations obtained within six months.

ESO 113-G10 was observed twice with *XMM–Newton* in 2001 and 2005. Long-term X-ray variability studies of these source were not found in the literature. We find that SMF1 with variations in $Norm_1$ (40%) represents the data best in a four years period. This implies flux variations of 17% in both the soft and hard energy bands.

Porquet et al. (2007) found short-term variations in the soft and hard light curve from 2005 in timescales lower than 500 s. These results agree well with those obtained by González-Martín & Vaughan (2012) and ours, because the analysis of the same light curve resulted in short-term variations of the total, soft, and hard energy bands. Later, Cackett et al. (2013) used the same observation to report a hard and a soft lag at low and high frequencies, respectively, between the 1.5–4.5 keV and 0.3–0.9 keV energy bands.

t UV frequencies, we detected variations in the UVW2 (8) filter from the OM.

ppendix B.4: NGC 526

NGC 526 is the west galaxy in the strongly interacting pair of galaxies in NGC 526 (Mulchaey et al. 1996). It was optically classified as a Seyfert 1.9 (Griffiths et al. 1979; Winkler 1992). radio counterpart was detected with *VL* data at 3.6 and 20 cm (Nagar et al. 1999).

X-ray flux and spectral variability was detected in this source as observed by *HE O 1*, *Einstein*, *EXOS T* and *GING* in timescales of years (Mushotzky 1982; Turner & Pounds 1989; Polletta et al. 1996).

It has been observed with *Chandra* five times between 1999 and 2003, and four times with *XMM–Newton* between 2002 and 2013. Long-term variability analyses using these data are not reported in the current literature. SMF1 is the best representation of the *XMM–Newton* data presented in this work, with variations in $Norm_2$ (48%). This implies a flux variation of 48% (46%) in the soft (hard) energy band in 11 years period. When comparing with *Chandra* data (the annular region contributed with 45% in *Chandra* data) out method cannot differentiate if variations in N_{H2} ($\chi^2_r = 1.03$) or variations in $Norm_2$ ($\chi^2_r = 1.08$) are preferred in the two years period, both results being a good option. For this reason we do not report this analysis and we take into account the results from the *XMM–Newton* data.

González-Martín & Vaughan (2012) studied the *XMM–Newton* observation from 2003 and found that it showed short-term variations in the three analysed energy bands. We studied three *XMM–Newton* observations (except the one from 2002) and detected short-term variations in all of them and the three energy bands, in good agreement with González-Martín & Vaughan (2012). In short timescales, Turner et al. (1997) also detected rapid variations using *SC* data. Using *RXTE* data between 2001 and 2003, Zhang (2011) estimated $^{2}_{NXS} = 8.16^{+}_{-}1.81 \quad 10^{-2}$.

In the 14–195 keV energy band, Soldi et al. (2014) estimated a variability amplitude of $35^{+}_{-}6\%$ using data from the *Swift*/B T 58-month survey.

UV data from the OM are available in two filters. Variations are detected in the UVW1 (11) but not in the UVM2 (1) filter.

ppendix B.5: M RK 609

This galaxy was classified as a Seyfert 1.8 by Osterbrock (1981), although it was later classified as a type 2 and 1.5, suggesting that this might be a changing-look candidate (Trippe et al. 2010, and references therein). It has also been proposed to be a "true" Seyfert 2, i.e., an GN that lack circumnuclear obscuration (LaMassa et al. 2011, 2014). radio counterpart was detected with *VL* data at 6 cm (Ulvestad & Wilson 1984).

The source was observed twice with *XMM–Newton* in 2002 and 2007. Variability studies using these data were not found in the literature. We find that SMF1 represents best the data, requiring changes in $Norm_1$ (22%) within five years. This implies flux variations of 13% in both the soft and hard energy bands.

ppendix B.6: NGC 1365

NGC 1365 is a barred spiral galaxy located in the Fornax I cluster. It was classified as a Seyfert 1.8 at optical wavelenghts (Maiolino & Rieke 1995). This is the prototypical example of a changing-look source, having changed from reflection-dominated to transmission dominated states in different occasions, in good agreement with the results presented here (e.g., Risaliti et al. 2009). radio counterpart was observed with *VL* data (Jorsater & van Moorsel 1995).

It was observed 13 times with *XMM–Newton* between 2003 and 2013, and seven times with *Chandra* between 2002 and 2006.

Risaliti et al. (2005b) studied a *Chandra* observation from 2002 and three *XMM–Newton* observations from 2003. They reported variations from Compton-thin to Compton-thick in timescales of six weeks, which were attributed to changes in the absorber, whereas the soft thermal emission and the reflection component remained constant. The same authors also discovered four absorption lines between 6.7 and 8.3 keV (identified them as Fe XXV and Fe XXVI Kα and Kβ lines) related to absorption by a highly ionized gas (Risaliti et al. 2005a), and detected an X-ray eclipse from clouds in the BLR from the *XMM–Newton* observation from January 2004 (Risaliti et al. 2009). Guainazzi et al. (2009) analyzed the *RGS* data and suggested that the relative weakness of the photoionisation might be related to the same material responsible for the X-ray abosrbing column density variations.

Simultaneous *XMM–Newton* and *Suzaku* data from 2012 and 2013 were studied by different authors. Risaliti et al. (2013) and Walton et al. (2014) found continuum variations related to absorption from reflection, Parker et al. (2014) reported variability in the absorber and intrinsic to the source using a principal component analysis (PC), Braito et al. (2014) found absorption variations in timescales of about 100 ksec in the 0.3–1.8 keV energy band related to a low ionization zone of a disk wind, and Rivers et al. (2015) reported that changes in this source are mainly due to absorption. Our method does not allow to perform the spectral fit to all the spectra simultaneously ($\chi^2_r > 2.5$). Instead, we removed the spectra in the Compton-thick state (Risaliti et al. 2005a) and those in a 'relativistic' state (Risaliti et al. 2013). Therefore we used six *XMM–Newton* observations. The best fit resulted from the use of SMF3 with N_{H2} (68%), $Norm_2$ (33%), and $Norm_1$ (35%) varying. These changes imply a change in flux of 81% (24%) in the soft (hard) energy band in a 10 years period. When comparing *Chandra* and *XMM–Newton* data, SMF2 was required with variatons in N_{H2} (37%) and $Norm_2$ (30%) in a two years period. The annular region contributed with 53% in *Chandra* data.

Connolly et al. (2014) studied 190 observations obtained with *Swift* between 2006 and 2013. They reported variations in the normalizations of the soft and hard energy bands plus changes in the absorbing material, and interpreted these variations in terms of an GN wind scenario.

Brenneman et al. (2013) studied three *Suzaku* observations of NGC 1365 obtained between 2008 and 2010. They reported variations both at short- and long-term, mainly due to absorption and continuum variations.

González-Martín & Vaughan (2012) studied three *XMM–Newton* observations between 2004 and 2007. They found short-term variations in the hard and total energy bands of the three observations, whereas the soft band did not show variations. We analyzed two of these light curves and found a good agreement. In total, we were able to study short-term variations in eight observations. We found that variations in the hard and total energy bands are very common in all the observations, but variability in the soft band is observed only in observations from 2012 and 2013. The light curve presented by Connolly et al. (2014) using *Swift* data also showed short-term variations. They attributed these variations to clouds passing throught the line of sight of the observer. Using the simultaneous *XMM–Newton* and *NuSTAR* data, Kara et al. (2015) found a Fe K lag, plus another lag at low frequencies, probably due to absorption variations.

Data at UV frequencies were available from the OM in the three UV filters. Strong variations were detected with the UVW1 (62) and UVM2 (76) filters. Variations were not detected with the UVW2 (1) filter, but data were available only in two epochs separated by about seven months.

ppendix B.7: NGC 2617

NGC 2617 is a spiral galaxy. It was optically classified as a Seyfert 1.8 (Moran et al. 1996), although it was classified as a type 1 in 2014, when it was also classified as a changing-look GN (Shappee et al. 2014). radio counterpart was detected with the *VL* (Condon et al. 1998).

This galaxy was observed twice with *XMM–Newton* in 2013. These data were studied by Giustini et al. (2016), who reported changes in flux, spectral shape ($\Gamma \sim 0.1$) and in N_H within the month timescale. Our analysis of the same *XMM–Newton* data showed that SMF2 is the best representation of the data set, with changes in $Norm_1$ (59%) and N_{H2} (30%) within a one month period. This implies flux variations of 46% (45%) in the soft (hard) energy band. follow up of this source of $\sim$ 70 days using X-ray, UV, optical and NIR data was conducted by Shappee et al. (2014) after a transient source alert on 2013 pril. They observed an increasing X-ray flux of about one order of magnitude followed by an increase in its optical/UV continuum flux. By cross-correlating the light curves, they found that the UV (2–3 days) and the NIR (6–9 days) lagged behing the X-rays, and explained this variability behaviour due to X-ray radiation driven by the disk.

Giustini et al. (2016) analyzed the *XMM–Newton* light curves and reported modest variations in the 0.3-10 keV energy band. They also reported hints of a soft band delay on time scales larger than 5 ks between the soft and the hard energy bands. From the analysis of one of the *XMM–Newton* light curves, we found short-term variations in the soft and total energy bands.

In the UV, we detected variations in the UVW1 (30) filter with data from the OM.

ppendix B.8: M RK 1218

M RK 1218 (also named NGC 2622) was optically classified as a Seyfert 1.8 by Osterbrock & Dahari (1983), but it changed to a Seyfert 1 spectrum a few years later (Smith et al. 2004) and has also been classified as a type 1.9 (Trippe et al. 2010). radio counterpart was detected with *VL* data at 6 and 20 cm (Ulvestad 1986).

This source was observed with *XMM–Newton* twice in 2005. Variability studies of this source were not found in the literature. Singh et al. (2011) performed a spectral fit of the obsID. 0302260201 using an absorbed power law with warm absorption, and obtained an X-ray luminosity of logL(2–10 keV) = 42.68, in very good agreement with our estimation. We found that the best representation of the data is SMF1 with changes in

Norm (63%). This implies flux changes of 64% in both the soft and hard enery bands.

In the UV, variations were not detected with the UVM2 (1) filter from the OM.

ppendix B.9: NGC 2992

NGC 2992 is interacting with NGC 2993, which is located at 2.9′. It was classified as a Seyfert 1.9 by Ward et al. (1980) using optical data. radio counterpart was detected with *VL* data at 5 GHz (Condon et al. 1982). In good agreement with our results, it is also a changing-look candidate (Gilli et al. 2000; Trippe et al. 2008).

Historically, X-ray flux variability by a factor of 20 was found in this source between different satellites (Shu et al. 2010, and references therein).

It was observed four times with *Chandra* between 2003 and 2010, and ten times with *XMM–Newton* between 2003 and 2013. Shu et al. (2010) studied the *XMM–Newton* data from 2003 and reported flux variability when comparing with *Suzaku* data from 2005. They attributed the changes to intrinsic variability of the source. Parker et al. (2015) used the nine *XMM–Newton* observations between 2003 and 2010 to study variability through principal component analysis. They reported variations in two components, one corresponding to intrinsic source variability, and a more ambigous one, corresponding either to changes in the power law, the column density, or the soft excess. From the analysis of the *XMM–Newton* data, the best representation is obtained with SMF2 varying N_{H2} (5%) and $Norm_2$ (21%) in a three years period. This results in a flux variation of 19% in the soft and hard energy bands.

The covering of this source with *RXTE* during one year (24 observations) was presented by Murphy et al. (2007), who reported flux variations by a factor of 10 in timescales of days to weeks. They related these variations with changes in the inner accretion disk.

González-Martín & Vaughan (2012) studied the nine *XMM–Newton* observations between 2003 and 2010 and reported short-term variations in three energy bands but not in all the observations, being more frequent in the total and hard energy bands than in the soft band. We analysed five *XMM–Newton* observations and detected variations in the total and hard energy bands in a few observations, but none in the soft band.

t higher energies, a combined study with *INTEGR L*, *Swift*, and *BeppoS X* data published by Beckmann et al. (2007) showed that variations in the normalization of the power law were needed when using an absorbed broken power law model to fit the data simultaneously. They found a constant Γ and flux variations by a factor of 11 in timescales of months/years.

Variations in the near infrared were reported by Glass (1997) due to an outburst between March 1988 and pril 1992 observed with the 1.9m telescope at Sutherland.

t UV frequencies, variations in the UVM2 filter of 6 were detected with the OM.

ppendix B.10: POX 52

POX 52 is a dwarf elliptical galaxy. It was optically classified as a Seyfert 1.8 by Barth et al. (2004). radio counterpart was observed with *VL* data at 5 GHz (Thornton et al. 2008).

This source was observed once by *XMM–Newton* in 2005 and once by *Chandra* in 2006. Thornton et al. (2008) studied these observations. They found variations in the column density due to partial covering during this period. This result agrees well with our analysis, where variations in N_{H2} (44%) and N_{H1} (it passes from a value of ~ 8 $10^{22} cm^{-2}$ to the Galactic value) are needed to explain the observed variations in the same dataset. We note however that our values of N_{H2} are larger than theirs, most probably due to the different models used (we used two absorbers instead of one). The annular region contributed with 4% to the *Chandra* data.

González-Martín et al. (2011) studied a sample of ultraluminous X-ray sources (ULX) using *XMM–Newton* data and included this source because the GN has a low black hole mass. They reported short-term variations through the estimation of $^{2}_{NXS}$ in the 2–10 keV energy band. Dewangan et al. (2008) also estimated the $^{2}_{NXS}$ and found it to be compatible with short-term variations for the same *XMM–Newton* observation. The *Chandra* and *XMM–Newton* light curves were analysed by Thornton et al. (2008), who found variations in timescales of 500 s and 10^4 s, respectively, in the 0.5–10 keV energy band. These results agree well with our analysis of the *XMM–Newton* light curve, where we also detected these variations.

t UV frequencies, Thornton et al. (2008) studied the OM data and also *G LEX* data, but variations were not detected.

ppendix B.11: NGC 4138

NGC 4138 is a spiral galaxy that was classified as a Seyfert 1.9 by Ho et al. (1997). radio counterpart was detected using *VL* data at 2cm (Nagar et al. 2002).

This galaxy was observed once with *XMM–Newton* in 2001 and once with *Chandra* in 2003. Variability studies of this source were not found in the literature. The *XMM–Newton* spectrum is best fitted with the ME2PL model, but the *Chandra* spectrum did not have enough counts below ∼2 KeV, and thus the PL model was used to fit both spectra individually and also for the simultaneous fit in the 2–10 keV energy band. The annular region contributed with 83% in *Chandra* data. SMF1 with variations in *Norm* (98%) represents best the data in a two years period. This implies flux variations of 97% (21%) in the soft (hard) energy band.

ppendix B.12: NGC 4395

NGC 4395 is a late-type spiral galaxy that holds an intermediate mass black hole. Its nucleus was classified as a Seyfert 1.8 by Ho et al. (1997). nuclear radio source was detected with VLB data (Wrobel & Ho 2006).

NGC 4395 was observed four times with *Chandra* between 2000 and 2004 and six times with *XMM–Newton* between 2002 and 2014. O'Neill et al. (2006) studied three *Chandra* spectra plus the *XMM–Newton* spectrum from November 2003. They reported flux variations of a factor 2 between the *Chandra* and *XMM–Newton* observations. Nardini & Risaliti (2011) studied the *XMM–Newton* data from November 2003 and *Suzaku* data obtained in June 2007. They reported variations related to the covering fraction of the neutral absorber and discussed that this absorber is located in the BLR. These studies agree well with our results. The best representation of the *Chandra* data shows variations in N_{H2} (31%) within one day when fitting SMF1. *XMM–Newton* data require SMF2 with N_{H2} (20%) and $Norm_2$ (88%) varying in 12 years period. This implies flux variability of 15% (13%) in the soft (hard) energy band. When comparing *Chandra* and *XMM–Newton* data, the annular region contributes with

14% in *Chandra* data, and SMF1 is used with variations in N_{H2} (93%) in a two years period.

Dewangan et al. (2008) studied two *XMM–Newton* light curves (2002 May and 2003 November) and reported short-term variations only in the 2003 data. González-Martín & Vaughan (2012) analyzed the *XMM–Newton* observation from November 2003 and reported variations in the total, soft, and hard energy bands. Vaughan et al. (2005) studied the 2003 *XMM–Newton* light curves together and found a high variability amplitude, with the fractional rms exceeding the unity. They found that this source follows the rms-flux relation usually observed in accreting black holes (e.g., Hernández-García et al. 2015b). Moran et al. (2005) studied the *Chandra* data from June 2000 and reported short-term variations from the analysis of the light curve, with changes of a factor of 2–3. They suggested that these changes are related to variations of the absorbing medium. O'Neill et al. (2006) found short-term variations during one of the *Chandra* light curves. One *XMM–Newton* light curve is analyzed in the present work, which shows variations in the soft, hard, and total energy bands.

Time-lags between optical/UV frequencies and X-rays have been studied by McHardy et al. (2016) (using *XMM–Newton*, OM (UVW1 filter) and optical data in the g-band), Cameron et al. (2012) (using *Swift* data), and O'Neill et al. (2006) (using *Chandra* and *HST*/STIS data) and found lags of 473 and 788 s, 400 s, and a zero-lag correlation, respectively, relative to the X-rays.

Variations of this source have also been detected at near-infrared frequencies in timescales shorter than a day by Minezaki et al. (2006). They observed the source in 2004 with the 2 m telescope at the Haleaka Observatories and found variations in he J and H bands correlated with the V band, whereas variations in the K band were not detected.

UV variations are detected in the UVW1 (9) filter using the available OM data.

ppendix B.13: NGC 4565

NGC 4565 is an edgewise spiral galaxy. It was classified as a Seyfert 1.9 in the optical (Ho et al. 1997). compact radio core was detected using *VL* data at 2cm (Nagar et al. 2002). Ho & Ulvestad (2001) suggested that the nucleus may be variable at radio frequencies since flux measurements fluctuated by a factor of 2 between their *VL* data and previous *FIRST* measurements.

This source was observed once by *XMM–Newton* in 2001 and twice by *Chandra* in 2000 and 2003. Cappi et al. (2006) analyzed the *XMM–Newton* data. They fitted the spectrum with an absorbed power law model with $N_H = 0.12^{+}_{-}0.04$ $10^{22} cm^{-2}$, $\Gamma = 1.8^{+}_{-}0.2$, and logL(2–10 keV) = 39.4. They compared their spectral fit to the one reported by Terashima & Wilson (2003) of the *Chandra* data from 2000, finding a good agreement between the spectral parameters and intrinsic luminosities. Our analysis agree well with their spectral fits. We find that SMF1 is the best representation of the data with changes in N_H (48%) in two years period. The annular region contributed with 17% to *Chandra* data.

We examined a *Chandra* light curve and detected possible variations in the soft energy band.

ppendix B.14: M RK 883

It was optically classified as Seyfert 1.9 by Osterbrock & Dahari (1983), who stated that the broad component is 'barely detected', and later classified as a Seyfert 2 (Trippe et al. 2010). radio counterpart was detected at 6 cm with *VL* data (Ulvestad 1986).

This nucleus was observed four times with *XMM–Newton* between 2006 and 2010. Variability studies of this source were not found in the literature. From our analysis we find that SMF1 represents the data best, showing changes in *Norm* (28%) in a timescale of four years. This implies flux variations of 28% in both the soft and hard energy bands.

Data at UV frequencies with the OM are available in the three filters. Variations are detected in the UVW1 (13) and UVW2 (5) filters but not in the UVM2 (1) filter.

ppendix B.15: IR S 20051-1117

IR S 20051–1117 is a luminous spiral galaxy. The line ratios of this galaxy located it in the boundarie between a composite and a Seyfert galaxy (Moran et al. 1996). It shows a broad component, so it was classified as a Seyfert 1.9 using optical data (Georgantopoulos et al. 2004; Shi et al. 2010). radio counterpart was detected with *VL* data at 1.4 GHz (Condon et al. 1998). This is one of the cases where a source is classified as a type 2 GN at optical wavelenghts but shows no absorption at X-ray frequencies (Panessa & Bassani 2002).

It was observed once with *Chandra* and twice with *XMM–Newton* in 2002. Georgantopoulos et al. (2004) and Shi et al. (2010) studied the *Chandra* and one *XMM–Newton* observations and reported no variations between the two epochs, separated by only three weeks. They obtained a luminosity of logL(2–10 keV) = 42.60, in perfect agreement with our estimated luminosity for the same *XMM–Newton* spectrum. Using the two *XMM–Newton* observations, we found that changes in $Norm_2$ (29%) are required in the SMF1 within half a year. This results in flux variations of 29% in both the soft and hard energy bands.

Georgantopoulos et al. (2004) did not find short-term variations in the *Chandra* nor the *XMM–Newton* light curves.

t UV frequencies variations were not detected with the UVW1 (2) filter.

ppendix C: Images

ppendix C.1: Optical spectra, and X-ray, 2M SS and optical HST *images*

In this appendix we present images at different wavelengths for each energy and the optical spectrum when available from NED. In X-rays we extracted *Chandra* data in four energy bands: 0.6-0.9 keV (top left), 1.6-2.0 keV (top middle), 4.5-8.0 keV (top right), and 0.5-10.0 keV (bottom left). The CSMOOTH task included in CI O was used to adaptatively smooth the three images in the top panels (i.e., the images in the 0.5-10.0 keV energy band are not smoothed), using a fast Fourier transform algorithm and a minimum and maximum significance level of the signal-to-noise of 3 and 4, respectively. When data from *Chandra* was not available, *XMM*–Newton images were extracted in the same energy bands, and the ASMOOTH task was used to adaptatively smooth the images. t infrared frequencies, we retrieved an image from 2M SS in the K_s filter[11]. t optical frequencies we used images from the *Hubble* Space telescope (*HST*)[12],

[11] http://irsa.ipac.caltech.edu/applications/2M SS/IM/interactive.html
[12] http://hla.stsci.edu/

preferably in the F814W filter, but when it was not available we retrieved an image in the F606W filter. *HST* data have been processed following the sharp dividing method to show the internal structure of the galaxies (Marquez & Moles 1996). The red squares in the bottom images represent the area covered by the *HST* image (presented in the bottom right panel when available). In all images the gray levels extend from twice the value of the background dispersion to the maximum value at the center of each galaxy. We used IR F [13] to estimate these values.

[13] http://iraf.noao.edu/

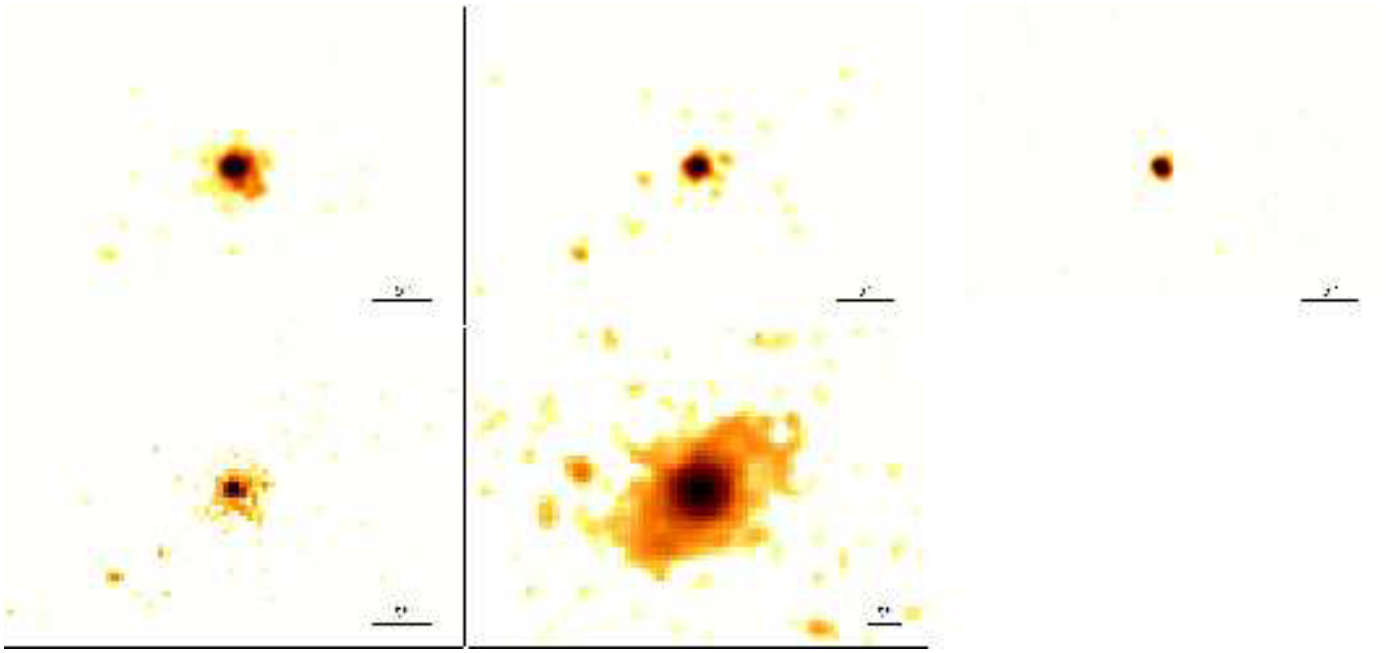

Fig. C.1: Images of ESO 540-G01. (Top left): Smoothed X-ray 0.6-0.9 keV energy band; (top center): smoothed X-ray 1.6-2.0 keV energy band; (top right): smoothed X-ray 4.5-8.0 keV energy band; (bottom left): X-ray 0.5-10.0 keV energy band without smoothing; (bottom center): 2M SS image in the K_s band.

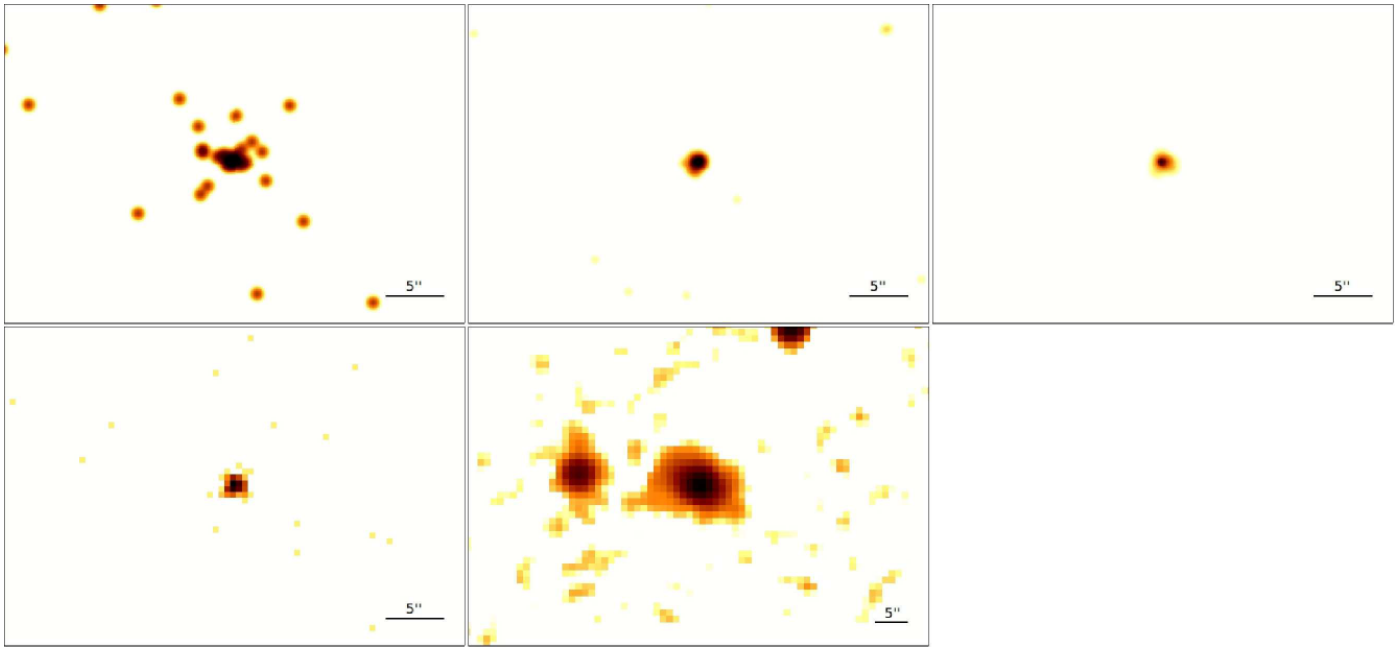

Fig. C.2: Images of ESO 195-IG21. (Top left): Smoothed X-ray 0.6-0.9 keV energy band; (top center): smoothed X-ray 1.6-2.0 keV energy band; (top right): smoothed X-ray 4.5-8.0 keV energy band; (bottom left): X-ray 0.5-10.0 keV energy band without smoothing; (bottom center): 2M SS image in the K_s band.

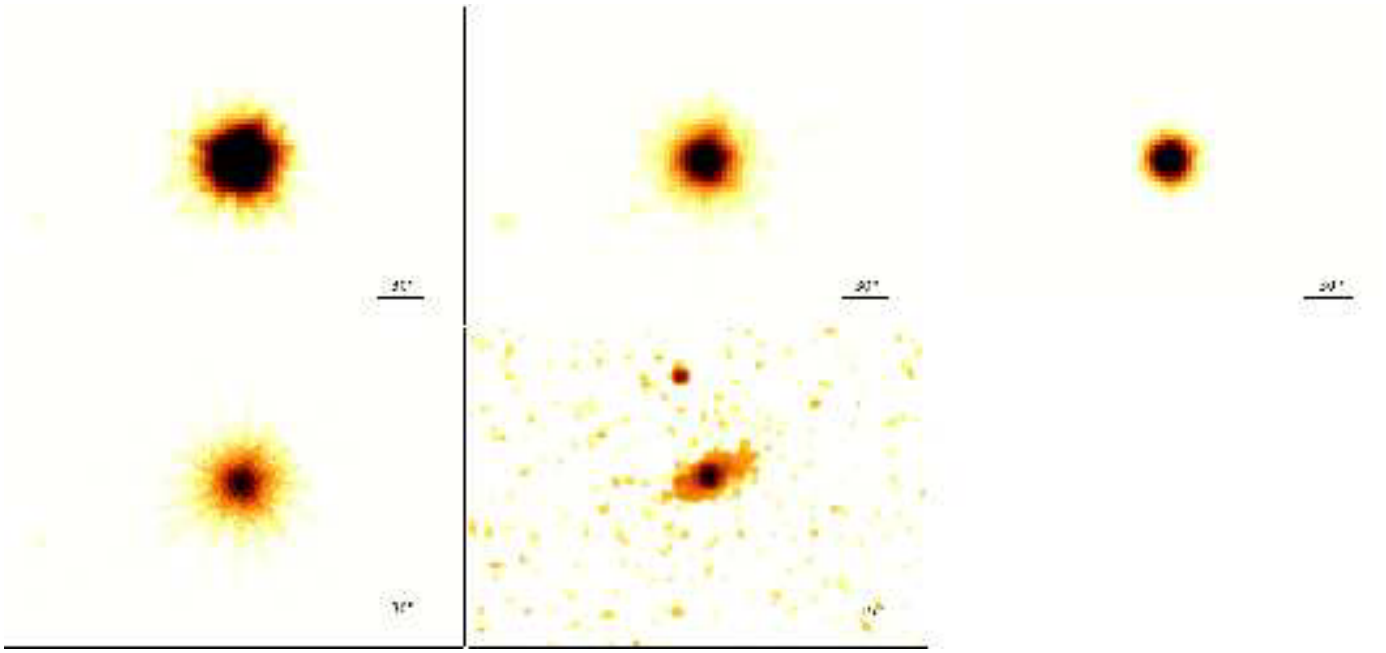

Fig. C.3: Images of ESO 113-G10. (Top left): Smoothed X-ray 0.6-0.9 keV energy band; (top center): smoothed X-ray 1.6-2.0 keV energy band; (top right): smoothed X-ray 4.5-8.0 keV energy band; (bottom left): X-ray 0.5-10.0 keV energy band without smoothing; (bottom center): 2M SS image in the K_s band.

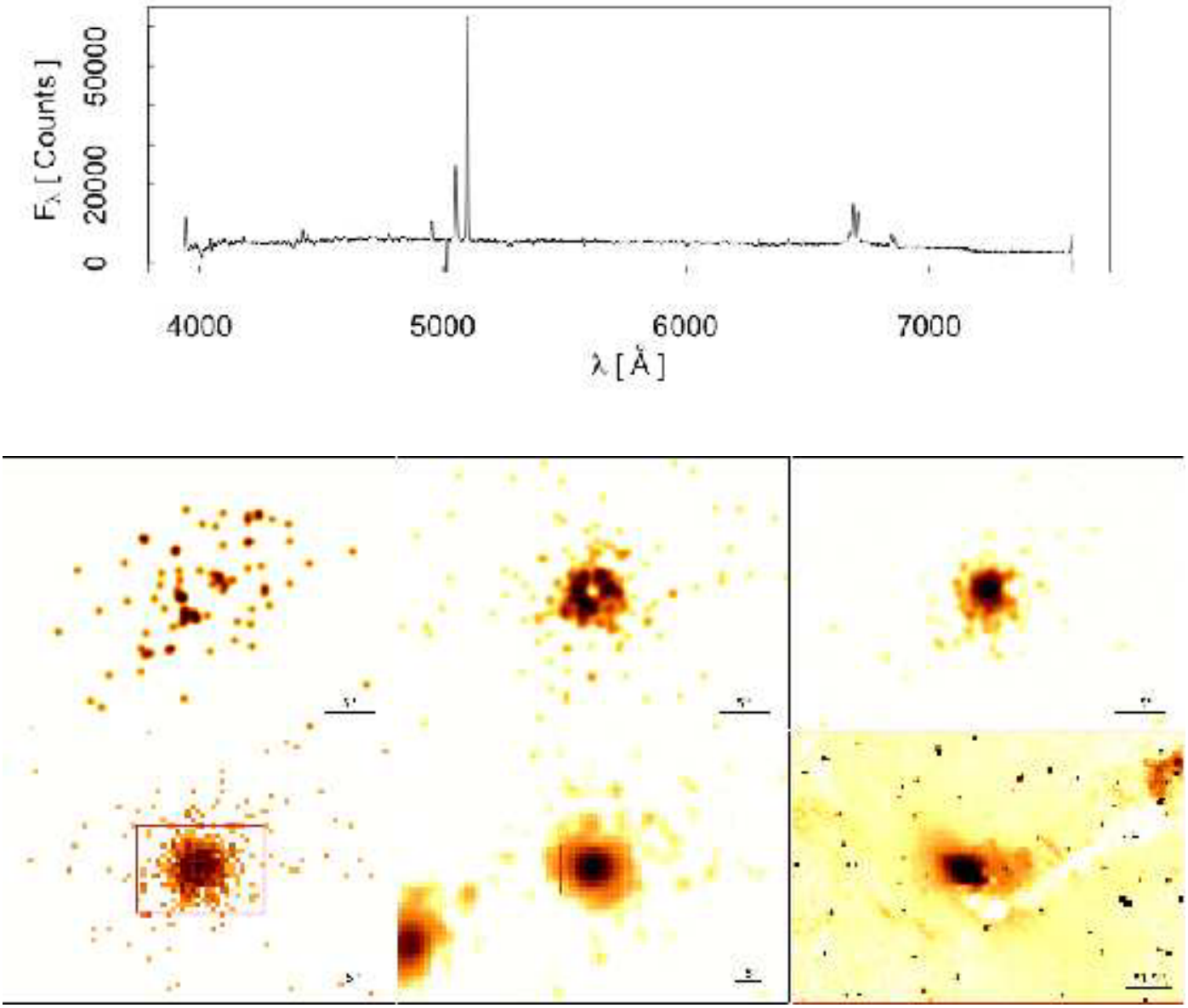

Fig. C.4: Up: Optical spectrum (from NED); bottom: images of NGC 526 . (Top left): Smoothed X-ray 0.6-0.9 keV energy band; (top center): smoothed X-ray 1.6-2.0 keV energy band; (top right): smoothed X-ray 4.5-8.0 keV energy band; (bottom left): X-ray 0.5-10.0 keV energy band without smoothing; (bottom center): 2M SS image in the K_s band; (bottom right): Sharp divided Hubble image in the F606W filter.

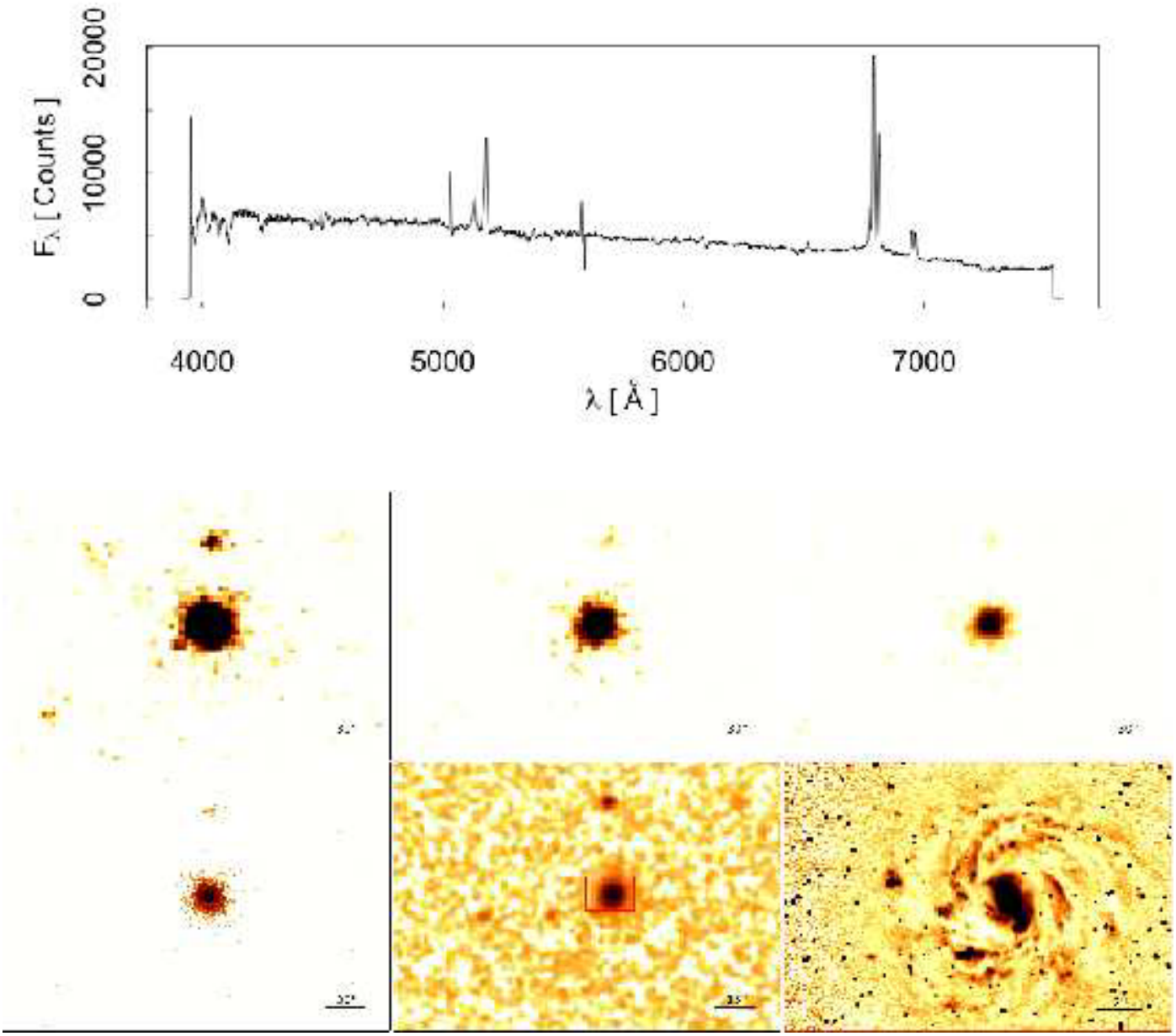

Fig. C.5: Up: Optical spectrum (from NED); bottom: images of M RK 609. (Top left): Smoothed X-ray 0.6-0.9 keV energy band; (top center): smoothed X-ray 1.6-2.0 keV energy band; (top right): smoothed X-ray 4.5-8.0 keV energy band; (bottom left): X-ray 0.5-10.0 keV energy band without smoothing; (bottom center): 2M SS image in the K_s band; (bottom right): Sharp divided Hubble image in the F606W filter.

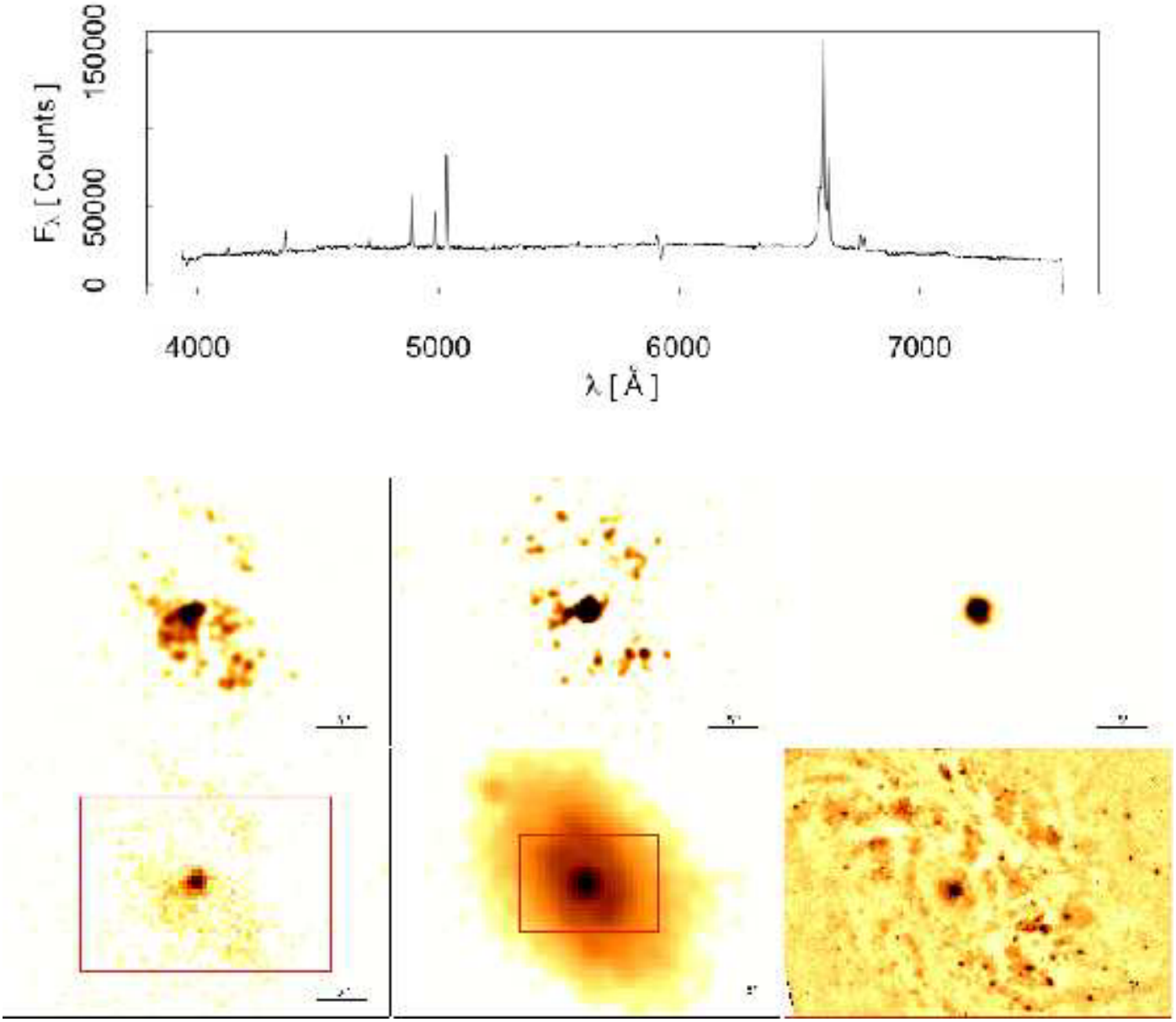

Fig. C.6: Up: Optical spectrum (from NED); bottom: images of NGC 1365. (Top left): Smoothed X-ray 0.6-0.9 keV energy band; (top center): smoothed X-ray 1.6-2.0 keV energy band; (top right): smoothed X-ray 4.5-8.0 keV energy band; (bottom left): X-ray 0.5-10.0 keV energy band without smoothing; (bottom center): 2M SS image in the K_s band; (bottom right): Sharp divided Hubble image in the F814W filter.

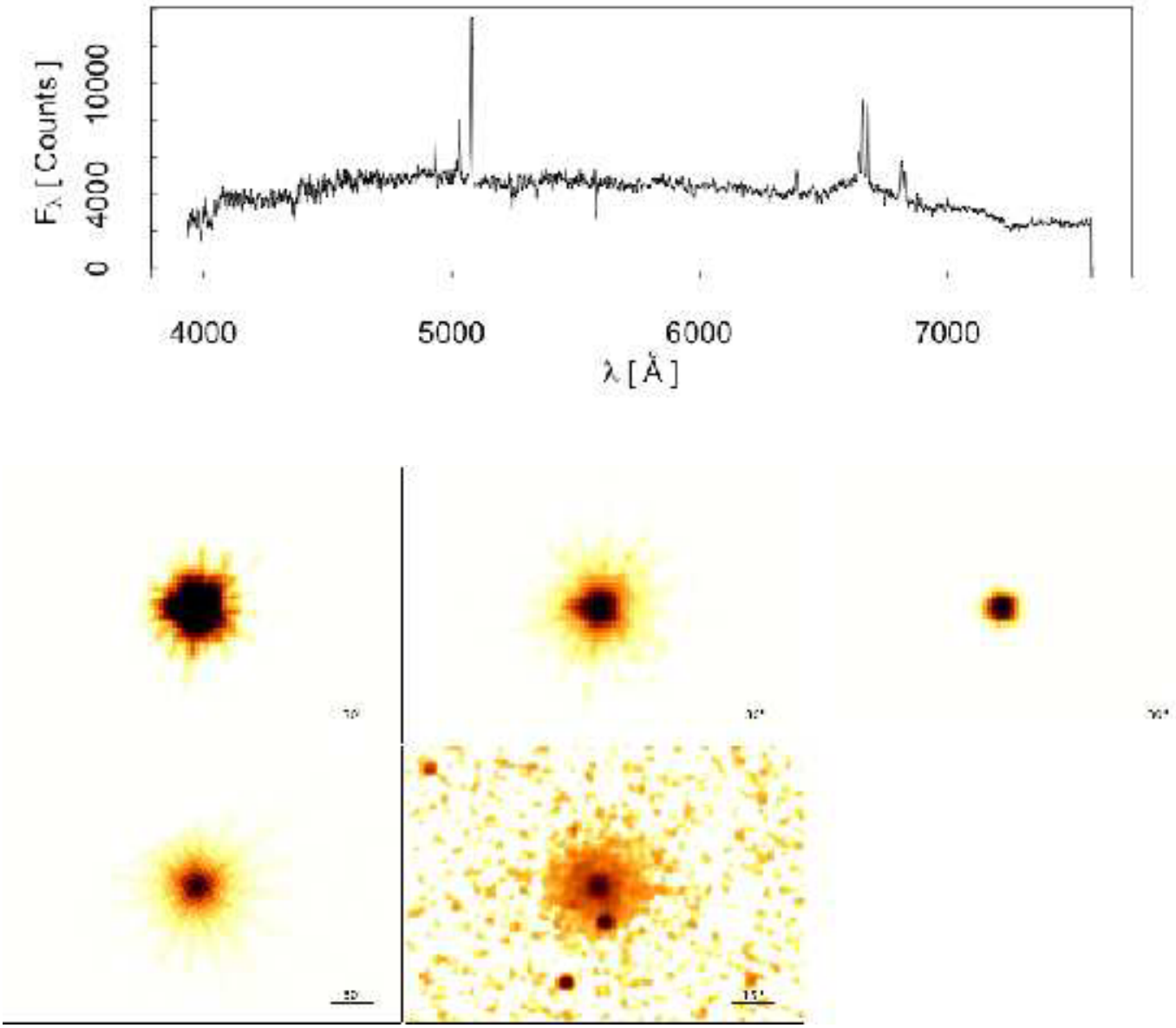

Fig. C.7: Up: Optical spectrum (from NED); bottom: images of NGC 2617. (Top left): Smoothed X-ray 0.6-0.9 keV energy band; (top center): smoothed X-ray 1.6-2.0 keV energy band; (top right): smoothed X-ray 4.5-8.0 keV energy band; (bottom left): X-ray 0.5-10.0 keV energy band without smoothing; (bottom center): 2M SS image in the K_s band.

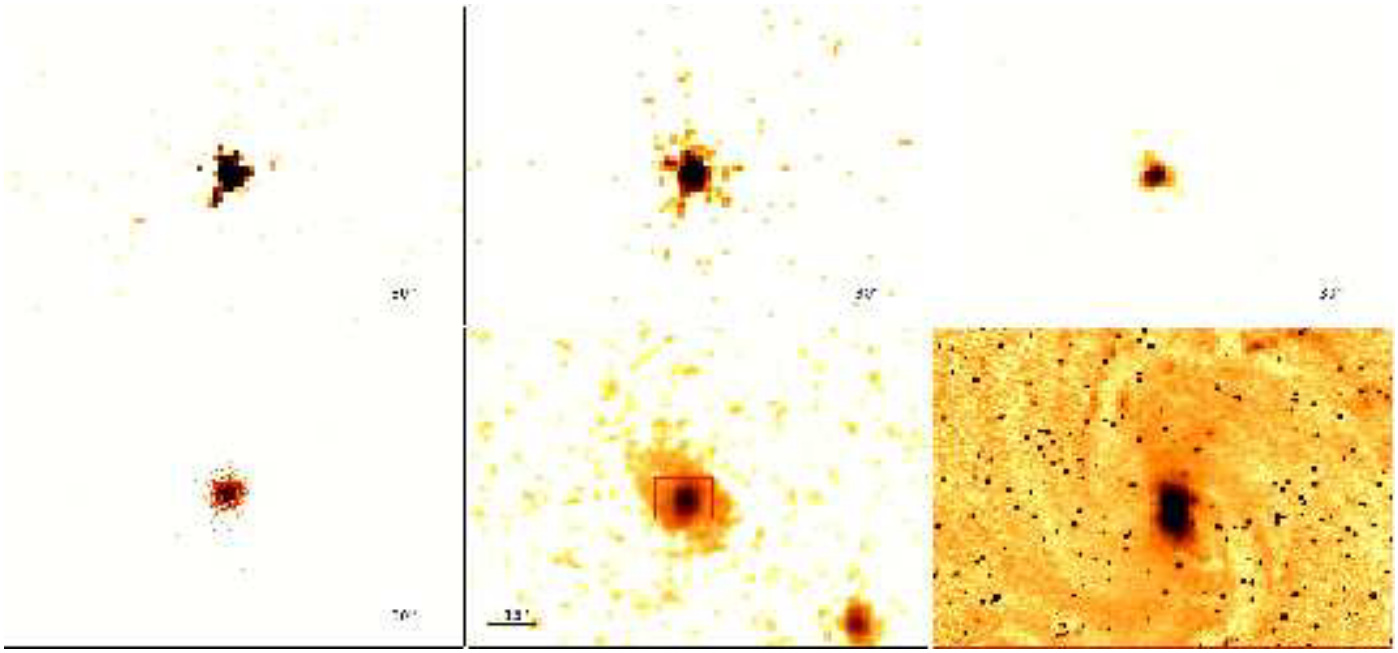

Fig. C.8: Images of M RK 1218. (Top left): Smoothed X-ray 0.6-0.9 keV energy band; (top center): smoothed X-ray 1.6-2.0 keV energy band; (top right): smoothed X-ray 4.5-8.0 keV energy band; (bottom left): X-ray 0.5-10.0 keV energy band without smoothing; (bottom center): 2M SS image in the K_s band; (bottom right): Sharp divided Hubble image in the F606W filter.

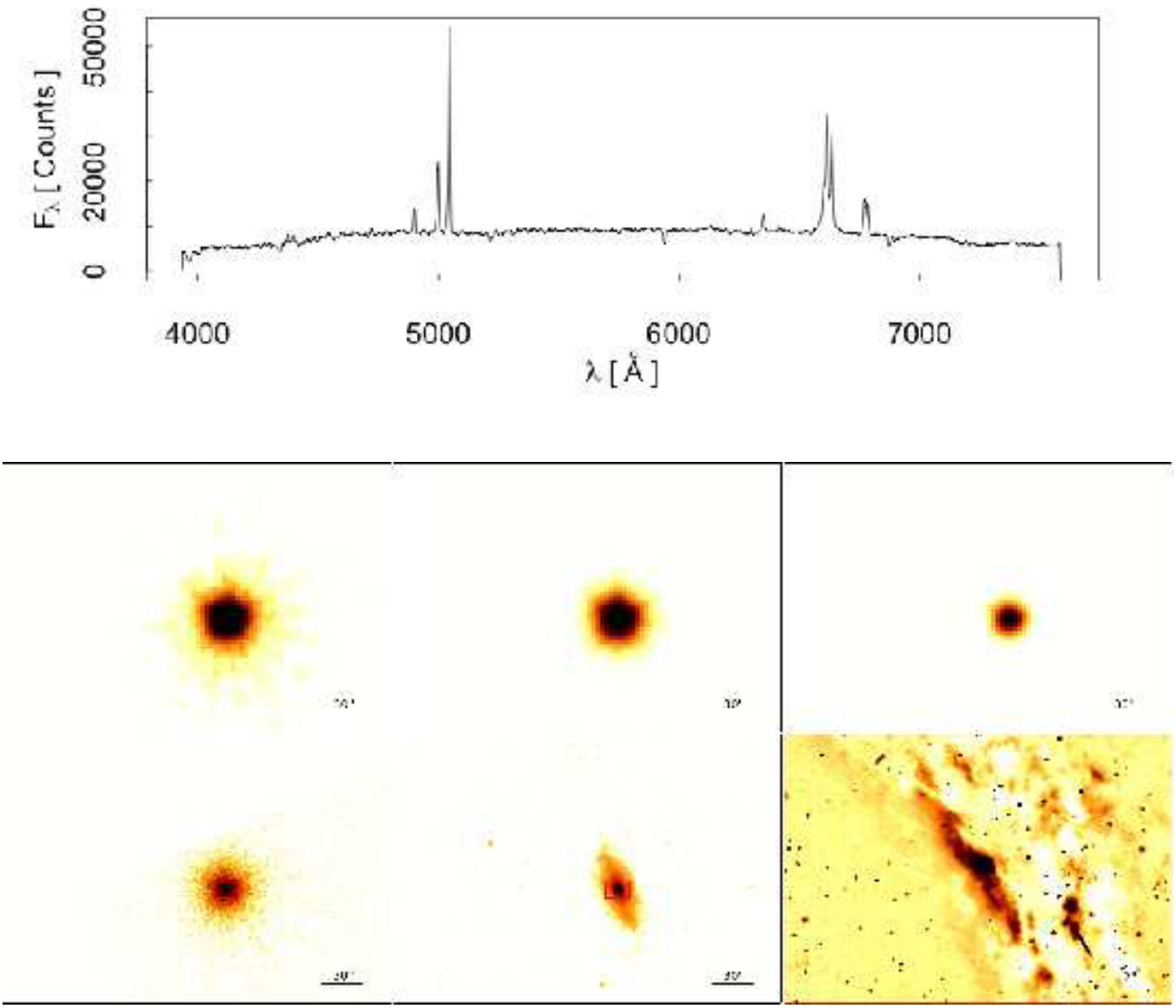

Fig. C.9: Up: Optical spectrum (from NED); bottom: images of NGC 2992. (Top left): Smoothed X-ray 0.6-0.9 keV energy band; (top center): smoothed X-ray 1.6-2.0 keV energy band; (top right): smoothed X-ray 4.5-8.0 keV energy band; (bottom left): X-ray 0.5-10.0 keV energy band without smoothing; (bottom center): 2M SS image in the K_s band; (bottom right): Sharp divided Hubble image in the F606W filter.

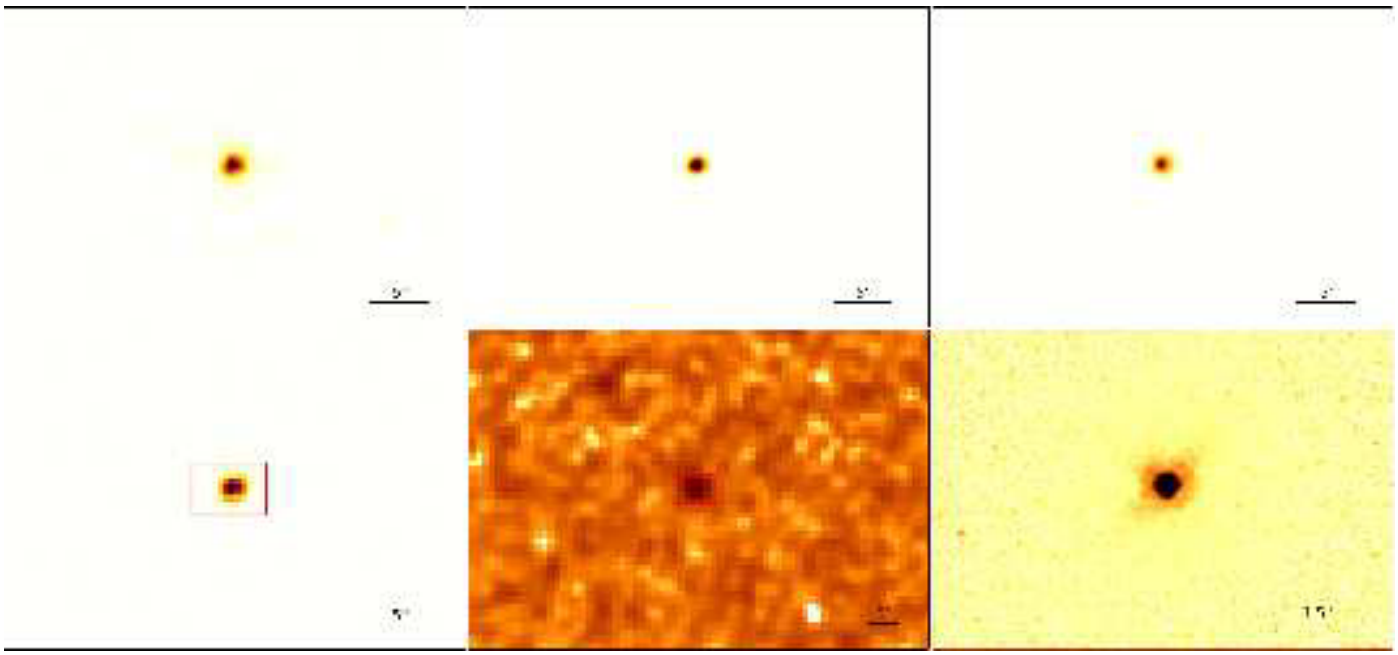

Fig. C.10: images of POX 52. (Top left): Smoothed X-ray 0.6-0.9 keV energy band; (top center): smoothed X-ray 1.6-2.0 keV energy band; (top right): smoothed X-ray 4.5-8.0 keV energy band; (bottom left): X-ray 0.5-10.0 keV energy band without smoothing; (bottom center): 2M SS image in the K_s band; (bottom right): Sharp divided Hubble image in the F814W filter.

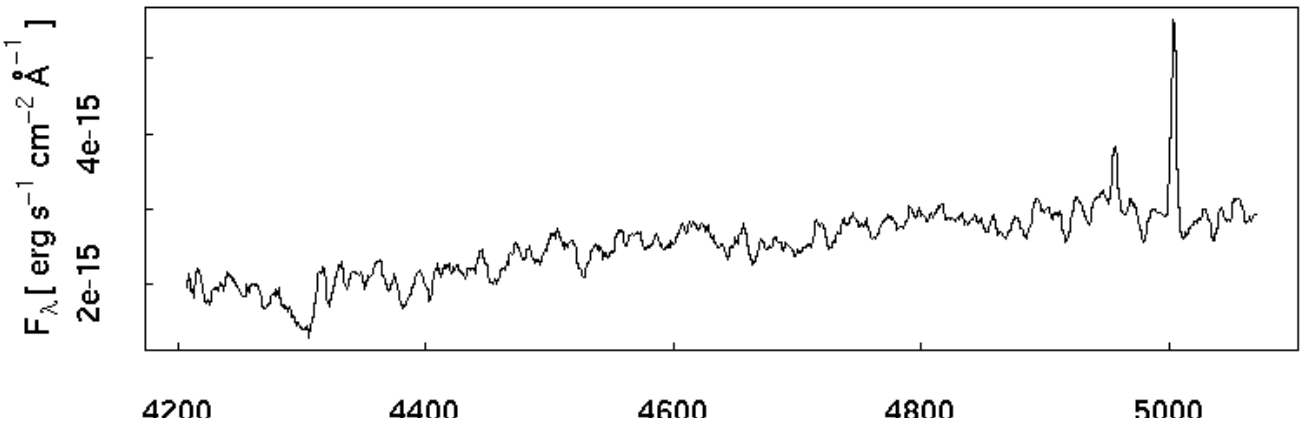
F_λ [erg s^{-1} cm^{-2} Å^{-1}]
2e-15
4e-15
4200
4400
4600
4800
5000

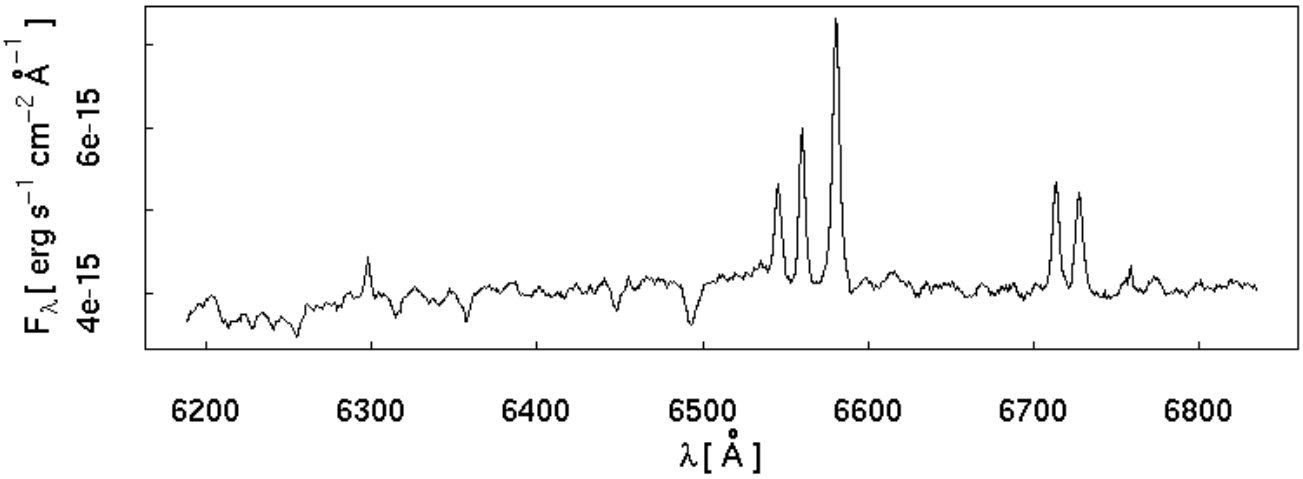
F_λ [erg s^{-1} cm^{-2} Å^{-1}]
4e-15
6e-15
6200
6300
6400
6500
6600
6700
6800
λ [Å]

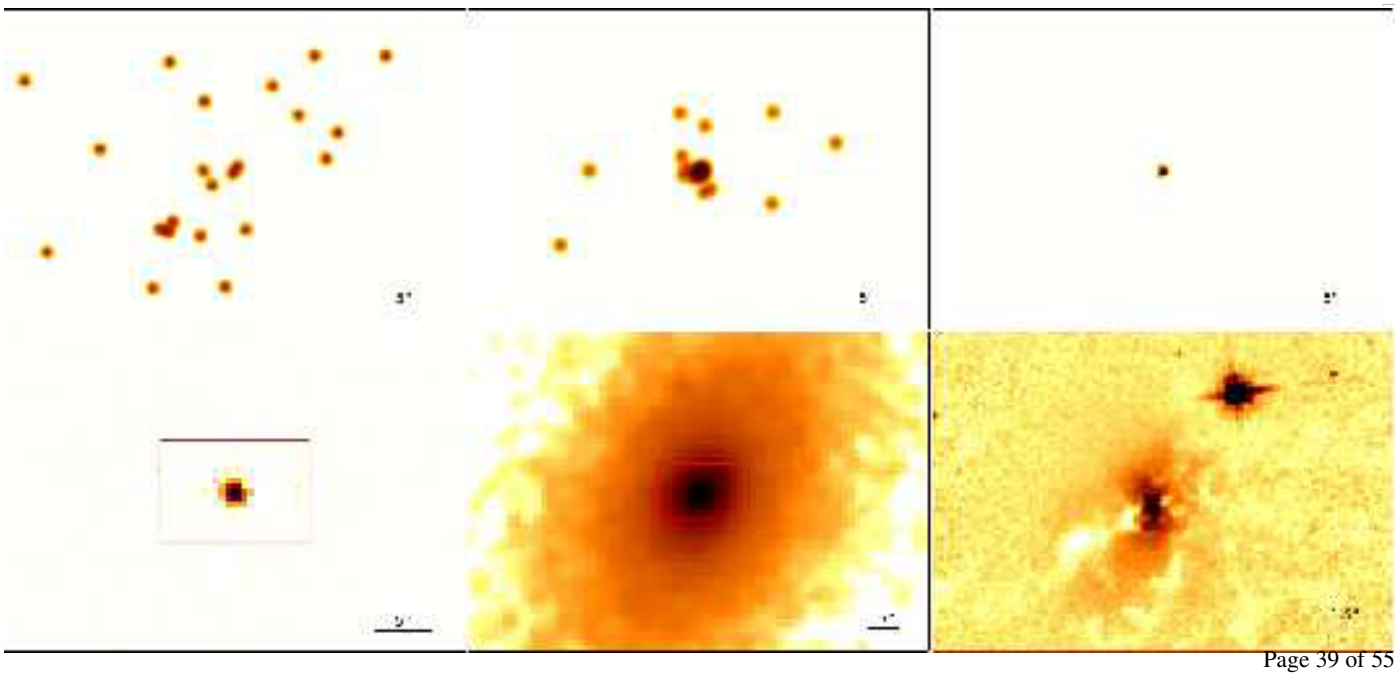

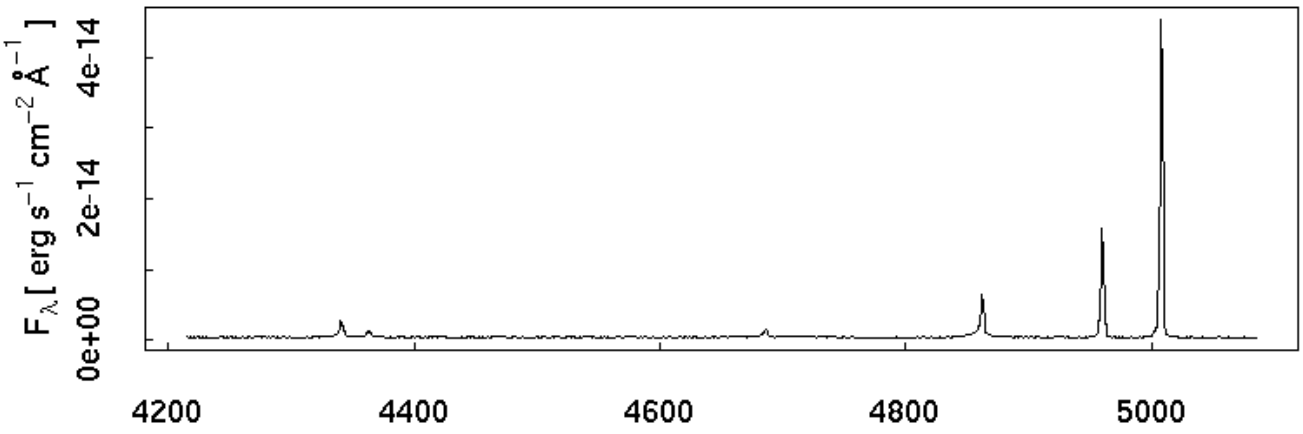
F_λ[erg s^{-1} cm^{-2} Å^{-1}]
0e+00
2e-14
4e-14
4200
4400
4600
4800
5000

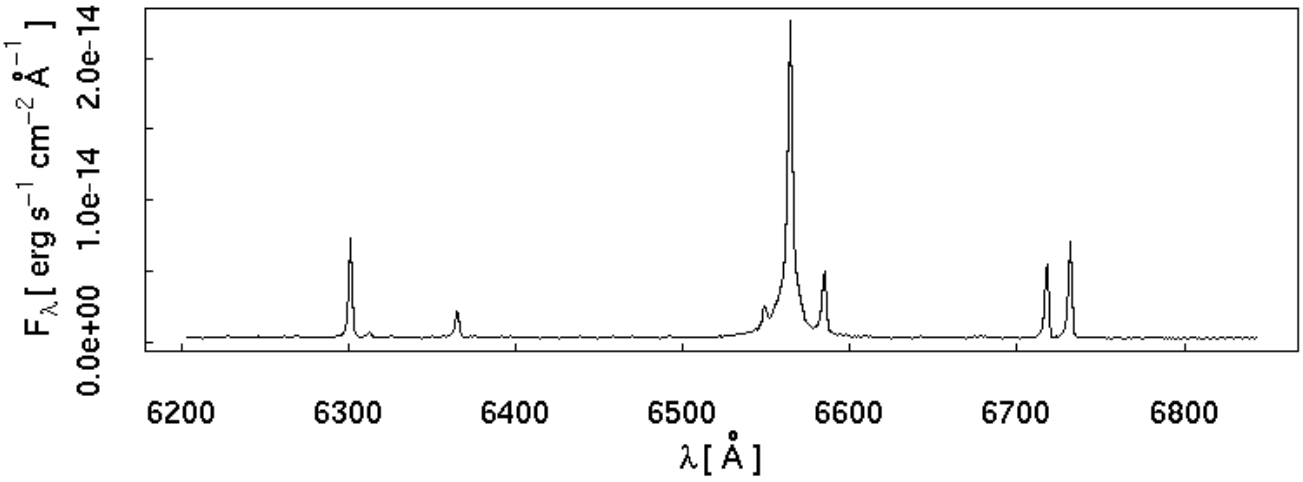
F_λ[erg s^{-1} cm^{-2} Å^{-1}]
0.0e+00
1.0e-14
2.0e-14
6200
6300
6400
6500
6600
6700
6800
λ[Å]

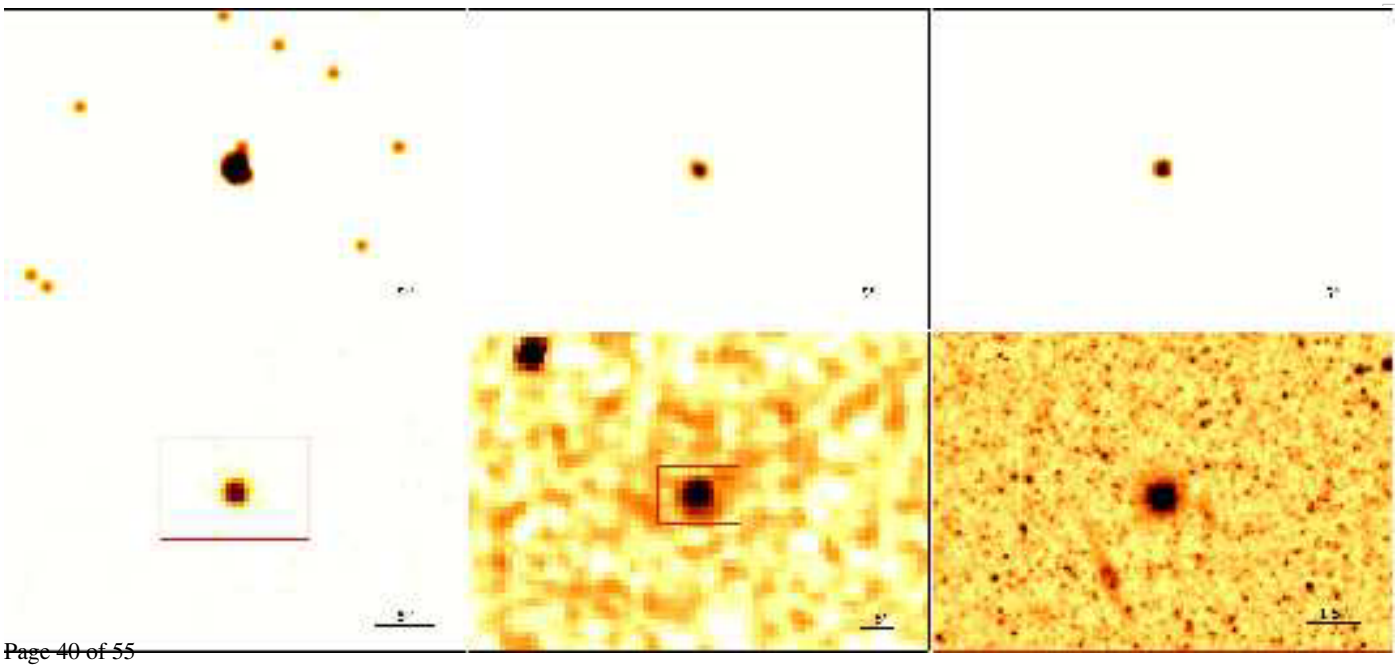

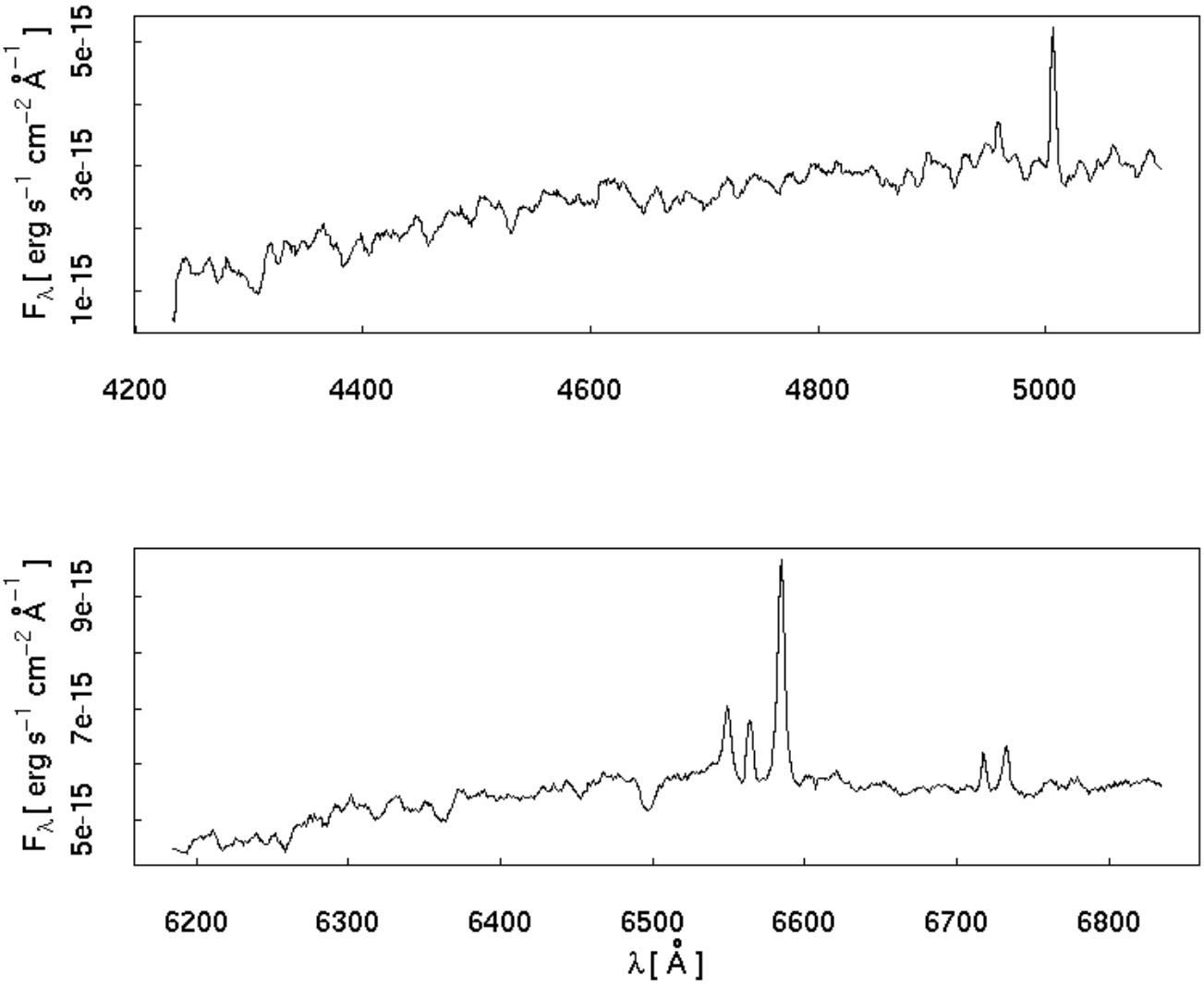
F_λ [erg s^{-1} cm^{-2} Å^{-1}]
1e-15
3e-15
5e-15
4200
4400
4600
4800
5000
F_λ [erg s^{-1} cm^{-2} Å^{-1}]
5e-15
7e-15
9e-15
6200
6300
6400
6500
6600
6700
6800
λ [Å]

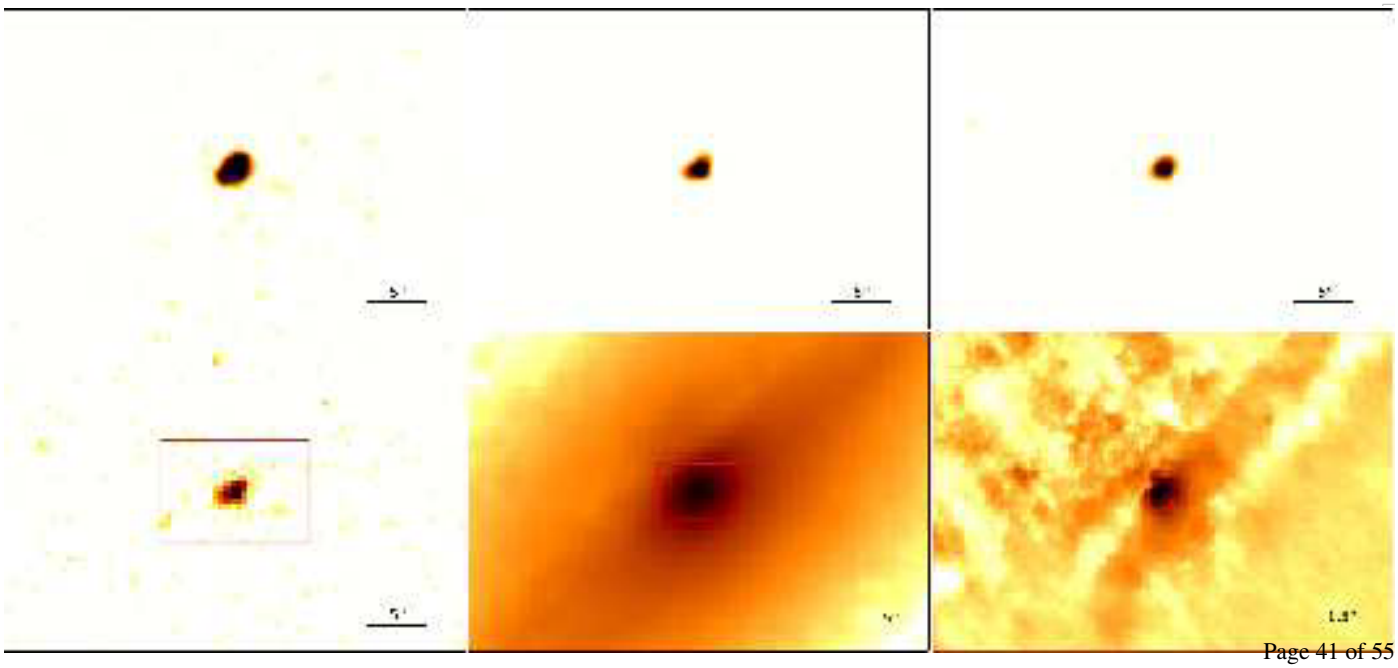

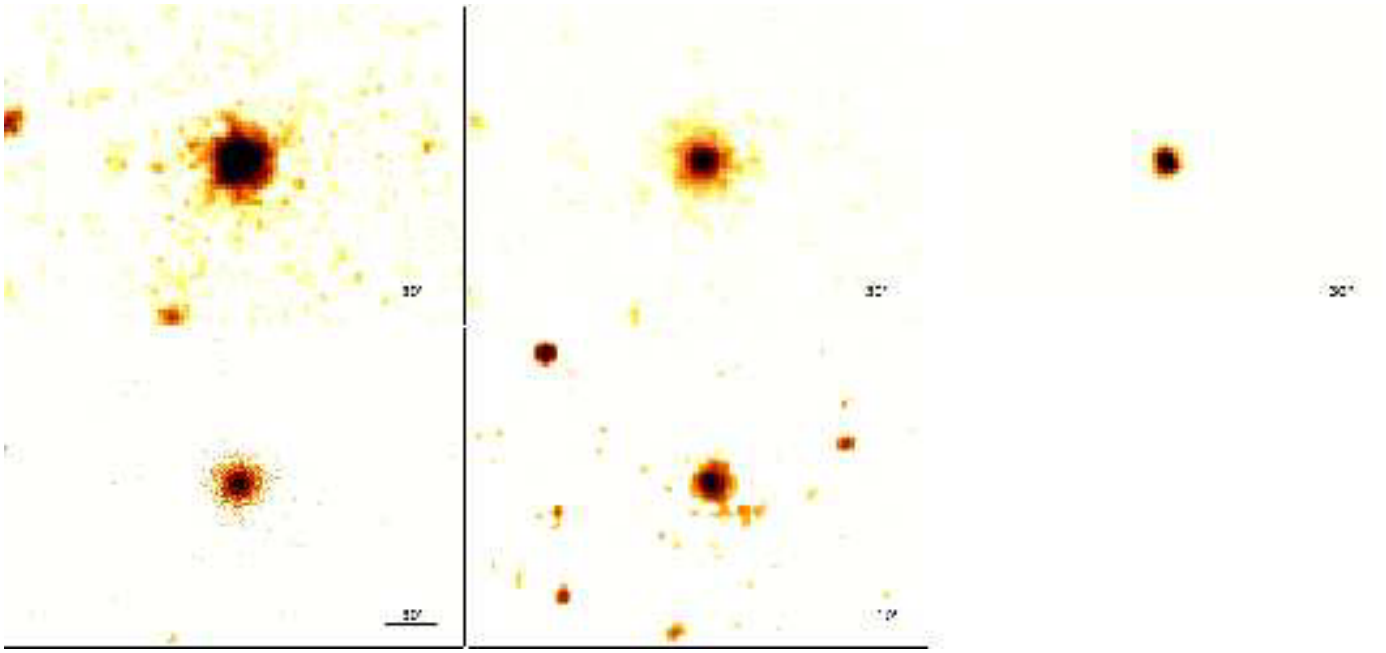

Fig. C.14: Images of M RK 883. (Top left): Smoothed X-ray 0.6-0.9 keV energy band; (top center): smoothed X-ray 1.6-2.0 keV energy band; (top right): smoothed X-ray 4.5-8.0 keV energy band; (bottom left): X-ray 0.5-10.0 keV energy band without smoothing; (bottom center): 2M SS image in the K_s band.

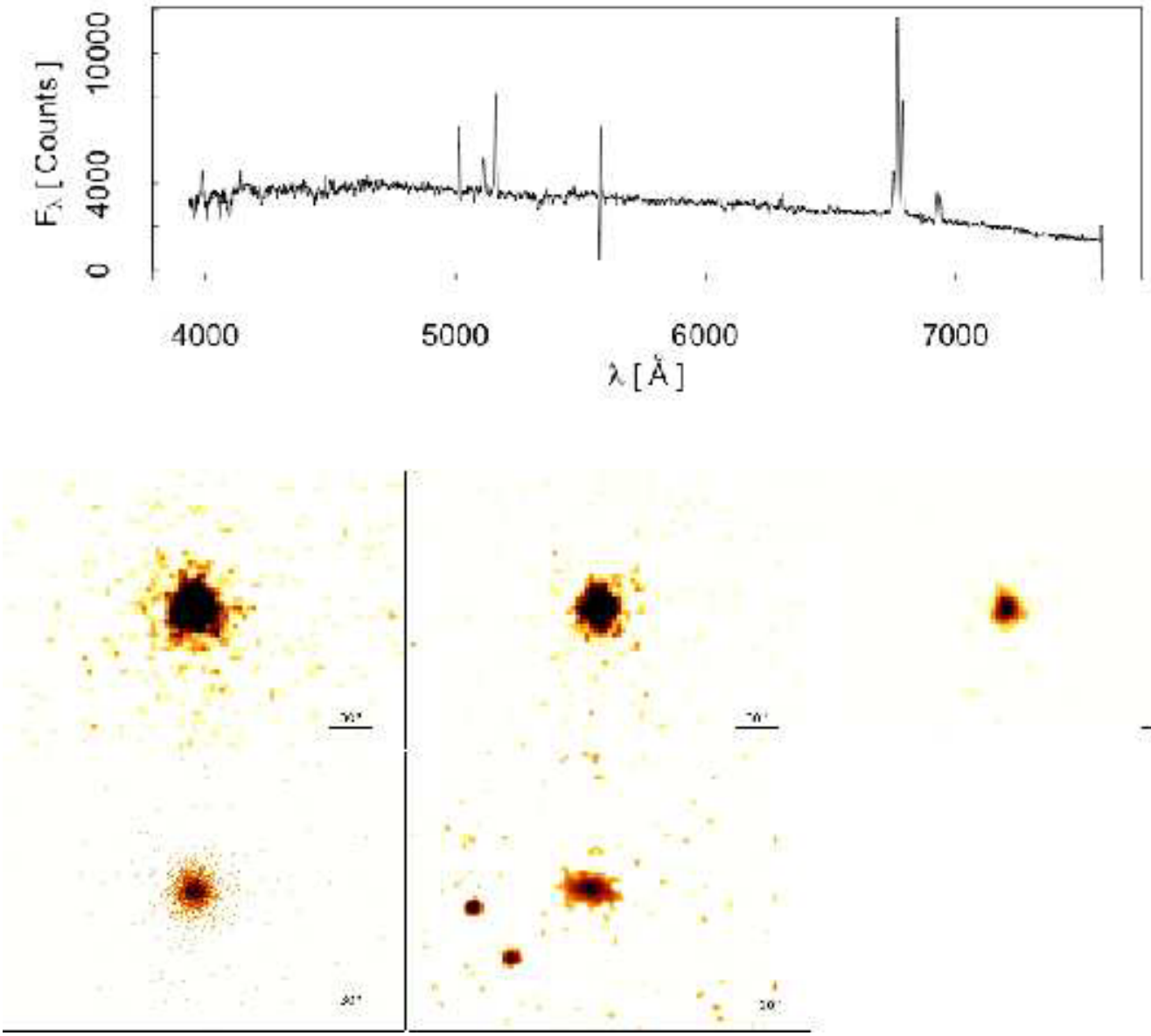

Fig. C.15: Up: Optical spectrum (from NED); bottom: images of IR S 20051-1117. (Top left): Smoothed X-ray 0.6-0.9 keV energy band; (top center): smoothed X-ray 1.6-2.0 keV energy band; (top right): smoothed X-ray 4.5-8.0 keV energy band; (bottom left): X-ray 0.5-10.0 keV energy band without smoothing; (bottom center): 2M SS image in the K_s band.

ppendix C.2: Chandra *and* XMM–*Newton images*

In this appendix we present the images from *Chandra* (left) and *XMM*-Newton (right) that were used to compare the spectra from these two instruments in the 0.5-10 keV band. In all cases, the gray scales extend from twice the value of the background dispersion to the maximum value at the center of each galaxy.

Fig. C.16: Images for *Chandra* data (left) and *XMM–Newton* data (right) for the sources in the 0.5-10 keV band. Big circles represent *XMM-Newton* data apertures. Small circles in the figures to the left represent the nuclear extraction aperture used with *Chandra* observations (see Table .1).

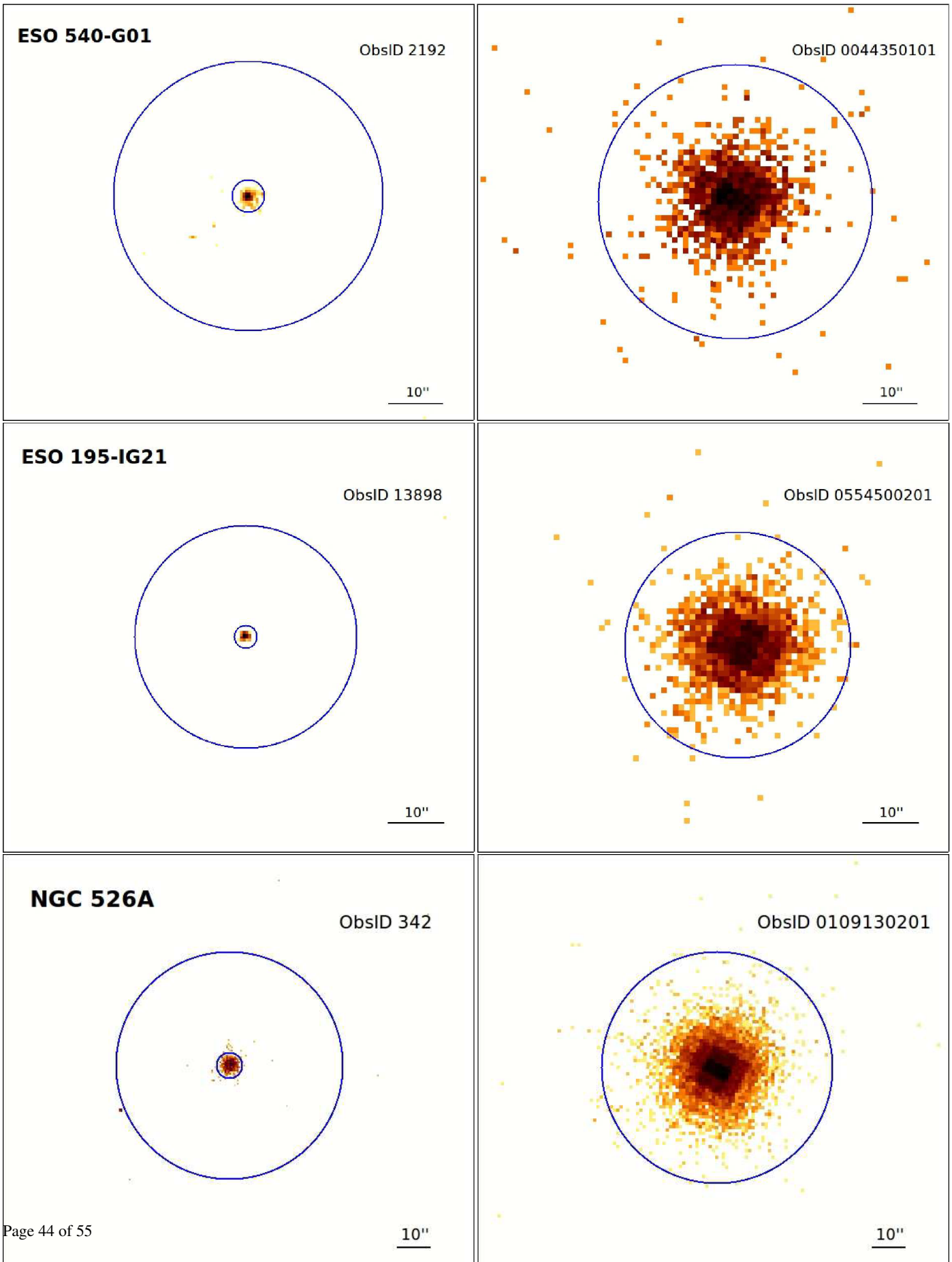

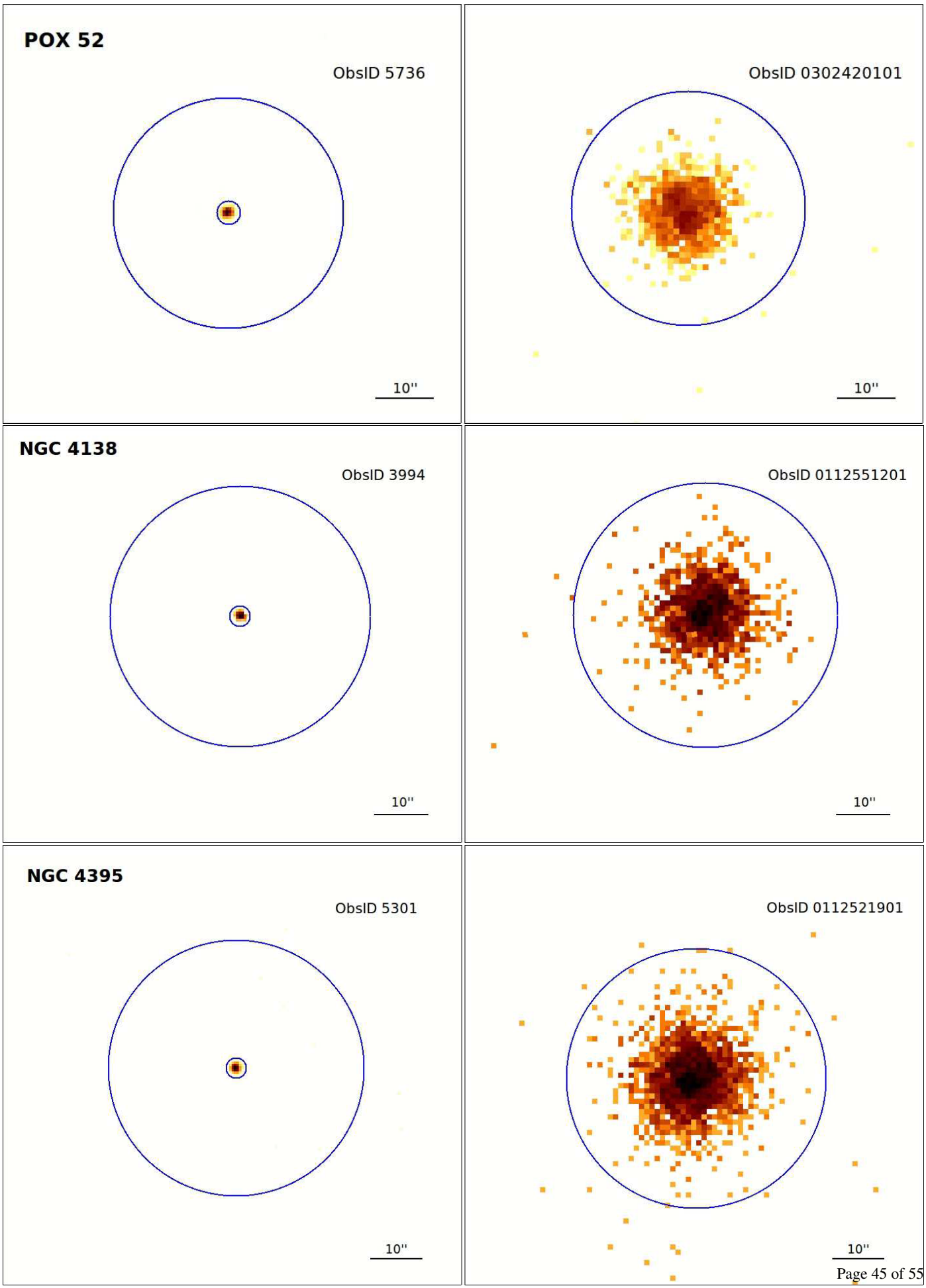
POX 52
ObsID 5736
10''
ObsID 0302420101
10''
NGC 4138
ObsID 3994
10''
ObsID 0112551201
10''
NGC 4395
ObsID 5301
10''
ObsID 0112521901
10''

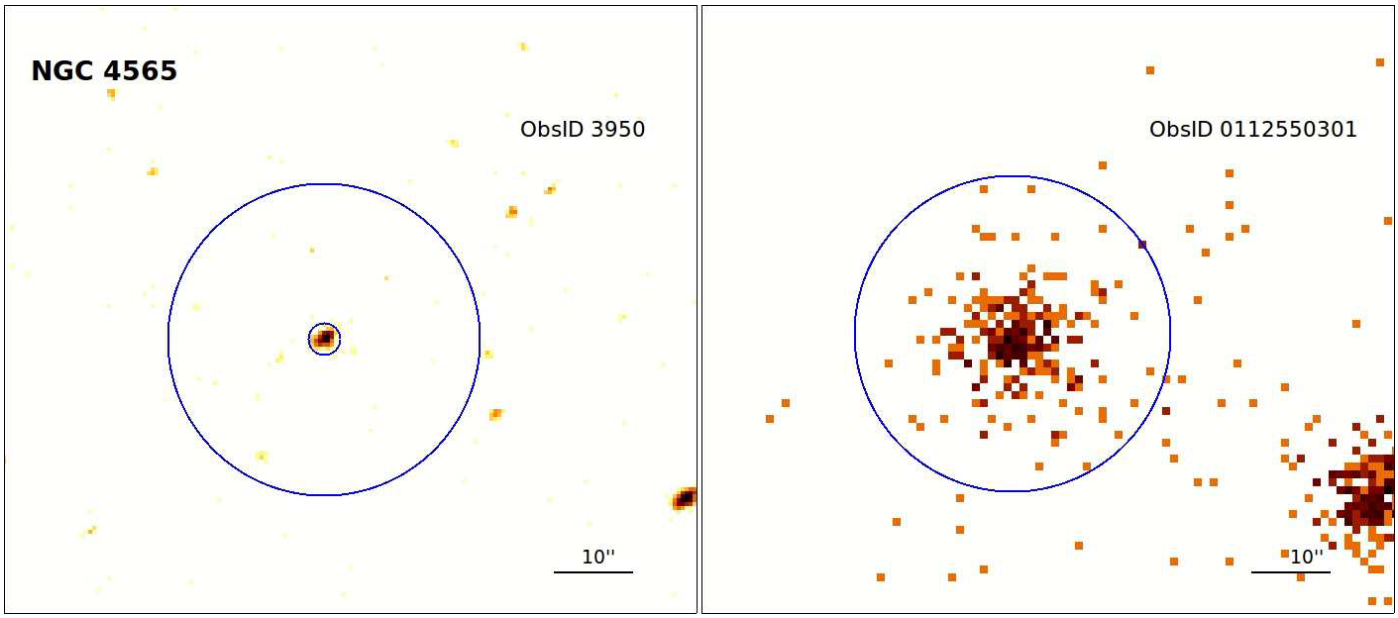
NGC 4565
ObsID 3950
10''
ObsID 0112550301
10''

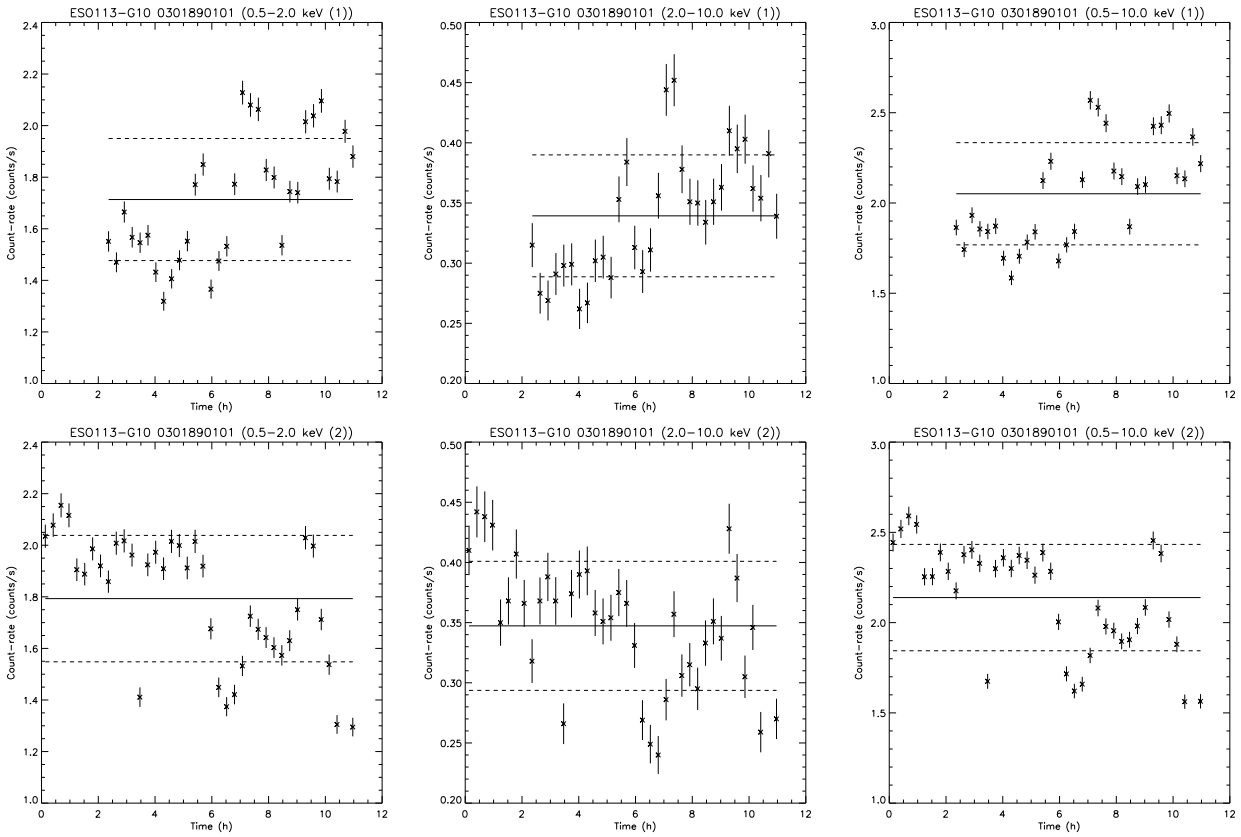

Fig. D.1: Light curves of ESO 113-G10 from *XMM–Newton* data.

ppendix D: Light curves

This appendix provides the plots corresponding to the light curves. Three plots per observation are presented, corresponding to soft (left), hard (middle), and total (right) energy bands. Each light curve has a minimum of 30 ksec (i.e., 8 hours) exposure time, while long light curves are divided into segments of 40 ksec (i.e., 11 hours). Each segment is enumerated in the title of the light curve. Count rates versus time continua are represented. The solid line represents the mean value, dashed lines the $^{+}_{-}1$ from the average.

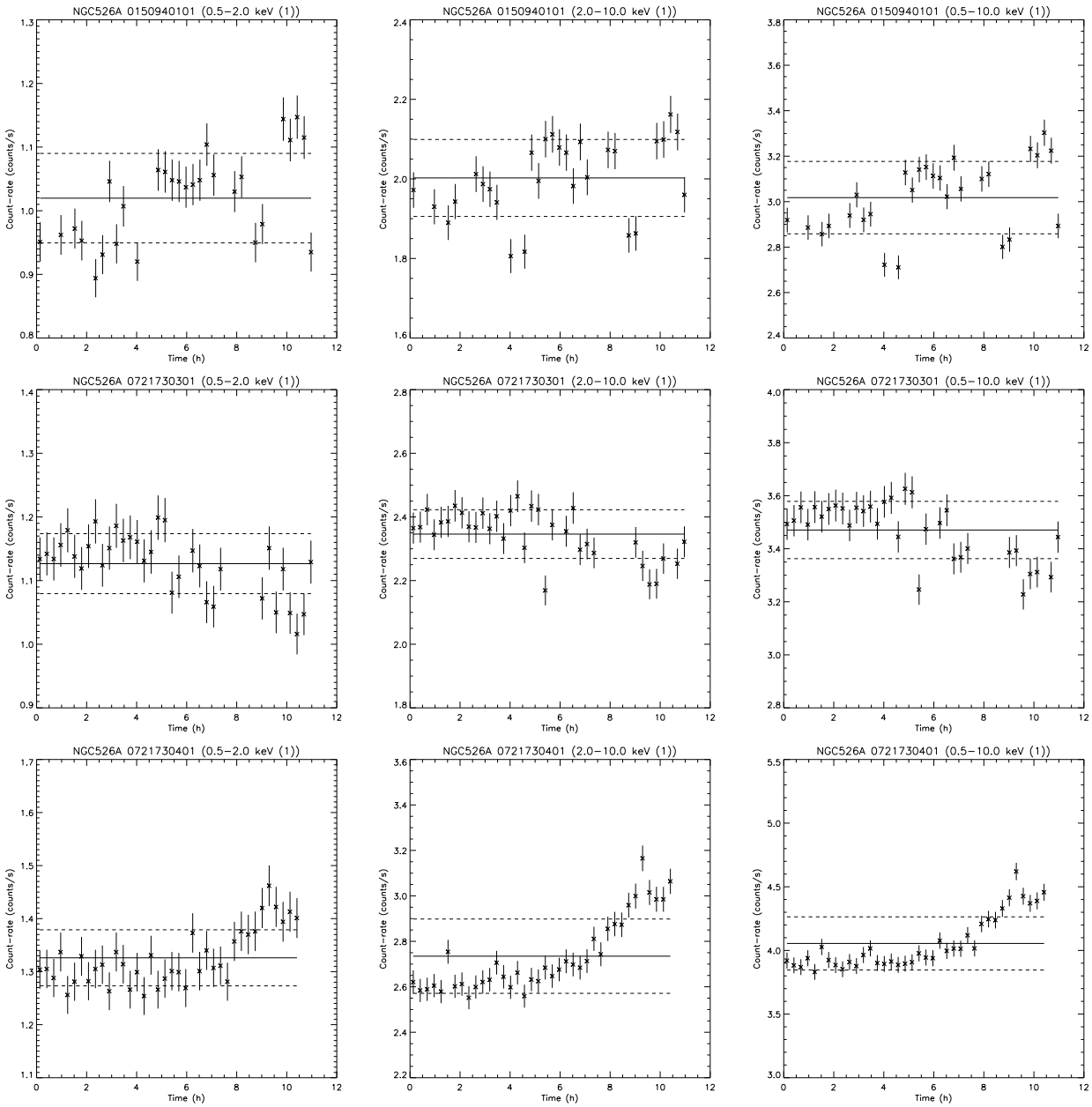

Fig. D.2: Light curves of NGC 526 from *XMM–Newton* data.

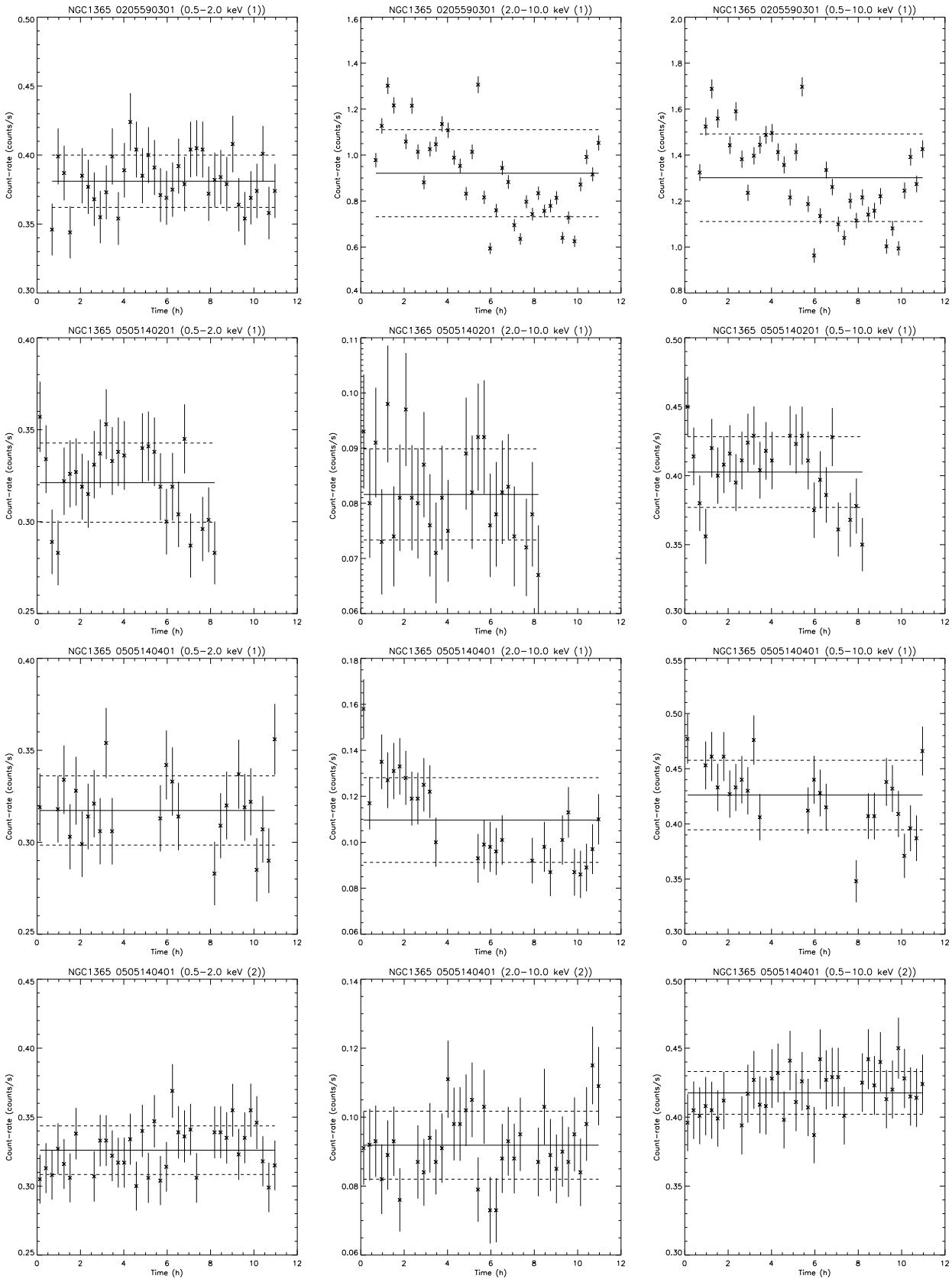

Fig. D.3: Light curves of NGC 1365 from *XMM–Newton* data.

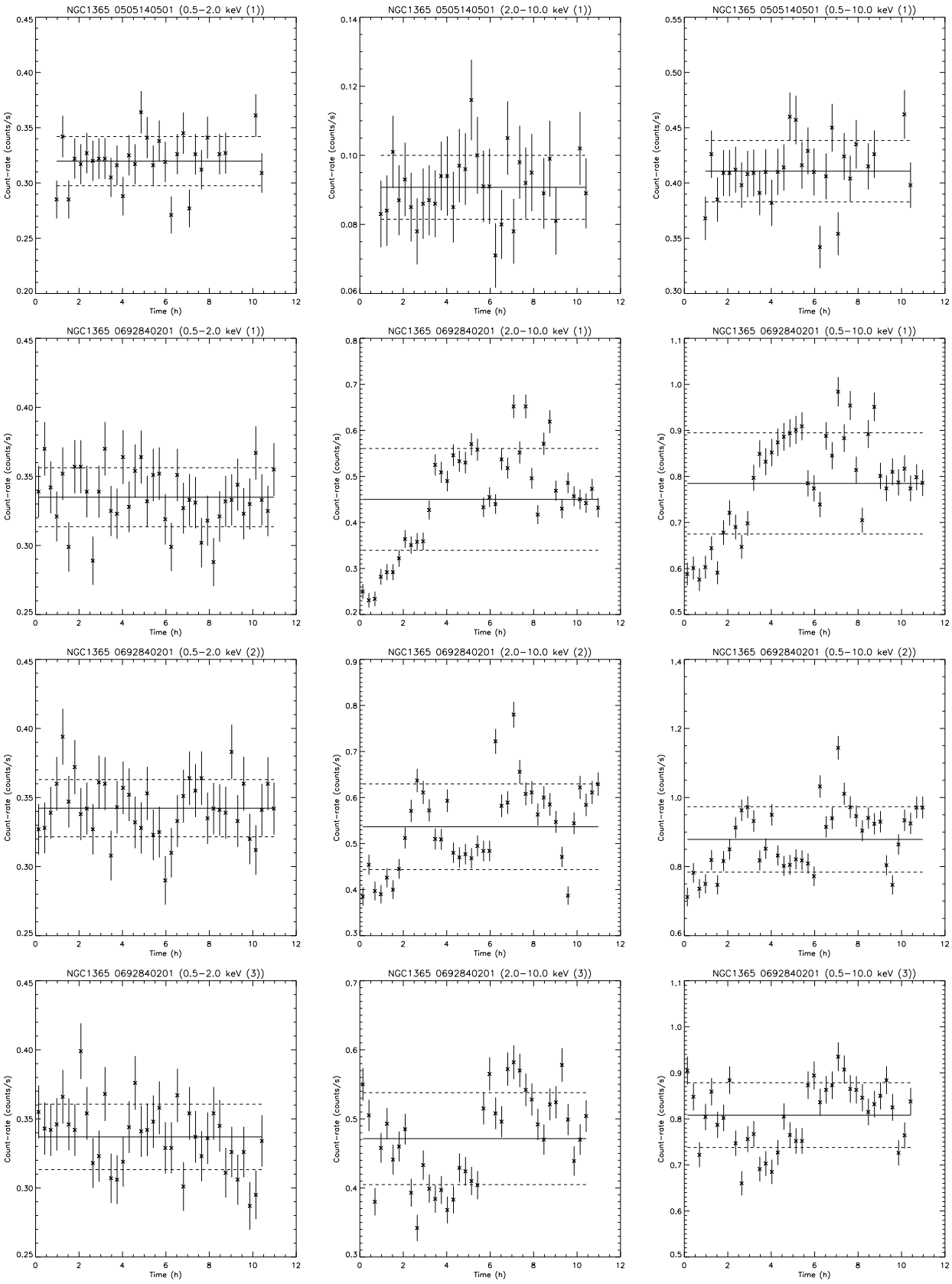
NGC1365 0505140501 (0.5−2.0 keV (1))
NGC1365 0505140501 (2.0−10.0 keV (1))
NGC1365 0505140501 (0.5−10.0 keV (1))
NGC1365 0692840201 (0.5−2.0 keV (1))
NGC1365 0692840201 (2.0−10.0 keV (1))
NGC1365 0692840201 (0.5−10.0 keV (1))
NGC1365 0692840201 (0.5−2.0 keV (2))
NGC1365 0692840201 (2.0−10.0 keV (2))
NGC1365 0692840201 (0.5−10.0 keV (2))
NGC1365 0692840201 (0.5−2.0 keV (3))
NGC1365 0692840201 (2.0−10.0 keV (3))
NGC1365 0692840201 (0.5−10.0 keV (3))
Count-rate (counts/s)
Time (h)

Fig. D.3: (Cont.)

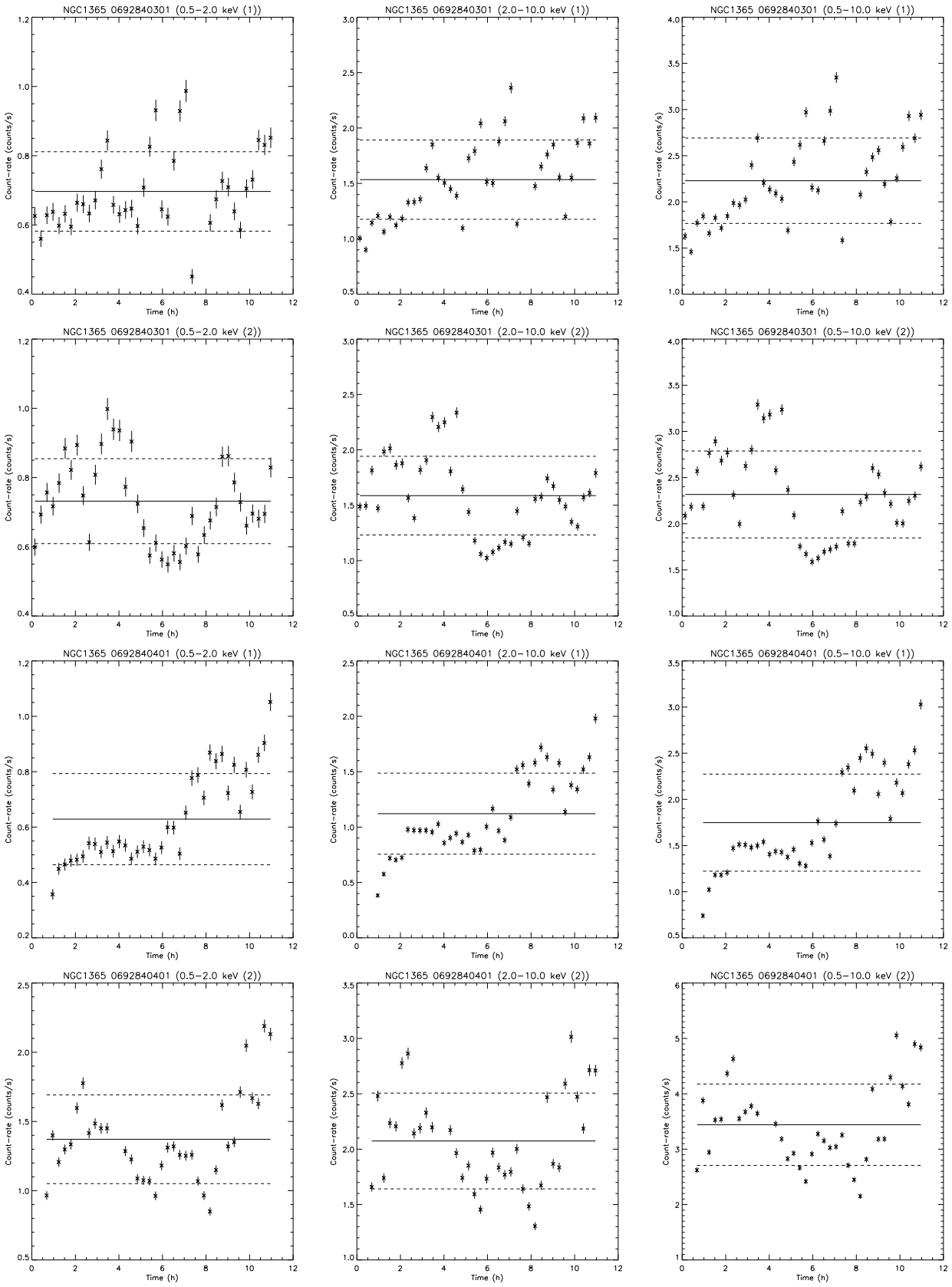
NGC1365 0692840301 (0.5−2.0 keV (1))
NGC1365 0692840301 (2.0−10.0 keV (1))
NGC1365 0692840301 (0.5−10.0 keV (1))
NGC1365 0692840301 (0.5−2.0 keV (2))
NGC1365 0692840301 (2.0−10.0 keV (2))
NGC1365 0692840301 (0.5−10.0 keV (2))
NGC1365 0692840401 (0.5−2.0 keV (1))
NGC1365 0692840401 (2.0−10.0 keV (1))
NGC1365 0692840401 (0.5−10.0 keV (1))
NGC1365 0692840401 (0.5−2.0 keV (2))
NGC1365 0692840401 (2.0−10.0 keV (2))
NGC1365 0692840401 (0.5−10.0 keV (2))
Count-rate (counts/s)
Time (h)

Fig. D.3: (Cont.)

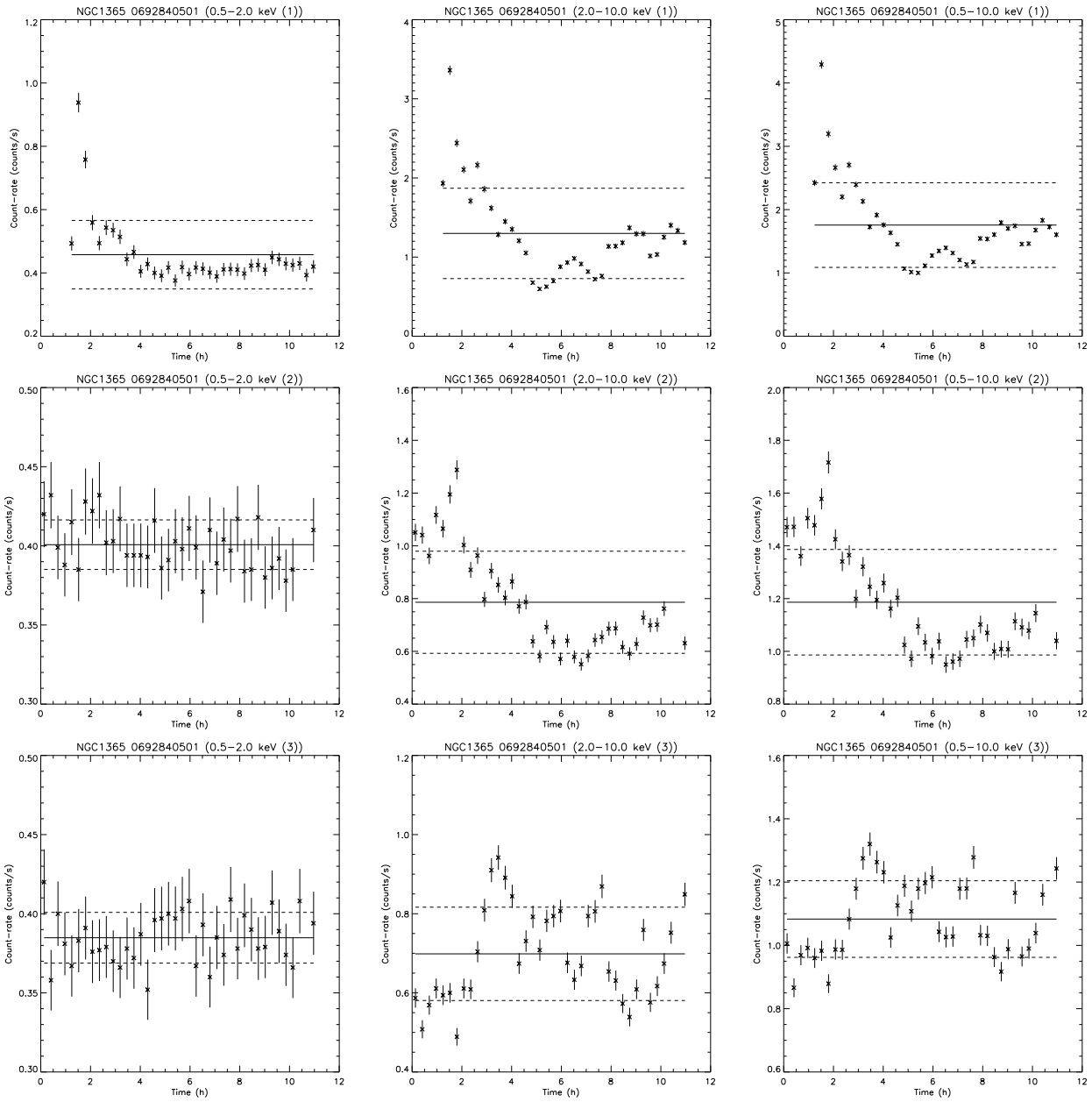

Fig. D.3: (Cont.)

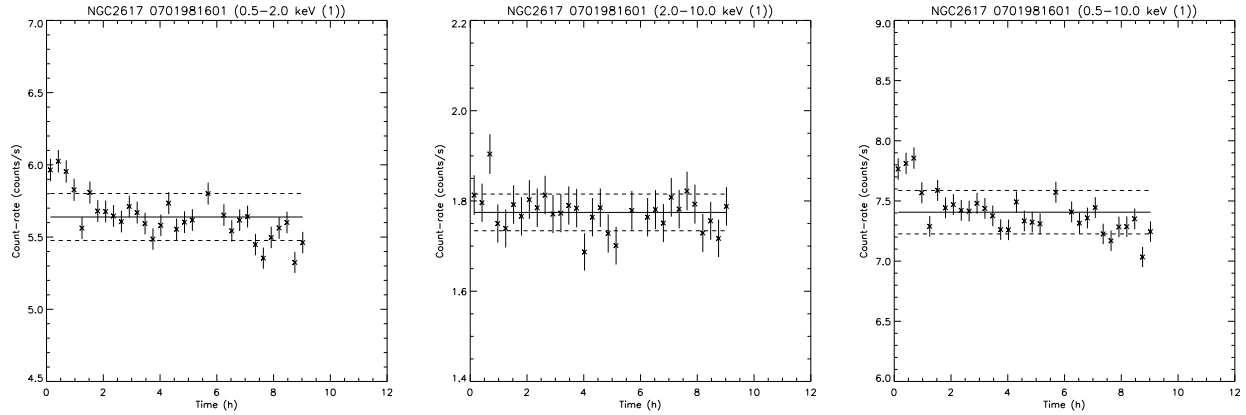

Fig. D.4: Light curves of NGC 2617 from *XMM–Newton* data.

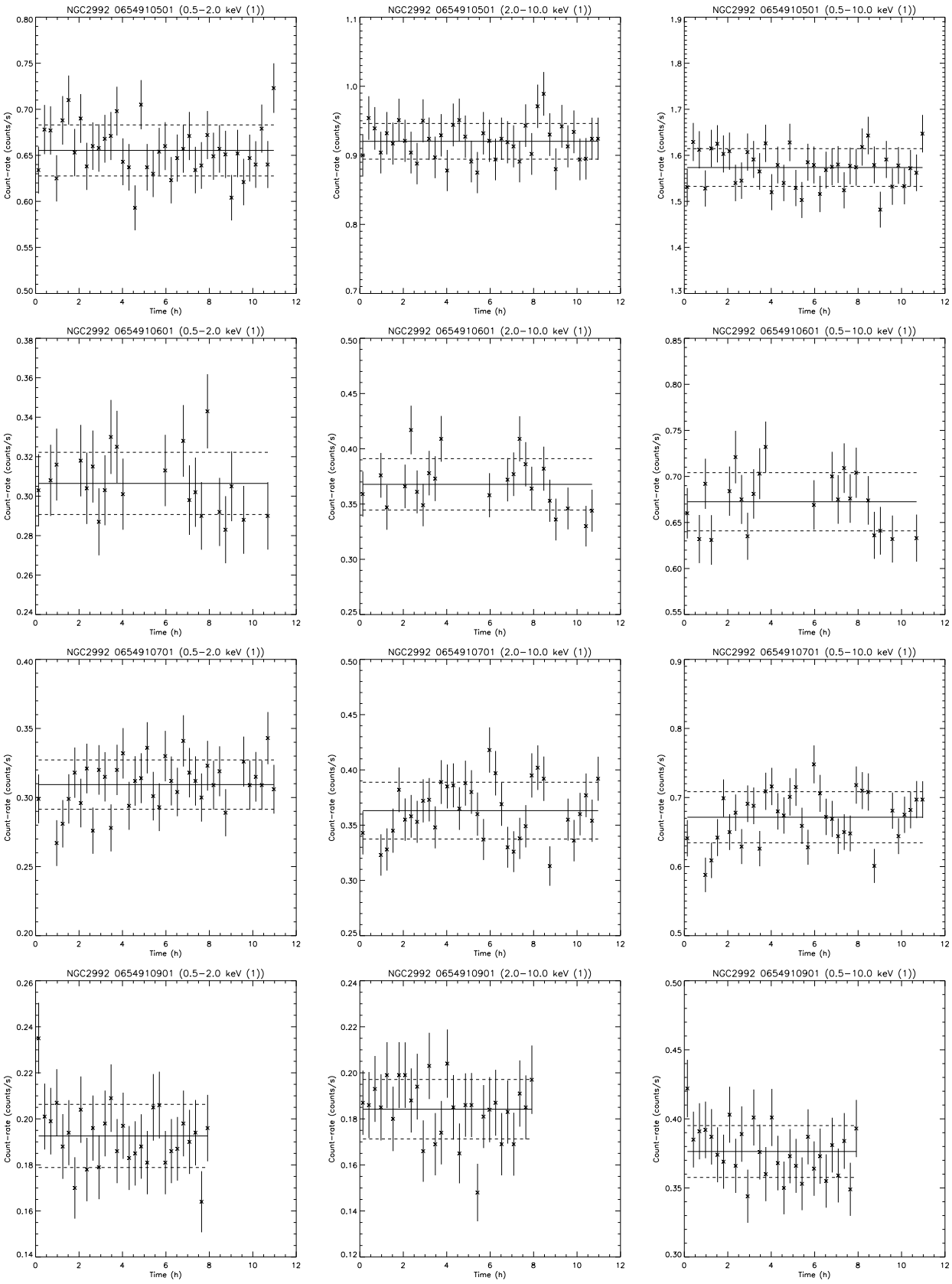

Fig. D.5: Light curves of NGC 2992 from *XMM–Newton* data.

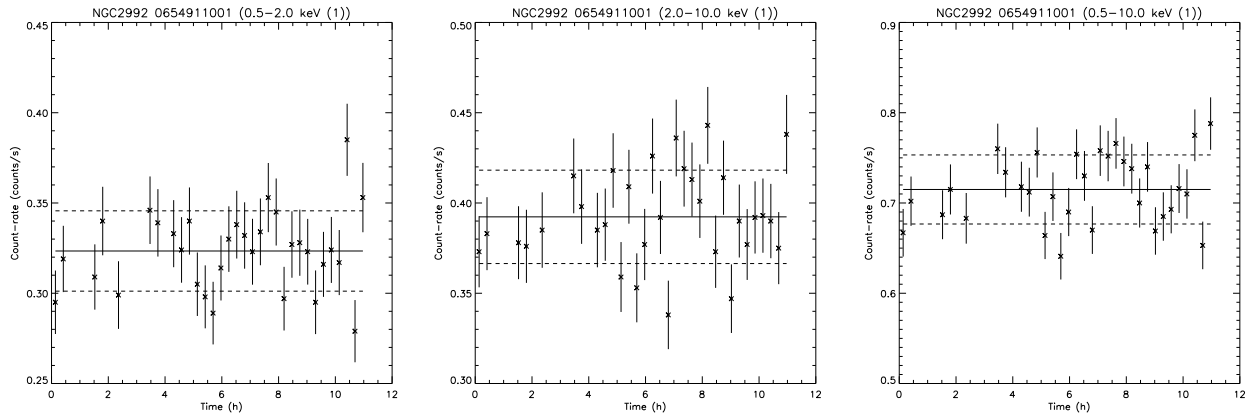

Fig. D.5: (Cont.)

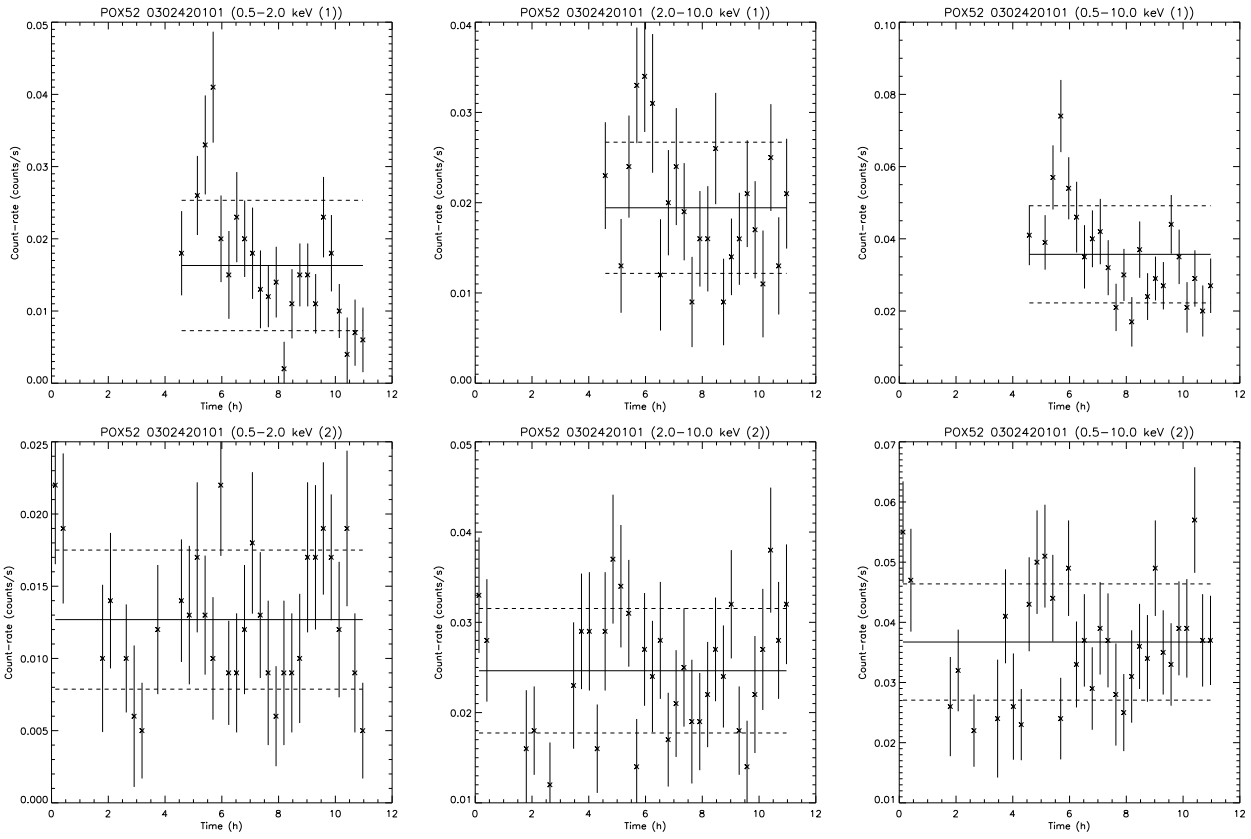

Fig. D.6: Light curves of POX 52 from *XMM–Newton* data.

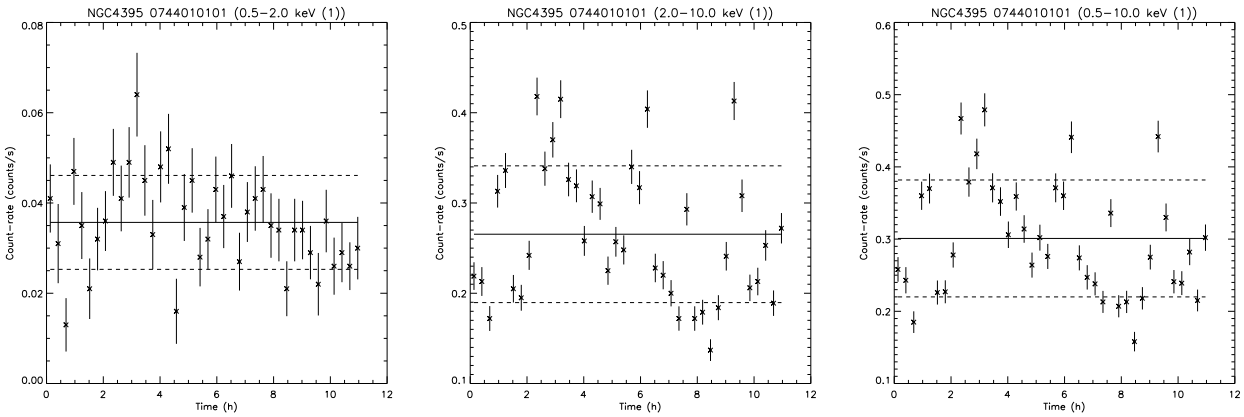

Fig. D.7: Light curves of NGC 4395 from *XMM–Newton* data.

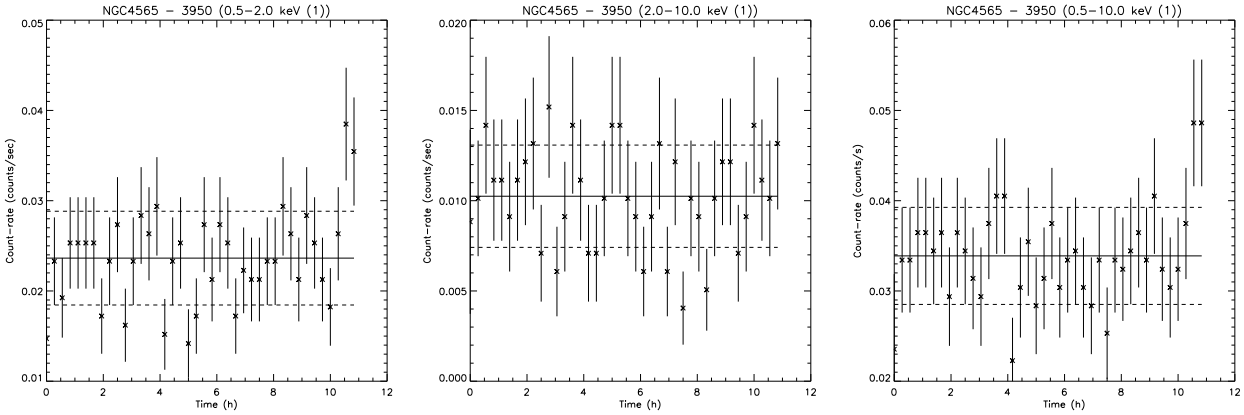

Fig. D.8: Light curves of NGC 4565 from *Chandra* data.